Magnetic Force Microscopy Studies of Submicron and Nanoscale Magnet Arrays

Xiaobin Zhu
Centre for the Physics of Materials
Department of Physics, McGill University
Montréal, Canada
September 2002

A thesis submitted to the
Faculty of Graduate Studies and Research
in partial fulfillment of the requirements for the degree of
Doctor of Philosophy

Your file Votre référence
ISBN: 0-612-85760-3
Our file Notre référence
ISBN: 0-612-85760-3

To Yipeng and Joey

Contents

List of Figures

List of Tables

Abstract

Magnetic structure and magnetization reversal of lithographically patterned submicron and nanometer scaled magnets with elliptical, disk, ring shapes, and pseudo spin valve structures, were studied by magnetic force microscopy.

Magnetic measurements were performed with a custom built vacuum magnetic force microscopy with *in-situ* in plane magnetic fields. The MFM has been optimized with a force gradient sensitivity as high as 1×10^{-6} N/m.

By using various magnetic tips, operating in different modes, and studying different samples, the effect of the magnetic tip stray field induced distortion of the magnetic state of a submicron sized magnet is presented. Through the systematic study, a method of how to detect and to avoid these irreversible distortions is also presented. A local 'hysteresis loop' technique has been invented to study the abrupt switching behavior of individual elements.

In arrays of elongated magnetic particle array, the aspect ratio dependence of the switching indicates that the vortex state can be trapped inside the elements and form an energetic stable state, leading to a broad switching field distribution. In an array of 70 nm wide pseudo spin valve elements, parallel and antiparallel single domain configurations are found. Major and minor hysteresis loops as well as inter-layer coupling are investigated. We found that interlayer coupling leads to switching field variations. In a Permalloy disk array, the vortex state with vortex core singularity is found. The switching mechanism through the nucleation and annihilation processes is demonstrated by the local hysteresis loop. An interdot coupling-induced anisotropic switching is observed. In Permalloy ring structures, a vortex state and an 'onion' state are found. The onion state in permalloy rings with diameters of 5μm is found to be a flux closure state with a head to head domain wall. The switching behavior of these ring elements is found to be domain wall propagation.

Résumé

Les structures magnétiques et le renversement de la magnétisation d'aimants de taille méso- et nanoscopique sont étudiés par microscopie à effet de force. Les aimants, en forme d'ellipses, de disques, d'anneaux et en structures de pseudo vannes de spin, sont produits en réseaux par lithographie.

Les mesures magnétiques sont effectuées sous vide par un microscope à effet de force maison à champs magnétiques in-situ coparallèles à la surface des échantillons. Le microscope est optimisé pour une sensitivité aux gradients de force de l'ordre de 10^{-6} N/m.

Par l'utilisation de différentes pointes, sous différents modes d'utilisation, et d'échantillons variés, l'effet du champ de fuite de la pointe sur le moment magnétique d'un nano-aimant est d'abord observé. Cette étude systématique permet de développer une méthode pour détecter et éviter cette distorsion irréversible. La technique des boucles d'hystérésis locales est développée pour l'étude du renversement soudain d'éléments magnétiques individuels.

Pour le réseau d'éléments allongés, la dépendance du renversement sur le rapport des axes indique qu'un vortex magnétique peut être piégé à l'intérieur des éléments et forme un état énergétiquement stable. Ceci cause une large distribution des champs de retournement.

Dans le réseau de vannes de spin de 70 nm de largeur, des configurations en domaines parallèles et antiparallèles sont observées. Les boucles d'hystérésis majeures et mineures ainsi que le couplage inter-couche sont examinés et il est trouvé que le couplage inter-couche amène une variation du champ de retournement.

Pour le réseau de disques de Permalloy, un vortex avec singularité interne est observé. L'étude de la boucle d'hystérésis permet de démontrer que le renversement est causé par des processus de nucléations et d'annihilations. Le renversement anisotropique causé par le couplage inter-points est aussi observé.

Dans les structures de Permalloy en anneaux, les états de vortex et d'oignons sont mis en évidence. On trouve que la structure en oignons des anneaux de Permalloy de 5 μm de diamètre est une configuration en fermeture de flux à la jonction de deux domaines de magnétisation opposée.

Acknowledgments

First and foremost, I would like to sincerely thank my supervisor Dr. Peter Grütter for his guidance, help and support during the course of my thesis research. He is the person with whom you like to work, not only because he possesses the distinguished scientific talent and knowledge, but also because he has highly respectable virtue.

I sincerely thank the people who provided me the excellent samples. They are Prof. Vitali Metlushko of the University of Illinois at Chicago, Prof. B. Ilic of Cornell University, Dr. Yaowu Hao and Prof. Caroline A. Ross of MIT, Ms. Jianyu Liang and Prof. Jimmy Xu of Brown University, Dr. Russell Cowburn and Dr. Xiong Gang of Durham University (U.K.), Dr. Radek Urban and Prof. Bret Heinrich of Simon Fraser university, Dr. Dirk Ullmann of the Max Planck Institute in Halle (Germany). I am also thankful to them for their instructive discussions.

I am thankful to Dr. Michael Donahue at NIST for his help with three dimensional micromagnetic simulation, and thankful to him for letting me attend the micromagnetic simulation workshop at NIST. I am grateful to Prof. Bret Heinrich for allowing me to visit his surface magnetism lab and to access his MBE system.

I am especially thankful to Dr. Mark Roseman for sharing his expertise in SPM, and am very grateful to him for his help. I am thankful to all my colleagues in the SPM lab, Robert Gagnon, Jeffrey Mativetsky, Michel Godin, Philip LeBlanc, Kaifeng Liang, Manuel Pumarol, Ben Smith, Romain Stomp, Yan Sun, Vincent Tabard-Cossa, Alex Wlasenko, Valentin Yakimov, Anne-Sophie Lucier, Nela Durisic, Yi-ting Huang, and Olivier Laroche for their helpful discussions and assistance. I am grateful to Li Cheng for her help in using the sputtering machine and the X-ray scattering system.

I am grateful to Dr. Martin Dube, Dr. Hong Guo, Dr. Dominic Ryan, Dr. Zaven Altounian, Dr. Mark Sutton, Dr. Qing-Feng Sun for their useful discussions and assistance.

The helps from Frank VanGils, Steve Kecani, and Paula Domingues are also highly appreciated.

Financial support through *Clifford Wong McGill Major Fellowship, Neil Croll Memorial Award, Milton Leong McGill Major Fellowship* and *Beijing Memorial Award* is also greatly appreciated.

I would like to especially thank my wife, Yipeng, for her continuous support and understanding. Special thank to my mother-in-law for her great help in taking care of my wife during her pregnancy and for helping to take care of my little son. Finally, I would like to thank my parents for their continued support.

Statement of Originality

The author claims the following aspects of the thesis to be original contributions of knowledge.

- The custom built vacuum magnetic force microscopy (MFM) was updated in order to achieve the highest possible sensitivity, and to be able to study the magnetic structure and magnetization reversal of nanomagnets in the presence of external magnetic fields.

- A systematic study of the magnetic force microscopy tip stray field induced magnetization reversal of Permalloy particles. Methods about how to detect, reduce and use MFM tip induced magnetization reversal were investigated.

  [1] *X. Zhu*, P. Grütter, V. Metlushko, B. Ilic, *J. Appl. Phys.* **91**, 7340 (2002).

  [2] *X. Zhu*, P. Grütter, V. Metlushko, B. Ilic, *Phys. Rev. B*, **66**, 0244xx (2002).

- Development of spectroscopy techniques including: (a) force distance curves to clarify magnetic states, and to study the local susceptibility; (b) frequency shift versus external field curves to characterize the switching behavior of individual element.

  [3] *X. Zhu*, P. Grütter, in preparation.

- The applications of MFM to study various arrays of submicron and nanometer scaled elongated, disk shaped, ring shaped, square shaped particles as well as pseudo spin valve structures.

  [4] *X. Zhu*, P. Grütter, Y. Hao, F. J. Castano, C. A. Ross, B. Vögeli, and Henry I. Smith, submitted to *Phys. Rev. Lett.* (Pseudo spin valve)

  [5] *X. Zhu*, P. Grütter, V. Metlushko, B. Ilic, *Appl. Phys. Lett.* **80**, 4789 (2002). (Permalloy disks)

  [6] *X. Zhu*, P. Grütter, V. Metlushko, B. Ilic, accepted by *Phys. Rev. B.* (Permalloy ring)

- Micromagnetic simulations through a public code were carried out to interpret the experimental results.

1

Introduction

The topics of this thesis include: (1) the optimization of our vacuum magnetic force microscope (MFM) in order to achieve high sensitivity imaging, (2) the systematic study of imaging, manipulation and spectroscopy of lithographically patterned nanoscaled magnets by MFM, (3) the investigation of magnetic structure and magnetization reversal of various lithographically patterned submicron and nanosized magnet arrays, including elongated, disk shaped, ring shaped, and square shaped particle arrays, as well as pseudo spin valve structures.

1.1 Why Study Nanomagnets?

The study of the interplay between the structure, the magnetic properties and the electrical properties of nanometer and submicron scale magnets is one of the most exciting subjects in modern magnetism. The driving force for this study is the fast growth of the semiconductor microelectronics and data storage industries. The fast growth of computer hard disk storage density requires a detailed understanding of magnetism on the submicron and nanometer scale. Nanomagnet arrays themselves are a potential candidate for ultrahigh storage media, since each uniaxial element can store one bit of data [1]. The interest in studying nanomagnetism is also driven by the potential to incorporate magnetic elements directly into microchips, such as for high density non-volatile magnetoresistive random memory (MRAM) [2, 3]. A further motivation is the potential of using magnetostatic coupled nanomagnet chains

as magnetic logic gates, allowing an all-magnetic implementation of information processing and storage [4]. From a fundamental research point of view, the experimental investigation of nanomagnet elements can be directly compared to micromagnetic simulations, since the simulation code is solvable for submicron sized magnets. This comparison can help test modelling, improve our understanding of micromagnetism, and provide practical parameters for realistic simulation.

1.2 Nanomagnets Fabrication

The study of nanomagnets cannot be separated from modern nanofabrication and high resolution imaging techniques. In nature, crystalline nanomagnets (Fe_3O_4 or FeS_2) with typical sizes of 10 to 100 nm can be perfectly formed in magnetotactic bacteria [5, 6]. Artificial nanomagnets can be fabricated by nanometer fabrication techniques, such as electron-beam lithography (EBL) [7,8], X-ray lithography (XRL) [9], imprint lithography (IML) [10], interference lithography (INL) [11, 12] and self assembly lithography (SAL) using anodized alumina or block-copolymer templates [11, 13]. EBL can be used to prepare magnetic elements with features smaller than 10 nm, but the process of making large area patterns (a few inches) is very difficult. XRL, IML, and INL however, can be used to pattern larger area samples with deep submicron features. SAL also has the ability to make large area samples, but it is hard to produce ordered structures over a large sample area.

The nanomagnet arrays studied in this thesis, provided by our collaborators, were prepared by EBL (University of Illinois at Chicago), INL (MIT), and SAL (Brown University). Fig 1.1 shows one type of INL technique and a typical nanomagnet array. Fig 1.2 shows two arrays prepared by EBL. One array has widely separated 500 nm diameter permalloy ($Ni_{81}Fe_{19}$) disks, while the other one is an array of closely spaced disk chains.

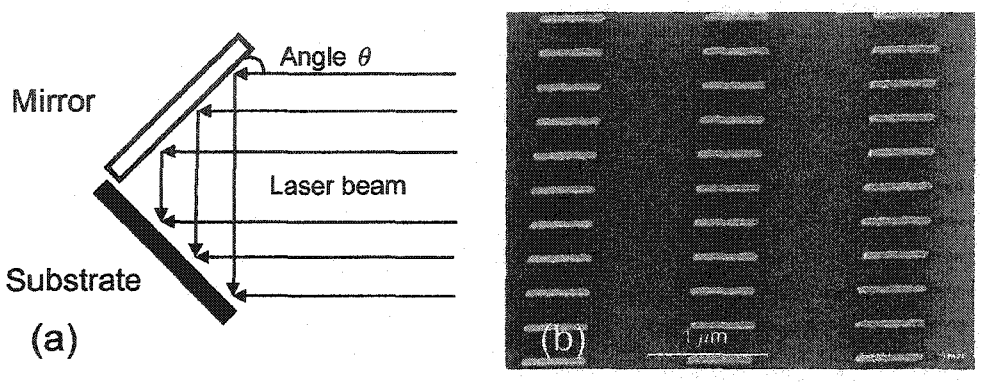

Figure 1.1: (a) schematic diagram of an interference lithography system, after Ross [11]. Two optical beams form an interference pattern on the sample, defining large area periodical structures. The period of the pattern can be controlled easily by varying the angle of the incidence θ and the wavelength λ; (b) a pseudo-spin valve structure with an element width of 70 nm and length of 550 nm and with a polycrystalline Co(4nm)/Cu(3nm)/NiFe(6nm) multilayer composition. The relative orientation of the magnetic moments in the Co and NiFe layers affects the resistance of this structure, i.e., giant magnetoresistive effect. The magnetization switching of individual elements will be presented in Chapter 4.

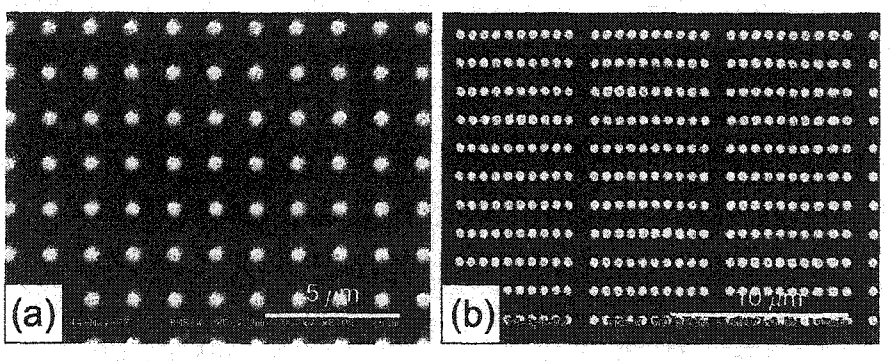

Figure 1.2: Permalloy disk arrays prepared by electron-beam lithography techniques (samples were supplied by V. Metlushko, University of Illinois at Chicago). (a) widely separated individual disks with diameter 500 nm and nominal thickness of 30 nm ; (b) chain of permalloy disks with the same dimensions as (a).

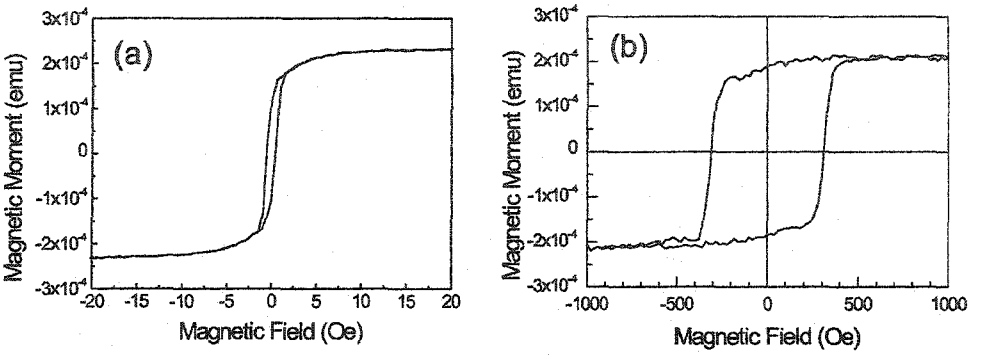

Figure 1.3: (a) hysteresis loop of a two dimensional film, and (b) a lithographically patterned Permalloy ($Ni_{81}Fe_{19}$) film. The film thickness is 10 nm, and the patterned element is $90nm \times 240nm$ in size. The coercivity in (a) is about 1 Oe, while it is about 300 Oe in lithographically the patterned sample. Courtesy: Y. Hao, MIT.

1.3 Characterization of Magnetic Properties

Submicron or nanometer scaled magnetic elements show different magnetization switching behavior than bulk material. The shape anisotropy can change the magnetization behavior dramatically [14]. For example, nanomagnets usually have a much larger coercivity than an unpatterned thin film deposited under identical conditions. Fig 1.3 shows typical hysteresis ($M - H$) loops for an unpatterned thin film and a patterned one. The coercivity for the unpatterned is only about 1 Oe, while it is a few hundred Oe for the patterned. The increased coercivity is the result of the increased demagnetization field in-plane.

The magnetic domain structures in patterned elements are also substantially different from those in unpatterned material. This characteristic is especially obvious for soft magnetic materials, such as iron, nickel or Permalloy, in which the domain patterns are mainly determined by the element shape, size and thickness. For a two dimensional film, the exchange interaction favors the alignment of magnetic moments. However, to minimize the total energy, the magnetic dipole interaction prefers the magnetic moment to be random due to the finite dimensions of the film. The compe-

tition between the exchange energy and the magnetostatic energy leads to the domain structures.[1] Fig. 1.4 show a series of images for different sized samples of the same material. Fig. 1.4 (a) shows the domain pattern of an unpatterned Permalloy film, obtained by Lorentz microscopy. A complex domain pattern with clear Néel walls, cross-tie walls and magnetic ripple structures is observed. This kind of domain pattern is very common in two dimension films [15]. However, a 20 μm sized Permalloy square forms a flux closure structure with some fine domain structures at the corners (Fig. 1.4(b)). This type of domain pattern is theoretically expected, since flux closure structures minimize the total energy, with a stray field energy approaching zero [16]. The observed seven-domain structure is not the only minimal energy state, but other domain patterns, such as a four-domain structure, can also be observed experimentally on the sample (as will be shown later).

For sufficiently small elements, due to the energy cost of a domain wall, it is energetically unfavorable to form domain structures in the element, and the element prefers to form a single domain state. Domain theory [17] estimates that the critical size of a sphere magnetic material for forming a single domain is

$$R_{c0} = \frac{q2}{M_s}\sqrt{\frac{6A_{ex}}{4\pi}} \approx \frac{1.595\sqrt{A_{ex}}}{M_s}, \tag{1.1}$$

where M_s is the saturation magnetization, A_{ex} is the exchange constant, and $q2$ is the smallest root of the derivative of the spherical Bessel function of the first kind and first order. The typical value is a few tens of nanometers. However, for elements larger than this critical value, shape anisotropy is a crucial feature in the formation of a single domain state. Fig. 1.4 (c) shows an MFM image of an array of Permalloy elements with a size of 90 nm $\times$ 240 nm and a thickness of 10 nm. The MFM image shows bipolar contrast (white and black), associated with south and north poles of single domain elements.

[1] In real cases, the anisotropy energy should also be taken into account. The different energetic terms in magnetic body are described in Appendix A.

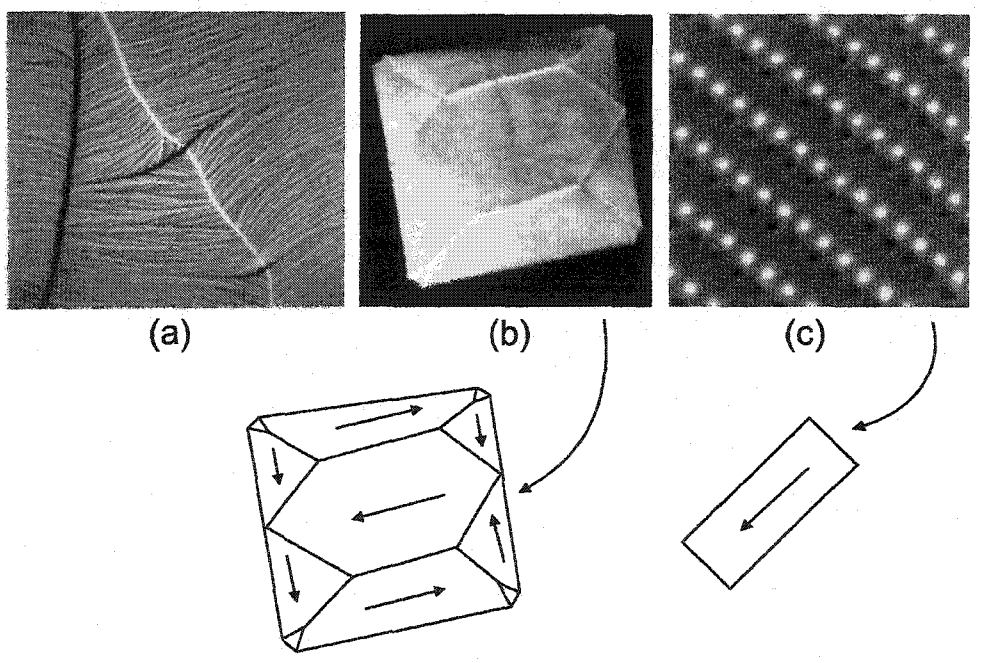

Figure 1.4: (a) a Lorentz microscopy image of a thin two dimensional Permalloy film (cover page of Physics Today, May 2001); (b) the domain structure in a 20 μm permalloy square, with thickness of 30 nm. Constant frequency shift mode, Tip: 15 nm $Co_{71}Pt_{12}Cr_{17}$, Cantilever resonance frequency: 69.690 kHz, in vacuum; (c) single domain structure in a 240nm $\times$ 90nm $\times$ 10nm permalloy element array. Constant height mode; Tip sample separation h= 80 nm; Silicon cantilever with the spring constant of 22.67 kHz in vacuum, 30 nm coated $Co_{71}Pt_{12}Cr_{17}$; rms oscillation amplitude: 12 nm. Schematic diagrams of the domain patterns in (b) and (c) are indicated by the arrows. A flux closure domain is formed in (b), while a single domain is formed in (c).

1.3.1 Experimental Tools

It is crucial both from a fundamental as well as an application point of view to understand and control the magnetic behavior of such small magnetic elements. This requires special experimental tools to characterize the magnetic properties. The collective magnetic properties such as the hysteresis loop can be characterized by standard techniques. However, it is even more important to characterize the individual behavior of the nanomagnets, and only then can some of the following questions be answered: What is the domain structure of an individual nanomagnet? How does an individual nanomagnet switch in response to an external field? How fast does it switch? What are the transport properties of these structured nanomagnets? Finally, what is the variability of these properties from element to element?

The collective behavior can be characterized by alternating gradient magnetometery (AGM), by vibration sample magnetometery (VSM), using superconducting quantum interference device magnetometers (SQUID) and through the use of magnetooptical Kerr effect (MOKE). However, due to variations between individual elements, the characteristics of an individual element can be washed out in the measurements of ensembles. There are however some sophisticated spatially resolved techniques which allow the investigation of the magnetic properties of individual elements. Magnetic force microscopy (MFM) [18–20], Lorentz electron microscopy (LEM) [21], scanning electron microscopy with polarization analysis (SEMPA) [22] and MOKE microscopy [16] can be used to characterize the magnetic domain structure of individual elements. LEM, Micro-SQUID techniques [23, 24], micro-Hall techniques [25] and MFM [26] can also be used to study the magnetization behavior of an individual element. Time-resolved scanning Kerr microscopy can resolve the magnetization distribution in time [27]. These techniques are complimentary. Each technique has its advantages as well as drawbacks. A combination of these techniques allows one to fully reconstruct the complete magnetization distribution and to fully understand the mechanism of magnetization switching.

The domain observation by LEM is based on the Lorentz force deflecting the electrons:[1] $F_L = q_e V \times B$. The unique features of LEM are high resolution (nanometer), high contrast, and a direct measurement of the magnetization vector. However, the disadvantages of this technique are that it requires very special sample preparation (flat and electron transparent), and it is difficult to apply magnetic fields to the sample as this changes the electron beam trajectory. It is thus challenging to observe changes of the magnetization via external magnetic field in LEM.

SEMPA collects the spin polarized secondary electrons emitted by a magnetic sample. The secondary electrons have magnetic moments which are parallel to the magnetization direction at the point of their origin. Unlike the traditional SEM, SEMPA is also sensitive to the polarization of secondary electrons. SEMPA has a high spatial resolution (10 nm) which is determined by the beam width and it directly detects the sample magnetization component. The major limitation of using SEMPA is sample preparation, as the experiment must be performed in ultra high vacuum conditions on a clean conducting surface to avoid loss of the secondary electron polarization by scattering.

MFM records the magnetostatic forces or force gradient between a magnetic sample and a small (with typical radius of 10-50 nm) magnetic tip. The detailed principle of MFM will be presented in the next chapter. The advantage of this technique is that it does not need special sample preparation, and can work in ambient conditions with a spatial resolution down to 10 nanometers [28]. However, it is not easy to separate the magnetic contrast from other background forces. The interpretation of the observed magnetic contrast is not straightforward since MFM does not directly monitor the magnetization distribution but rather the stray field. Furthermore, there is the potential of mutual distortion between the MFM tip and the sample moment. Interpretation of an observed image usually relies on the understanding of micromagnetism

[1]This is a classical view. The detailed classic and quantum theory underlying LEM can be found in a review paper by Chapman [21].

and micromagnetic simulations.

All of the above techniques have one common demerit: poor time resolution. It takes about one second for LEM and a hundred seconds for MFM or SEMPA to form an image. Very fast imaging within nanosecond scale can be achieved by scaning Kerr microscopy measurements [27,29], allowing the dynamics of domain pattern formation to be studied. However, the spatial resolution of the MOKE technique is limited by the wavelength of the laser used and thus is about few hundred nanometers.

Among all these techniques, MFM is the most commonly used to study the magnetic structure of nanomagnets due to its easy implementation and lower costs. Furthermore, MFM is not just a tool for imaging, it can also be used to study the magnetization behavior of individual elements with a capability similar to that of micro-Hall and micro-SQUID techniques [26]. MFM also has the potential to study the collective magnetization switching behavior by performing large area scans with *in-situ* magnetic fields [30,31].

1.3.2 *Micromagnetic Simulation*

Micromagnetic simulations can be used to help explain experimental observation, and to understand the domain formation process. The simulation can be performed by solving the Landau-Lifshitz equation [32]:

$$\frac{dM}{dt} = -\gamma M \times H_{eff} - \frac{\gamma\alpha}{M_s} M \times (M \times H_{eff}), \tag{1.2}$$

where M is the magnetization, H_{eff} is the effective field, γ is the gyromagnetic ratio, while α is the damping coefficient.[1] The effective field is defined as

$$H_{eff} = -\frac{\partial E}{\partial M}, \tag{1.3}$$

where E is the total magnetic energy density including the exchange energy, anisotropy energy, Zeeman energy, and magnetostatic energy (demagnetizing energy). Details

[1]The simulations in this thesis were performed by the publicly available code OOMMF from NIST, http://math.nist.gov/oommf.

about the micromagnetic simulation are presented in the Appendix A.

1.4 Scope of this Study

There is mutual distortion between the magnetic tip and the magnetic sample. Such distortions can sometimes be calamitous while studying nanomagnets, as the MFM tip stray field can irreversibly change the particle's state [33]. Such effects frequently appear in the published literature, and in some circumstance it is unavoidable as the local tip stray field can be larger than the element switching field. In this thesis, by using various magnetic tips, operating in different modes, and studying different samples, the effect of magnetic tip stray field distortions on a nanomagnet state is investigated. Through systematic study, a method of how to detect and to avoid the irreversible distortion is also presented.

MFM is not just a tool for imaging, in this thesis, the versatility of MFM is explored. MFM is used to study the magnetization reversal behavior of individual submicron sized magnets and ensembles. Local hysteresis loop technique is developed by monitoring the resonant frequency shift of the cantilever as a function of external magnetic fields. Finally, the possibility of using the MFM tip stray field to manipulate a magnetic state of an individual particle, 'writing' a bit, is also demonstrated.

In the second part of the thesis, MFM is used to study the magnetization behavior and the domain structures of different kinds of patterned arrays. Different submicron and sub-100 nm arrays are studied extensively by using MFM in the presence of an external magnetic field. The samples studied in this thesis are elongated particles, disks, rings, and pseudo spin valve structures.

The structure of the thesis is as follows: the experimental technique (MFM), instrumentation and MFM tip stray field distortion on two dimensional samples is presented in Chapter 2. Chapter 3 details the study of imaging, manipulation, and spectroscopy of nanomagnets, including the separation of magnetic contrast from other signal, and detection, reduction and application of MFM tip stray induced ir-

reversible distortions. The technique allowing the determination of hysteresis loops of ensembles of nanomagnets is also presented. Finally, a local hysteresis loop technique is developed. The detailed study of pseudo spin valve structures is presented in Chapter 4. In chapter 5, the magnetic structure and magnetization reversal of disk arrays are studied. In chapter 6, the study of permalloy ring structures is presented. The conclusion and outlook is presented in Chapter 7.

Throughout the thesis, gaussian units are used for magnetic field and magnetization. 1 Oe = 79.58 A/m; 1 emu/cm^{-3} = 1000 A/m, as they are the units commonly used in the literature and technology.

2

Experimental Techniques

In this chapter, a review of magnetic force microscopy and the instrumentation will be presented. The sensitivity of our vacuum MFM is demonstrated to be thermally limited. The highest imaging sensitivity can be achieved by operating the MFM in vacuum in the constant height mode. Various techniques designed to improve the sensitivity of the instrument are discussed. Tip stray field induced distortions of the sample magnetic structure are also presented.

2.1 Magnetic Force Microscopy

2.1.1 Principle of Magnetic Force Microscopy

The magnetic force microscope (MFM) [18, 19], a variant of the scanning force microscope, is a tool capable of revealing a magnetic sample's domain structure in real space. The basic principle is illustrated in Fig 2.1. A flexible cantilever beam with a

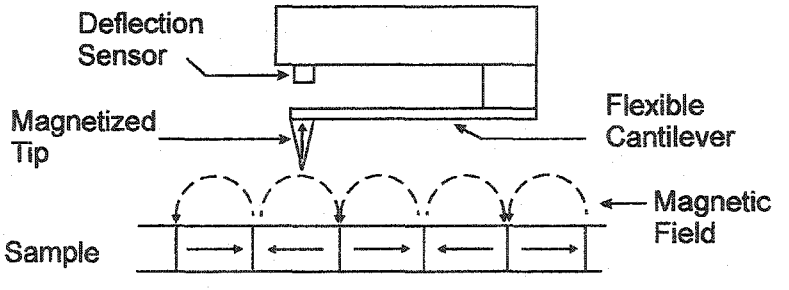

Figure 2.1: A magnetically sensitive cantilever interacts with the magnetic stray field of the sample. Resulting changes in the status of the cantilever are measured by the deflection sensor, and recorded to produce an image. Adapted from [20].

sharp magnetic probe on its end is used as a force sensor. If the tip is brought close enough to the sample surface, typically between ten to a few hundred nanometers, the magnetic interaction between the tip and sample can give rise to a change of the cantilever status, such as static deflection or resonant frequency. As the MFM tip (sample) is raster scanned across the sample (tip), this change can be used to form a two dimensional magnetic image. In force spectroscopy, another operation mode of MFM, the cantilever status is monitored with respect to the tip-sample separation.

2.1.2 *Magnetic Interaction & Experimental Technique*

MFM detects the force or force gradient between the MFM tip and magnetic sample [20]. The magnetic force acting on the tip can be written as

$$F_{t-s} = \int d^3r' \int d^3r'' \mathbf{M}(r') \bigtriangledown \cdot \mathbf{H}(r'', r') \tag{2.1}$$

where $\mathbf{M}(r')$ is the tip magnetization at position r' inside of the tip, while $\mathbf{H}(r'', r')$ is the sample stray field at position r' generated by the magnetic moment at position r'' inside of the sample.

The consequence of the force is to directly bend the cantilever beam by the amount of $\delta z = F_n/k_{cb}$, where F_n is the component of the force normal to the cantilever, and k_{cb} is the spring constant of the cantilever. These deflections can be used to form MFM images. However, this mode is not commonly employed because the dc measurement is easily corrupted by noise, such as vibrations and $1/f$ electronic noise.

Much higher sensitivity can be achieved in the ac mode by driving the cantilever at (or close to) its resonant frequency to reduce environmental noise [18], and to increase the signal to noise ratio using lock-in techniques or frequency modulation techniques [34]. In this case, the cantilever beam can be treated as a one dimensional damped driven harmonic oscillator with a resonance frequency of $f_0 = (k_{cb}/m^*)^{1/2}/2\pi$, where m^* is the effective mass of the cantilever [20]. For long range forces (magnetic force) and for small oscillation amplitudes (compared to the decay length of the magnetic interaction), the tip-sample interaction can be treated as a spring in series

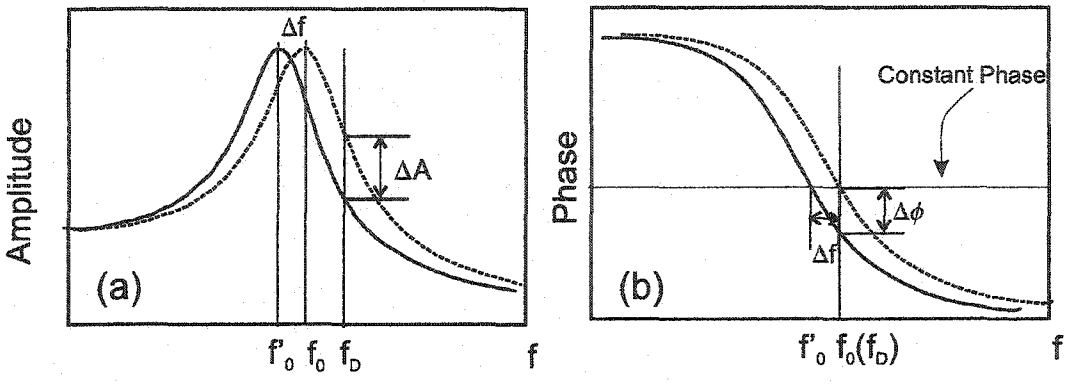

Figure 2.2: AC detection techniques. If a cantilever is driven at a fixed frequency f_D (lock-in technique), a cantilever resonance frequency shift causes the cantilever oscillation amplitude and phase to change. The amplitude change ΔA (a) or the phase change $\Delta\phi$ (b) can be interpreted as a magnetic signal. However, the direct frequency shift Δf can be obtained by a frequency modulation technique: the cantilever phase is maintained at a constant value by a phase locked loop.

with the cantilever. This causes the cantilever to oscillate at a new resonant frequency $f_0' = ((k_{cb} + F_n')/m^*)^{1/2}$, as indicated in Fig. 2.2, where F_n' is the force gradient along the normal direction of the cantilever. In a linear approximation, the frequency shift can be written as

$$\delta f = \frac{F_n'}{2k_{cb}} f_0. \tag{2.2}$$

However, if a short range force such as a spin-spin interaction is involved, the cantilever oscillation is usually much larger than the decay length of the force, and nonlinear effects need to be considered [35].

The cantilever resonant frequency shift can be obtained by either lock-in techniques [18] or frequency modulation (FM) techniques [34]. In the lock-in technique, the cantilever is driven at a fixed frequency (f_D, as indicated in Fig 2.2). During imaging, the oscillation amplitude A (Fig 2.2 (a)) or the phase ϕ (Fig 2.2 (b)) of the cantilever will change due to the tip-sample interaction. In the linear approximation, the amplitude and the phase change are linear in the frequency shift and the force gradient. In the FM technique, however, the phase relation between the drive signal and the cantilever oscillation can be kept at a constant value by a phase locked loop (PLL). Therefore, the cantilever can always be driven at its new resonance frequency

$f_0' = f_0 + F'$ [20, 34], and the cantilever frequency shift can be directly monitored. In addition, in the FM technique, the cantilever oscillation amplitude can be maintained at a constant value by an additional analog feedback. This option is used for dissipation imaging, an imaging technique which is sensitive to non-conservative interactions, as compared with the frequency shift information which is indicative of conservative interactions [36, 37].

2.1.3 *Operating modes*

The tip-sample interaction has different origins which include magnetic interactions, electrostatic interactions, van der Waals interactions, short range and capillary forces. During MFM imaging, the tip-sample separation usually varies between ten to a few hundred nanometers, where the magnetic force (F_{mag}), electrostatic force (F_{elec}) and van der Waals force (F_{van}) are dominant. Therefore, the total force is approximately,

$$F_{tot} = F_{mag} + F_{elec} + F_{van}. \tag{2.3}$$

The van der Waals force and force gradient between a sphere tip and semi-finite flat sample can be written as [38]

$$F_{van} = A_H R/6z^2, \tag{2.4}$$

$$F'_{van} = -A_H R/12z^3, \tag{2.5}$$

where R is the effective radius of the tip, z is the tip-sample separation and A_H is the Hamaker constant with a typical value of 1 eV for metals. For a sharp MFM tip (sharp silicon tip with thin film coating), the van der Waals force is usually very small. For example, for a tip radius of 10 nm, and a tip-sample separation of 50 nm, the force gradient is about 1×10^{-6} N/m. Even if the tip becomes blunt with a radius of 50 nm, the force gradient will only be 5×10^{-6} N/m. However, an order of magnitude increase is observed for tip sample separations of 20 nm.

The electrostatic force and the force gradient between a metallic tip and sample can be written as

$$F_{elec} = \pi\varepsilon_0 U^2 R/z \tag{2.6}$$

$$F'_{elec} = -\pi\varepsilon_0 U^2 R/z^2, \tag{2.7}$$

where U is the bias voltage between a tip and a sample, R is the effective tip radius, ε_0 is the permittivity of free space and z is the tip-sample separation. Assume R=10 nm, z=50 nm, U=100 mV, we can estimate the force gradient: $F'_{elec} = 1 \times 10^{-6} N/m$. However, if the bias voltage is set to be 1 V, the force gradient will be two orders of magnitude larger, $1 \times 10^{-4} N/m$.

The magnetic force (force gradient) between a magnetic tip and sample depends on both the tip and the sample moment distribution. Since both the magnetic tip and magnetic sample prefers to form domain structures (flux closure) to reduce stray field energy (magnetostatic energy), the magnetic force (force gradient) can decay very slowly. For example, the force gradient above the center of a transition of a longitudinal recording medium with a long dipole tip can be written as [39]

$$F'_{mag} \sim \frac{1}{(a+z)^2}, \tag{2.8}$$

where z is the tip-sample separation, and a is the transition width, on the order of 100 nm. As can been seen, when the tip-sample separation is on the order of 100 nm, the force gradient decays slower than the electrostatic and van der Waals forces. Due to the often unknown tip moment distribution and different nature of the sample domain walls, there is no universal law relating the magnetic force (force gradient) to the tip-sample separation.

With a small bias voltage U and a sharp tip, the van der Waals force gradient and the electrostatic force gradient can be much smaller than the magnetic force gradient, and the magnetic interaction can be dominant even at small tip-sample separations (20 nm).

To generate a magnetic image, MFM can be operated in a constant frequency shift mode [20], a tapping/lift mode [40] or a constant height mode.

- Constant frequency shift mode

As shown in Fig. 2.3 (a), in the constant frequency shift mode, the image is generated by maintaining a constant cantilever resonance frequency shift by adjusting the tip-sample separation, i.e.,

$$F'_{total} = F'_{mag} + F'_{elec} + F'_{van} = const, \tag{2.9}$$

and the magnetic image is therefore the contours of force gradient.

The magnetic force between the tip and sample can be attractive or repulsive. To stabilize the feedback, the relation between the force (force gradient) and the tip-sample separation needs to be monotonic. To fulfil this, a dc voltage needs to be applied between the tip and sample to provide a servo force, even though van der Waals forces occasionally can be used as a servo force as the tip becomes blunt. For a flat surface, the observed contrast will mainly come from the magnetic interaction. However, if the surface is not flat, the obtained image will certainly be a convolution of the magnetic contrast with the topography. By applying an AC voltage between the tip and sample, topography and magnetic contrast however can be partially separated by using electrostatic force gradient as feedback signal [41].

- Tapping/lift mode

Tapping/lift mode is a very elegant method developed by Digital Instruments [40]. In this mode, the magnetic contrast and the topography can be nicely separated. As shown in diagram Fig. 2.3 (b), the sample is scanned twice: the sample's topography is obtained in the tapping mode scan using the cantilever oscillation amplitude as feedback. Magnetic contrast is subsequently obtained in the lift mode scan by monitoring the cantilever's frequency or the phase shift upon rescanning the previously measured topography with a user controlled height offset, h.

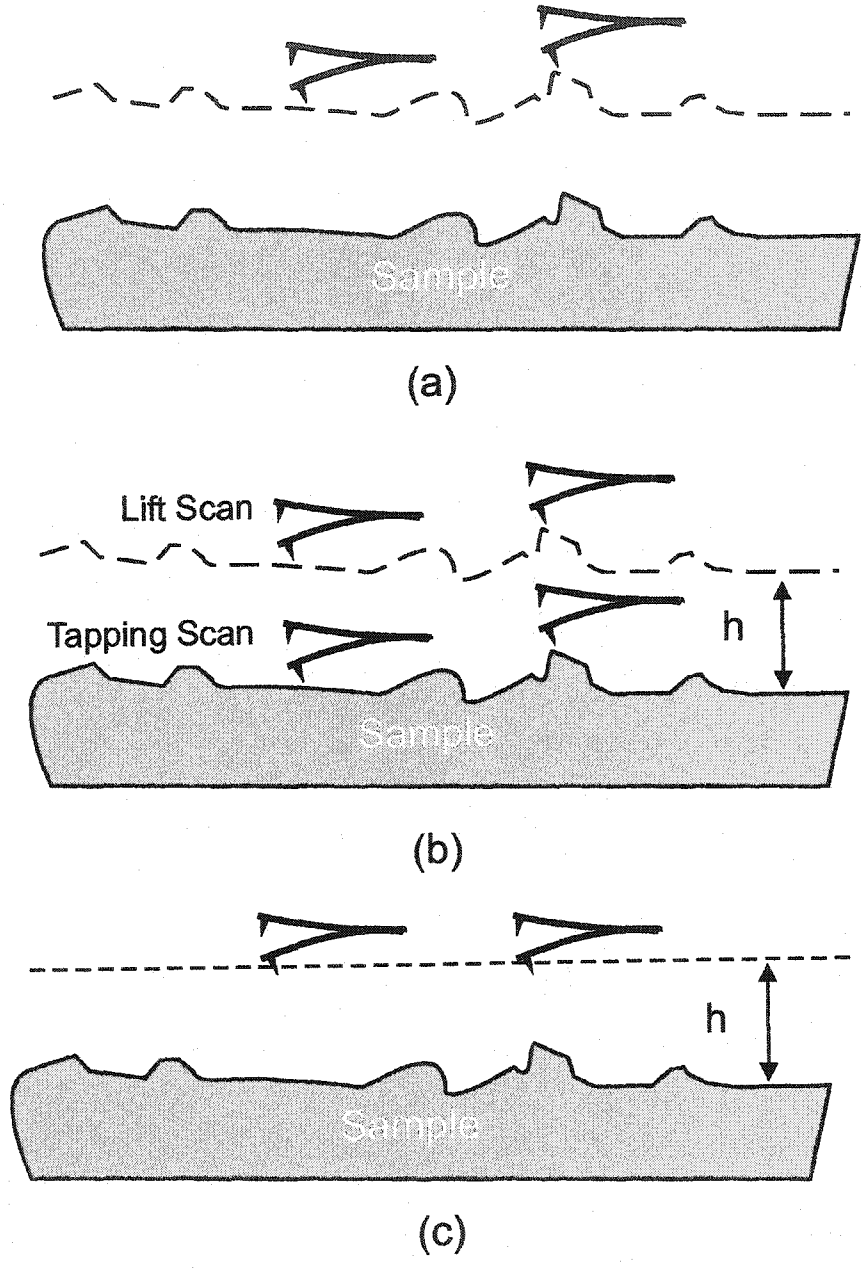

Figure 2.3: Schematic diagrams of the different operating modes: (a) constant frequency shift mode. The feedback loop maintains the resonance frequency at a constant value (eq. 2.9) by adjusting the tip-sample separation; (b) tapping/lift mode, tapping scan is used to obtain the sample's topography, while the lift scan follows the topography with a lift hight h(dashed line). The clean separation of topography signal and magnetic signal can be obtained; (c) constant height mode. The tip flies in a plane above the surface.

- Constant height mode

The constant height image can be obtained by directly monitoring the frequency signal in the constant frequency shift mode while using a fast scan speed. However, there will still be a strong convolution between topography and magnetic signal as a bias voltage U is applied between the tip and sample, especially while imaging non-flat samples.

A constant height mode scan can also be performed as follows. Instead of tracking the sample's topography, the tip is scanned across the surface at a predetermined constant height while the cantilever frequency shift is monitored. Unavoidable sample tilt is compensated by tilt correction hardware. A zero or small bias voltage to compensate the work function difference between tip and sample is applied while acquiring magnetic data. This minimizes electrostatic contributions to image contrast. By using this technique, magnetic contrast can be obtained even when the tip is as close as 20 nm to the sample with minimal topography cross-talk. This mode of imaging has the best signal to noise ratio (no feedback noise) and the potential of increased scan speeds.

2.2 Instrumentation

During this thesis, three different microscopes have been used to obtain magnetic images: two commercial systems (BioScope and MultiMode from Digital Instruments) and one custom built vacuum magnetic force microscope (VMFM). The BioScope and MultiMode are operated in the tapping/lift mode to obtain magnetic and topography images simultaneously. The VMFM is operated in the constant frequency shift and constant height modes. In the following, the instrumentation of the VMFM will be presented. Details about the system can be found in previous theses from our group [37,42]. My research has focused upon maintaining and updating the VMFM to achieve higher sensitivity, and to use it to study magnetization reversal of small magnetic elements.

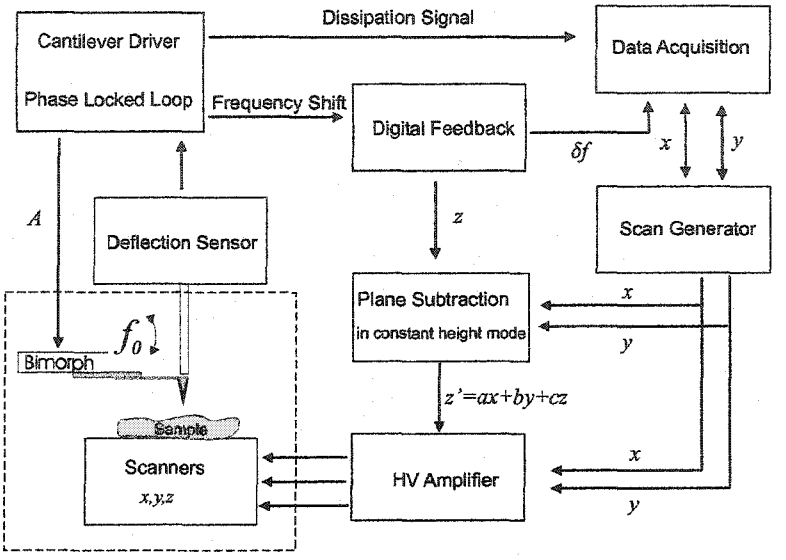

Figure 2.4: Block diagram detailing the components of the magnetic force microscope. The items enclosed within the dashed line are subjected to vacuum. D/A and A/D convertors are not included.

We use the FM technique to directly measure the cantilever resonance frequency shift with a PLL. Fig. 2.4 shows a block diagram of the setup. During imaging, the cantilever beam is oscillated at its resonance frequency with an amplitude A,[1] while the sample is raster scanned by a pizeotube scanner with respect to the cantilever. A optic fiber interferometer is used to detect cantilever deflections, and the PLL is used to decode its frequency. The frequency shift signal obtained by the PLL can be maintained constant through a feedback loop by varying the tip-sample separation. This leads to the acquisition of contours of constant force gradient. As an alternative, images can also be obtained in the constant height mode.

The microscope together with damping plates, indicated in the dashed line in Fig. 2.4, sits inside a vacuum chamber with a base pressure of 5.0×10^{-6} Torr. The vacuum environment increases the cantilever's quality factor and reduces the acoustic noise. The whole vacuum chamber sits on an optical table to isolate it from floor vibrations. The microscope head, which includes the force and deflection sensor, is

[1]The oscillation amplitude A is defined by half of the peak to peak amplitude all through the thesis, unless otherwise specified.

kinematically mounted onto the base which houses the sample pizeo scanner. Three micrometer screws are used to perform coarse and fine approaches. The piezo scanner is two inches long, leading to a maximum lateral scan size in x-y of 120 μm and a vertical scan range, z, of 9 μm with the applied voltage of $\pm$300 V. The scanner is mounted on an orthogonal pair of piezo walkers which provide x-y motion of the sample with a range of $\pm$ 5 mm.

2.2.1 *Force Sensor*

The force sensor is the most crucial part of the MFM. We use thin film coated tips as our force sensors. The cantilevers used are commercially made by NanoSensors [43] and MikroMasch [44]. Figure 2.5 shows a scanning electron microscopy image and a transmission electron microscopy (TEM) image of a cantilever from MikroMasch [44]. The tip has a pyramidal shape with a height of 10 μm. The tip radius is 10-15 nm with the facet angle of about 15°.

The optimum properties of the magnetic tip coating is a tradeoff between a large signal to noise ratio and the magnitude of the tip stray field which can induce irreversible distortions of the sample's magnetic structures. A large moment tip can achieve a large signal to noise ratio, but also tends to have a big tip stray field. Tailoring the magnetic moment of the probe was achieved by coating different materials at various thicknesses. We coated cantilevers with Co, $Co_{80}Cr_{20}$, $Co_{71}Pt_{12}Cr_{17}$, $Ni_{81}Fe_{19}$, Fe, and $Ni_{50}Co_{50}$ by sputtering or thermal evaporation. The outside of the film is usually coated with a 5 nm of gold to protect the magnetic layer from oxidation. The probe is magnetized along its z axis in a 10^4 Oe field prior to the experiments.

The spring constant of the cantilever is a very important parameter of the force sensor. The detected magnetic force (force gradient) is small. Thus soft cantilevers have better sensitivity, but are more susceptible to being snapped into the sample for the cantilever spring constant smaller than the force gradient. Furthermore, soft cantilevers are not suitable for tapping scans at ambient conditions if the experiment

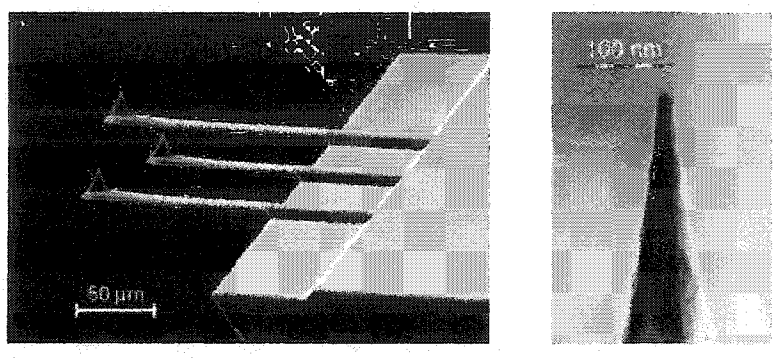

Figure 2.5: Scanning electron microscopy image of three cantilevers (left), and transmission electron microscopy image at the end of a force sensor. There images were taken from the MikroMasch website, the company which supplies the cantilevers.

is to be performed in tapping/lift mode. The cantilevers we used in our experiments have typical spring constants of 0.01 to 2 N/m and resonant frequencies of 10 kHz to 150 kHz. The spring constants of the cantilevers are calibrated by a geometry method, based on the measured plane dimensions of the lever (length and width), the resonant frequency and quality factor [45], which can be express as,

$$k_{cb} = 0.1906 \rho_f w^2 l Q_f \Gamma_i(\omega_f) {\omega_f}^2, \tag{2.10}$$

where ρ_f is the density of the fluid (1.18 kg/m^3 in air), Q_f is the quality factor in fluid (air), $\Gamma_i(\omega_f)$ is the imaginary components of hydrodynamic function Γ [46], w is the width of the cantilever and l is the length of the cantilever.

2.2.2 *Deflection Sensor*

There are different ways to detect the deflection of a cantilever beam [47]. Among the optical methods, beam deflection and interferometry are commonly used due to their high sensitivity and ease of implementation. Fig. 2.6 shows schematic diagrams of the beam deflection method and the interferometer method. In our Multimode NanoScope, the beam deflection technique is used, while in the home built system, an interferometry technique was adopted (originally described by Rugar et al. [48]).

In our interferometer deflection sensor, the laser light is guided through a 125 μm diameter fiber with a core size of 5 μm into a 50/50 bi-directional coupler. The fiber

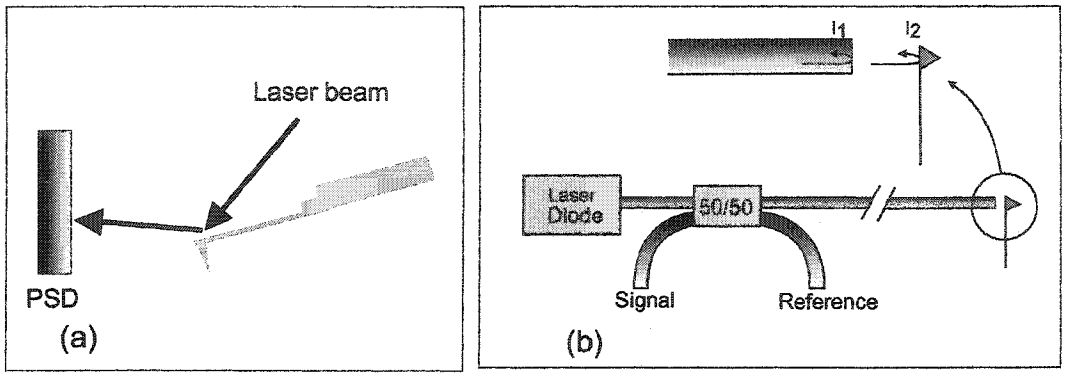

Figure 2.6: The deflection sensors: (a) optical beam deflection technique. The displacement of the reflected beam is proportional to the deflection of the cantilever; (b) interferometer technique. (b) was from Roseman [49].

end close to the cantilever is cleaved, reflecting 4% of the light intensity back into the fiber at the fiber/air interface with an intensity $I1$. This beam will interfere with the light beam $I2$ reflected into the fiber from the cantilever beam. The total intensity I of the light at the photodiode is then fiber-cantilever separation dependent. If the experiment is operated at the most sensitive cantilever fiber separation of $n\lambda/4+\lambda/8$, where n is an integer, the cantilever deflection can be quantitatively obtained by

$$\delta a = \frac{\lambda}{2\pi} sin^{-1} \frac{\delta I}{\delta I_{max}}, \tag{2.11}$$

where a the fiber-cantilever separation, λ is the light wavelength, 785 nm, and δI_{max} is the maximal intensity change between constructive and destructive interference. During experiments, the separation of the fiber to the cantilever backside is less than 5 μm to minimize the laser phase noise.

2.2.3 Phase Locked Loop

A PLL is used to directly monitor the cantilever's resonance frequency shift [50]. Two different phase locked loops have been used, one is analog [37] while the other one is digital from NanoSurf [51]. The analog one has a large bandwidth of 10 kHz, while the digital one has selectable frequency windows of 183.3, 366.7, 733.3 and 1466.7 Hz.

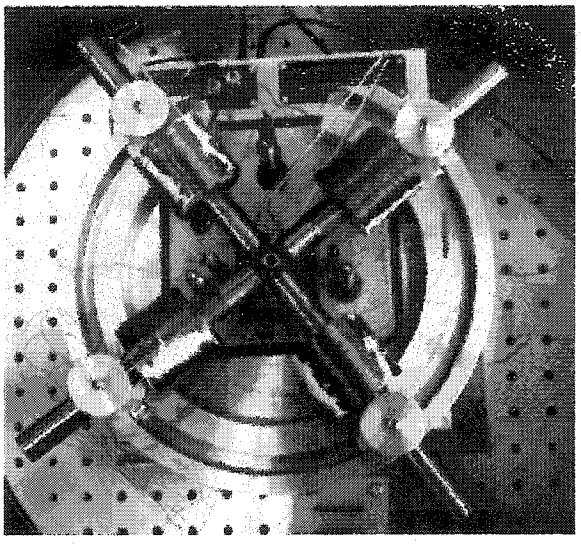

Figure 2.7: top view of two pair of electromagnets. A sample is mounted in the center of the air gap on the top of the piezo scanner.

2.2.4 *Electromagnets*

Two pairs of *in-situ* electromagnets are used to apply in plane magnetic fields along the x and y direction, as shown in Figure 2.7.[1]

2.3 *Noise Analysis and Sensitivity*

2.3.1 *Sensitivity of vacuum magnetic force microscopy*

Thermal energy will induce Brownian motion of the cantilever. Treating the cantilever as an isolated one dimensional harmonic oscillator, which has two degrees of freedom, the total thermal energy will be k_BT. The RMS noise of the lever can then be written

[1]The electromagnet is composed of soft iron bars with a diameter of 1/2″, an air gap of 1/2″; the end of the bar is tapered to 45°. There are 4,000 turns of insulated copper wires wound on each bar. The center of the air gap can achieve 1000 Oe while applying 250 mA current. The field in the scanned area, typically less than 100μm is very homogenous. The field is measured with a Hall probe, which is calibrated with a calibrated Gaussmeter. The electromagnet produce negligible heat while applying 50 mA current to the electromagnets, however it will produce heat considerably while applying 250 mA in vacuum, which can induce cantilever drift.

as,

$$< \delta a^2 >^{1/2} = [\frac{4k_B TB}{k_{cb}\omega_0} \frac{Q}{Q^2(1-\omega^2/\omega_0^2)^2 + \omega^2/\omega_0^2}]^{1/2}, \tag{2.12}$$

where T is the absolute temperature, ω_0 is the resonance frequency of the cantilever, k_B is Boltzmann's constant, k_{cb} is the spring constant of the cantilever, Q is the quality factor of the cantilever, and B is the bandwidth.

For an ideal MFM system, the sensitivity should be limited by cantilever thermal noise. The minimal detectable frequency shift is then [34],

$$f'_{min} = \frac{1}{A_0}(\frac{4k_{cb}k_B TB}{\omega_0 Q})^{\frac{1}{2}}, \tag{2.13}$$

where A_0 is the mean-square root amplitude of the cantilever oscillation amplitude, and B is the bandwidth.

Ideally, it is possible to tailor all the parameters such as A_0, Q, T, to achieve high sensitivity measurements. However, for a real system, there are other noise sources such as environmental vibration noise, deflection sensor noise, preamplifier Johnson noise, transducer (Bimorph) noise, feedback noise, electronic $1/f$ noise, back action forces on the cantilever from deflection sensor, or even Heisenberg noise (uncertainty of cantilever position). In some circumstance, it is not the cantilever thermal noise but these noises that determines the MFM sensitivity. Detailed discussion of these noise contributions can be found in the literature [47, 49, 52].

Under ambient conditions or in vacuum, thermal noise of the cantilever near resonance usually is a few orders of magnitude larger than other noise sources. Thermal noise limited sensitivity can thus be achieved in a well designed system. To determine the sensitivity of our system, we perform 'empty' scans, which are similar to a normal scan, however, there is no sample close to the tip. The cantilever frequency signal, decoded by the PLL, is acquired with the data acquisition system. Fig. 2.8 shows the frequency histograms of two recorded images at two different cantilever oscillation amplitudes. Each image has 128 by 128 pixels, and each was acquired in

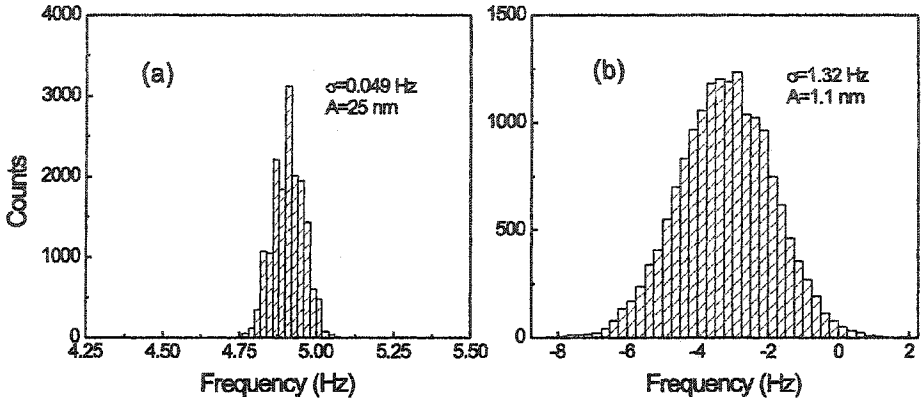

Figure 2.8: The frequency noise histogram at two different cantilever oscillation amplitude. (a) 25 nm, (b) 1.1 nm. Cantilever: $k = 0.7 \pm 0.1 N/m$, $f_0 = 64.49$ kHz, Q=3100, B=120 Hz.

two minutes. As expected, the standard deviation of the frequency signal is small (0.05 Hz) for large oscillation amplitudes (25 nm), while it is large (1.32 Hz) for small oscillation amplitudes (1 nm). Fig 2.9 shows the plots of the frequency RMS noise as a function of the oscillation amplitude. Solid dots were decoded by a digital PLL [51], while the empty dots were taken by an analog PLL [50]. The frequency noise of the digital PLL can be fitted by

$$f_{rms} = cA^{-0.97\pm0.03}, \tag{2.14}$$

which is in excellent agreement with the theoretical prediction (Eq. 2.13). The minimal detectable force gradient is about 1×10^{-6} N/m with an oscillation amplitude of 25 nm.

This agreement with theoretical expectations indicates that the sensitivity of our microscope is thermally limited while performing regular MFM imaging. This is not surprising, since the thermal noise at room temperature is usually orders of magnitude higher than other noise sources, such as deflection sensor noise. A deviation from the thermal noise limited sensitivity can appear when other noise sources are dominant. For example, when we use the analog PLL to decode the frequency signal,

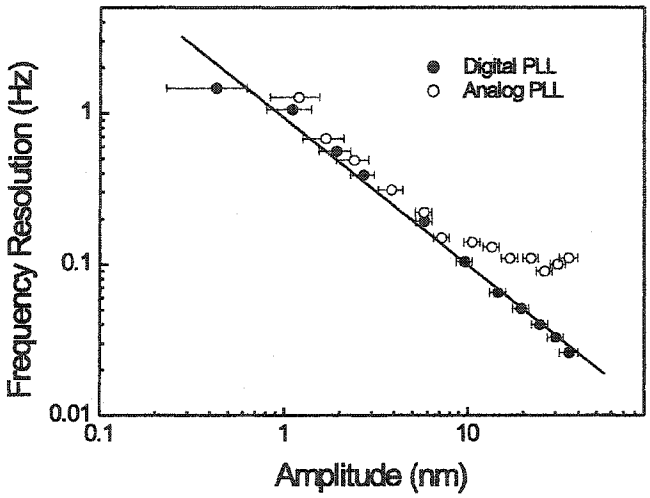

Figure 2.9: RMS noise of the frequency signal as a function of the cantilever oscillation amplitude. Solid dots: digital PLL, Open dots: analog PLL. The solid line is a best fit to DPLL data by equation $y = cx^{-0.97\pm0.03}$ with $c = 1.18 \pm 0.10$. Cantilever: $k_{cb} = 0.7 \pm 0.1$N/m, $f_0 = 64.49$ kHz, Q=3100. 1 Hz corresponds to 2×10^{-5}N/m

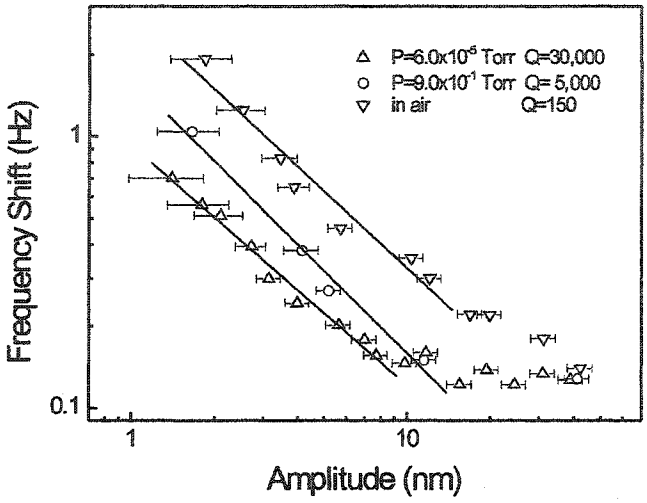

Figure 2.10: The sensitivity at different pressures. Cantilever: $k_{cb} = 1.3 \pm 0.2 N/m$, $f_0 = 60.849$ kHz. Analog PLL was used. The data can be fitted to $A^{-0.94 \pm 0.07}$ in air, $A^{-1.0 \pm 0.06}$ for $P = 9.0 \times 10^{-1}$ Torr and $A^{-0.88 \pm 0.06}$ for $P = 6.0 \times 10^{-5}$ Torr, respectively.

the frequency noise is saturated at large cantilever oscillation amplitude (>10 nm), as shown in the open dots in Fig 2.9. This can be understood when comparing the two PLLs: the analog one has a much larger bandwidth than the digital one, which results in larger electronic noise. The deviation shows up prominently at low temperatures, when the thermal noise is largely suppressed. Roseman demonstrated that his low temperature MFM is optical shot noise limited when using the analog PLL [49].

2.3.2 *Sensitivity Improvement*

To fundamentally increase the sensitivity, one needs to choose a proper cantilever, to use large oscillation amplitudes, to work in vacuum, or to cool down the temperature as low as possible.

- Increasing the cantilever oscillation amplitude A

The signal to noise ratio can been increased by increasing the cantilever oscillation amplitude, as shown in Fig. 2.9. For MFM imaging, we find that it is reasonable to oscillate the cantilever amplitude on the order of 10 to 50 nm for standard commercial MFM cantilevers.

- Operating in the vacuum

The direct consequence of operating the MFM in a vacuum is to increase the Q-factor of the cantilever, thus decreasing the thermal noise off resonance. The sensitivity improvement can be demonstrated in Fig. 2.10. The frequency noise as a function of the cantilever oscillation amplitude is plotted for three different conditions: in atmosphere, at a pressure of 9×10^{-1} Torr, and at 6×10^{-5} Torr. As pressure goes down, the curve shifts to the left, a result of the improvement in sensitivity. All data show an $A^{-\alpha}$ drop with α of 0.9 to 1, as expected. However, for a fixed A, we found that the sensitivity improvement cannot be fitted by $Q^{-1/2}$, and there is a crossover to domination by the analog PLL electronic noise easily observable in vacuum.

- Decreasing the ratio of $k_{cb}/\omega_0 Q$.

As the cantilever thickness is on the order of micrometers, the Q-factor of the cantilever is still determined by bulk parameters. Only for thinner silicon cantilevers do surface effects play a role. Therefore, reducing the value of k_{cb}/f_0 can increase the sensitivity.

For rectangular cantilevers, the cantilever spring constant can be written as

$$k_{cb} = \frac{Ewt^3}{4l^3}, \tag{2.15}$$

and the cantilever resonance frequency can be written as,

$$f_0 = 0.162\frac{t}{l^2}(\frac{E\gamma}{\rho})^{1/2}, \tag{2.16}$$

where E is the modulus of elasticity, w is the cantilever width, l is the cantilever length, t is the cantilever thickness, ρ is the mass density. Therefore,

$$k_{cb}/f_0 \approx wt^2/l. \tag{2.17}$$

The sensitivity can be increased by using narrower, thinner and longer cantilevers. This can only be done by custom micromaching. For very thin cantilevers (< 100 nm), surface passivation needs to be done to optimize Q. However, based on Eq. 2.16, the resonance frequency will be smaller if a thinner, narrower, and longer cantilever is used, and it can be an undesirable factor for a real experiment, as other noise sources will have more contribution to the total noise at low frequency. One needs to optimize these two parameters (thermal noise limited sensitivity and resonance frequency) according to a real system.

- Operating at low temperature

Operating the system at low temperature can substantially suppress the thermal noise. Usually at low temperatures, thermal noise is not the main noise contribution, even though the thermal peak still can be observed. Great care must be taken to minimize contribution by other noise sources such as vibrations and deflection sensor shot noise [53].

2.4 Some Examples

2.4.1 Magnetic force microscopy imaging

MFM is a tool used to obtain the domain patterns of magnetic samples. The stray field or field gradient close to the domain wall is different to that inside a domain. By mapping the stray field or field gradient, the magnetic domain structures can be obtained. Fig 2.11 show two typical domain patterns in 20 μm permalloy square samples and their corresponding patterns obtained by micromagnetic simulation.

Fig 2.12 shows the domain structures in an iron whisker sample.[1] The Bloch walls (black or white lines in the scanned area) can be revealed. On both sides of the wall, the magnetic moments are antiparallel to each other with moments aligned in the plane, and the Bloch wall is a transition area through which the moment direction

[1]The sample was supplied by Bret Heinrich of Simon Fraser University.

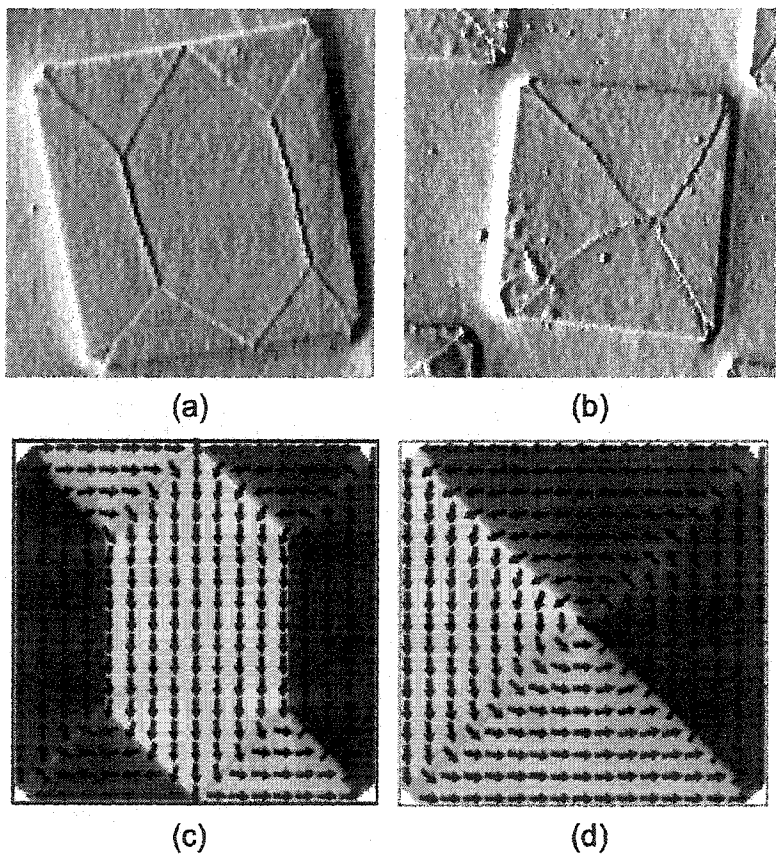

Figure 2.11: (a) and (b) MFM images of two 20 μm permalloy square with thickness of 20 nm. The domain patterns form flux closure structures with seven domains and four domains respectively. Tip: 15 nm $Co_{71}Pt_{12}Cr_{17}$, in constant frequency shift mode. Besides the domain patterns, the topography contrast also appears in the images. The images were differentiated along the fast scan direction to enhance the contrast. (c) and (d) magnetic moment patterns obtained by micromagnetic simulation. The simulation size has the same dimension as the real sample, but the unit cell was chosen to be $25^3 nm^3$, much larger than the exchange length of permalloy sample, 10 nm, limited by the capability of the computer memory. The micromagnetic simulations still show similar patterns as the experiments.

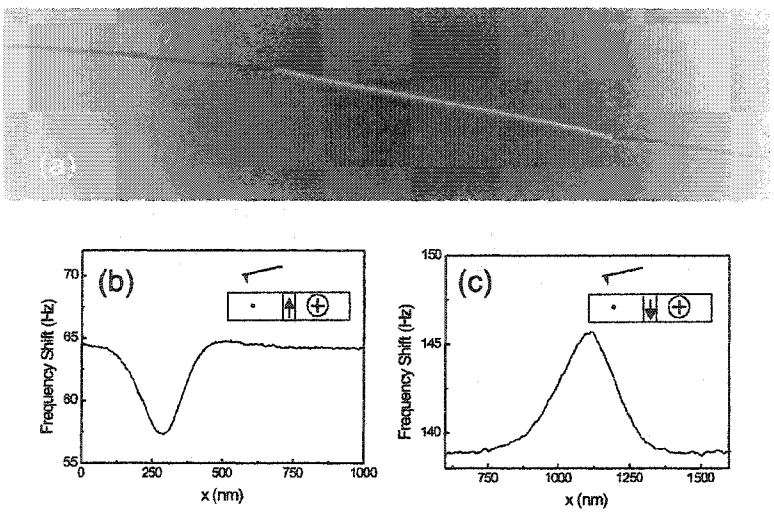

Figure 2.12: (a) The Bloch walls in an iron whisker sample, scan size: $100\mu m \times 25\mu m$, constant frequency shift mode in vacuum; parabolic backgroud is from the x-z coupling of the piezotube scanner; (b) and (c) typical line scans across the Bloch walls. Constant height mode scan. Tip: f_0= 40.4 kHz, k_{cb}= 0.13 N/m, tip coating: 30 nm $Co_{71}Pt_{12}Cr_{17}$, tip sample separation: 100 nm, oscillation amplitude: 10 nm.

gradually rotates 180 degree from one side to the other. The average magnetic moments inside the wall can point out of or into the plane. As a consequence, the MFM tip will feel an attractive or repulsive force on the walls depending on their polarities. Typical scan lines across both walls are shown in Fig 2.12 (b) and (c). When the wall moment direction is the same as the tip moment direction, the tip will feel an attractive force (force gradient) and the cantilever resonance frequency will become smaller. The opposite happens when the magnetic moment direction of the wall is antiparallel to the tip's; the MFM tip will feel a repulsive force. Bloch wall segments with different polarities are not aligned in a straight line, instead, they are kinked (Bloch line). The appearance of the kink and Bloch lines can help reduce the wall magnetostatic (stray field) energy [16].

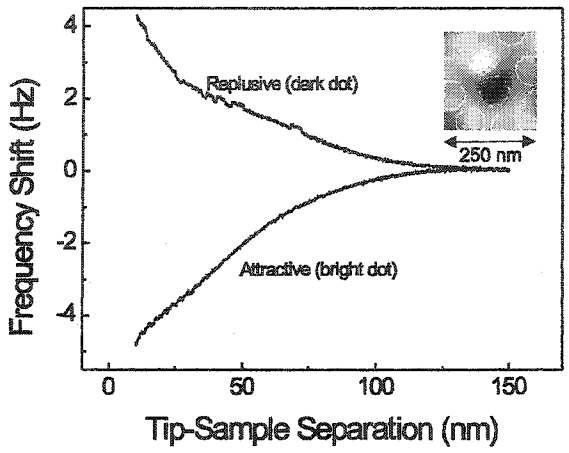

Figure 2.13: Force distance curves on two different Ni dots): one has a magnetic moment direction opposite to the tip stray field, while the other has the moment direction parallel to the MFM tip. By performing force spectroscopy, these different magnetic states can be identified. The MFM images of the dots is shown in the inset, and the dots are circled for clarity. Raw data were shown.

2.4.2 *Force Spectroscopy Imaging*

MFM is not just a tool to perform domain imaging. Force spectroscopy imaging can be performed to clarify the nature of interactions. Fig 2.13 shows such an example. The inset of Fig 2.13 shows an MFM image of Ni dots.[1] One dot shows dark contrast, another one shows bright contrast. This relative contrast cannot indicate the moment states of the dots, since an MFM image is a two dimensional contour of force gradient. However, force distance curves show that the interaction between the black dot and the tip is repulsive, while it is attractive between the tip and the white dot. This result indicates that one dot has the moment direction parallel to the MFM tip, while the other is antiparallel.

[1]Ni dot arrays with a dot diameter of 50 nm and 30 nm thickness were prepared with a nonlithographic technique utilizing a highly ordered anodized aluminum oxide porous membrane as a template, supplied by Jimmy Xu and Jianyu Liang (Brown University). Details about the preparation can be found in the paper by Liang [13].

2.5 Tip Induced Distortion on Large Sample

MFM monitors the magnetic force or force gradient between the tip and sample, which is determined by both the tip and sample moment distribution. However, during MFM imaging, the tip and sample can be very close to each other, therefore the presence of the tip stray field (sample stray field) can potentially change the sample (tip moment) distribution. Such distortion can be extremely severe if either the tip or the sample is magnetically soft. Grütter et al. have demonstrated that the stray field of magnetic tracks from longitudinal recording disks can completely reverse the NiFe thin film tip moment direction [54]. In most cases, it is however the MFM tip stray field that disturbs the sample magnetic state, especially while studying magnetically soft samples [55, 56].

Undisturbed force gradient images can only be obtained when a very low magnetic moment tip is used. However, the direct consequence of using such low moment tips is a reduction of the measurable magnetic signal. The smallest usable tip moment is limited by the sensitivity of the MFM system.

2.5.1 Reversible Distortions

The MFM tip stray field distortion can be reversible or irreversible. The MFM tip stray field can locally, reversibly oscillate domain walls or locally magnetize the sample. Fig 2.14 shows such an example. Fig 2.14 (a) shows a domain image at large tip-sample separation, while Fig 2.14 (b) shows the image at a closer separation. Close scanning leads to much better spatial resolution, and a fine domain structure can be seen clearly. However, the distortion is also obvious, as some domain walls become curved and highly localized domain wall displacements, as sketched in the image, can be observed. As the tip-sample separation becomes larger, the domain structure reverts back to (a).

The MFM tip stray field can locally magnetize the sample, which can be demonstrated by measuring the force distance curve on a whisker sample (Fig 2.15). There

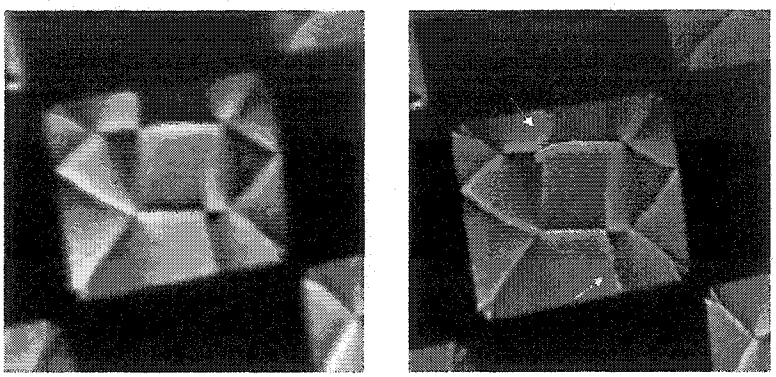

Figure 2.14: MFM image of Permalloy square: (a) large tip-sample separation (200 nm), (b) small tip-sample separation (50 nm). Constant height image; tip: 50nm CoPtCr; Q=42,000; f_0=63.183kHz.

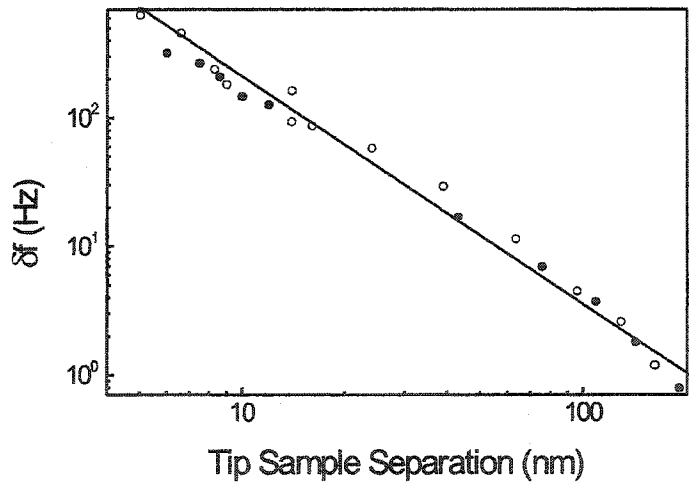

Figure 2.15: Cantilever frequency shift versus the tip and sample separation. Sample: iron whisker; tip: 30 nm CoPtCr; f_0=40.4 kHz, $k_c b$=0.13 N/m. The MFM tip stray field can reversibly rotate the magnetic moment underneath the tip. The cantilever frequency shift as a function of tip-sample separation. Black dots and white dots were taken at different location of the sample.

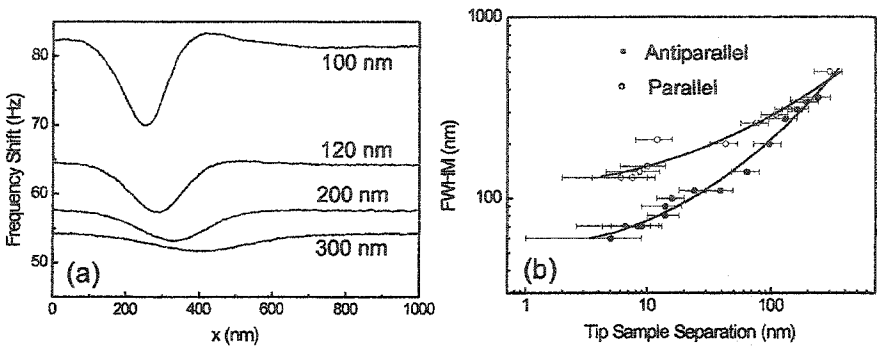

Figure 2.16: The MFM tip stray field can reversibly magnetize domain walls. (a) A series of line scans at tip-sample separations of 300 nm, 200 nm, 120 nm, and 100 nm, respectively. (b) Full width at half maximum of two different polarized Bloch walls as a function of tip-sample separation.

is a strong long range attractive interaction between the tip and sample, even when the tip-sample separation is as large as 300 nm. This interaction is magnetic in origin, since the van der waals force and electrostatic force[1] are extremely small at such tip-sample separations. The existence of strong attractive interactions can also be demonstrated by the fact that the constant frequency shift mode imaging can be performed at zero bias voltage, even though there are two different polarities of the Bloch walls (Fig 2.12). Since the whisker sample is magnetically extremely soft, the attractive interaction is due to the MFM tip locally rotating the moment direction underneath the tip. Such phenomena are not detectable on magnetically hard samples, and are not obvious in thin films (< 50nm). For magnetically hard samples, the tip stray field cannot overcome the local coercivity. For thin films (even magnetically soft), the contribution of the attractive interaction is small due to the small volume and shape anisotropy. By fitting the force-distance curve in Fig. 2.15, we found a power law relationship between the frequency shift and tip-sample separation:

$$\delta f \sim d^{-1.8\pm0.1}. \tag{2.18}$$

[1]Small bias voltage was applied to to compensate the work function difference

The relationship cannot be explained by existing theory [57]. To fully understand this relationship, one needs to know the tip stray field and its distribution, as well as the local susceptibility. From a micromagnetic simulation point of view, one needs to minimize the total energy including the anisotropy energy, exchange energy, magnetostatic energy, and Zeeman energy in the presence of an inhomogeneous tip stray field.

The reversible distortion can also be demonstrated with a final example: reversible magnetization of domain walls. If a magnetic field has the same direction as the moment direction of the wall, the thickness of the wall will grow. An opposite field will lead to a reduction of the wall width. We perform line scans across the Bloch wall separately with different polarities (Fig. 2.12 (b) and (c)) as a function tip-sample separation (Fig 2.16 (a)). As the width of the line scan profile should be directly proportional to the wall thickness, we plot the full width at half maximum (FWHM) of the profile in Fig. 2.16 (b). The width of a wall with a moment direction opposite to the tip moment direction is thinner than that of a wall with moment parallel to the tip moment. Potentially, one should be able to quantify the tip stray field by combining micromagnetic simulations with this experimental data. In passing, it is worthwhile pointing out that analyzing reversible tip induced sample distortions to characterize local sample magnetic parameters is still at its infancy and could be explored more in the future.

2.5.2 Irreversible Distortion

The MFM tip stray field can not only reversibly change the sample's moment direction, but it can also lead to an irreversible change in the sample's magnetic structure. A wall will move if the tip stray field is bigger than its local pinning potential. If the wall is moved to a new local energy minima in this process, the wall will not return to the original position even when the tip stray field is removed. Such irreversible distortions are observed rather often if large moment tips are used.

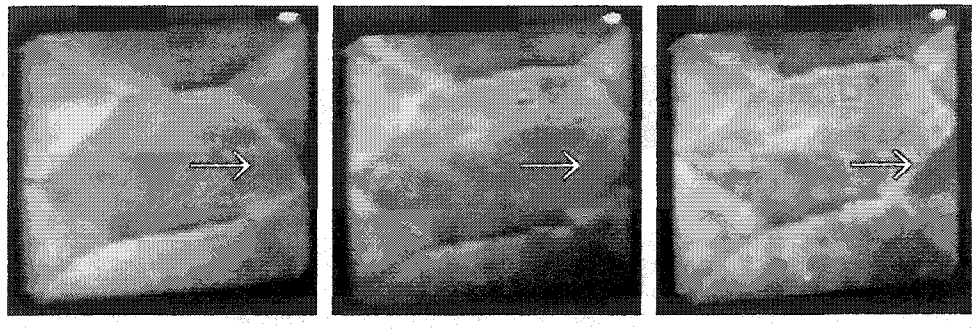

Figure 2.17: Magnetic domain structures acquired at three different tip-sample separations: (a) far; (b) close; (c) far. The MFM tip stray field irreversibly moved the domain wall during the second scan. Tip: 20 nm Fe, $f_0 = 67.78$kHz, $Q = 36,000$, k=1.5 N/m, $P = 6.7 \times 10^{-5}$Torr. Constant frequency shift mode. Square box in the images marks a dust particle using as a marker. The arrows point to a large change of the position of a wall.

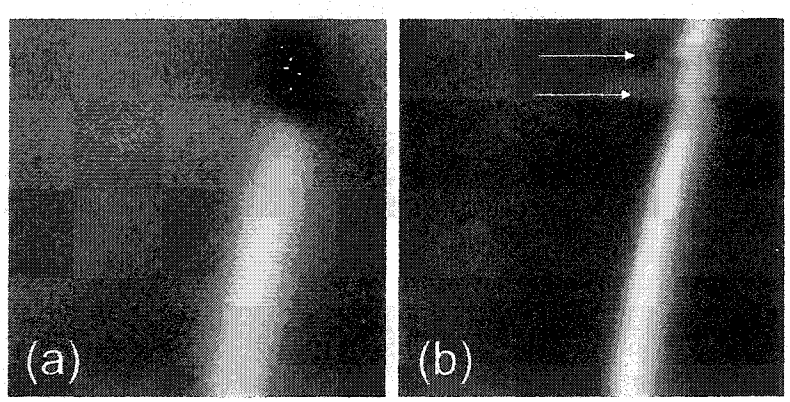

Figure 2.18: MFM image (a) Bloch wall at large the large tip-sample separation (120 nm); (b) for small tip-sample separation (30 nm). Scan size: $1\mu m$. Tip: 50 nm $Co_{71}Pt_{12}Cr_{17}$, Q=3,000, k_{cb}=0.13 N/m, f_0=40.699 kHz, A=4 nm. Constant height mode imaging.

Fig. 2.17 shows three consecutive scans on a Permalloy square. The images were taken in the constant frequency shift mode, so the absolute value of the tip-sample separation is unknown. However, the second scan has a larger frequency shift set point than the other two – the tip is thus closer to the sample during the second scan. We observe that the tip moves the domain wall during the second scan. Comparing the images of Fig 2.17 (a) and Fig. 2.17 (c), it can easily be concluded that the domain wall was irreversibly moved by the tip stray field.

Fig. 2.18 shows two images at different tip-sample separations on the Bloch walls of a iron whisker sample. In Fig. 2.18 (a), the Bloch line and the kink of the domain wall can be clearly seen. At a small tip-sample separation, the tip stray field induces the Bloch line jumps as indicated by the arrows. As a consequence, the antiparallel wall segments (dark contrast) disappear from the field of view, and the orientation of the wall also changed (the kink disappears).

2.6 Summary

- The sensitivity of the magnetic force microscopy is demonstrated to be thermally limited. The sensitivity is largely improved by using larger oscillation amplitude of the cantilever, using a digital PLL, and operating in vacuum.

- MFM tip stray field can reversibly or irreversibly rotate the magnetization state of a two dimensional sample depending on the tip-sample separation, local pinning potential of domain wall and the stray field of the MFM tip.

3

Imaging, Manipulation, and Magnetization Switching

This chapter presents the versatility of magnetic force microscopy to study the magnetic structures of nanoparticles: imaging, manipulation, and spectroscopy. The MFM tip stray field can not only locally irreversibly change the magnetic state of an individual magnetic particle, but it can also be used to manipulate this state. Controlling of the tip stray field induced distortion can be achieved by using an appropriate tip coating and tip-sample separation. Spectroscopy is performed by measuring the force gradient as a function of tip sample separation. This MFM operation mode can also be performed in the presence of a magnetic field, which allows the characterization of the magnetic switching behavior of individual elements. Imaging in the presence of external fields can be used to characterize the switching field of the elements. In the following, the general characteristics and implementation of these methods especially when applied to small magnetic particles will be described, and application of using these techniques to study elongated submicron and sub 100 nm Permalloy ($Ni_{81}Fe_{19}$) elements is presented.

3.1 Imaging of Nanomagnets

If the size of a magnetic element is below a certain critical value (R_c in the Eq. 1.1), a domain wall will not form and the most stable state is then uniformly magnetized state. Such critical value varies as a function of the materials. For Permalloy, the critical size is about 100 nm. However, for elongated elements with large aspect

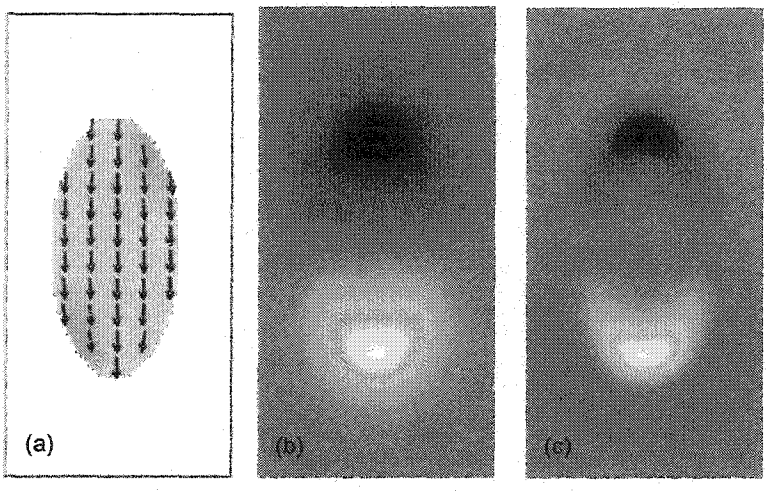

Figure 3.1: (a) The moment distribution in a 300 nm × 150 nm with 5 nm thick permalloy ($Ni_{81}Fe_{19}$) particle, obtained by micromagnetic simulation with unit cell size of 5 nm. There is no domain wall inside of the element. (b) Stray field distribution of the nanoparticle at the plane 40 nm above the particle, bright and dark contrasts correspond to the south and north pole; (c) Stray field gradient distribution at the same plane as (b), which shows similar contrast. However, the contrast is more localized.

ratios, even though the element size is still larger than the critical size, due to shape anisotropy, the magnetic moments align along the long axis, thus forming a single domain state. Fig 3.1 show the magnetic moment configuration inside a Permalloy element of size 300 nm × 150 nm × 5 nm,[1] obtained by micromagnetic simulation. As shown in Fig. 3.1 (a), all the magnetic moments align along the long axis with a little curling close to the edge. This curving of the moment at the edge is the result of the inhomogeneous demagnetizing field. Fig 3.1 (b) and (c) show the stray field and stray field gradient in a plane 40 nm above the element. If the MFM tip is an infinite long dipole, Fig 3.1 (c) should be equivalent to an MFM image.

However, a real MFM image can never be the same as Fig. 3.1(c) due to the MFM tip's convolution and other forces besides the magnetic interaction involved. In the previous chapter, the basic operating modes, such as constant frequency shift mode, tapping/lift mode and constant height mode, have been discussed. Different operating modes can lead to different levels of convolution between topography and

[1]The element size is defined by *Length* × *Width* × *Thickness*.

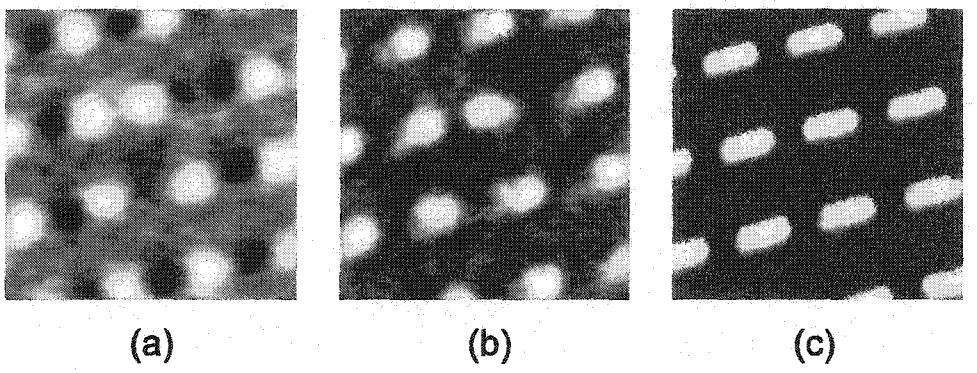

Figure 3.2: Three images of different frequency shift set points: (a) small frequency shift (80 Hz), (b) medium frequency shift (87 Hz), (c) Large frequency shift (120 Hz). $\delta z \sim 25$ nm for (a) $\rightarrow$ (b), and $\Delta z \sim 20$ nm for (b)$\rightarrow$(c). For small frequency shifts, corresponding to large tip-sample separation, the frequency shift mainly comes from magnetic interactions, and single domain structures can be observed. For medium frequency shifts, the single domain structures are not obvious. For large frequency shifts, mainly topography contrast appears. An array of 800nm $\times$ 200nm $\times$ 30nm permalloy particles, Tip: 50 nm $Ni_{50}Co_{50}$. Bias voltage: U=2.5 V.

magnetic signal.

The constant frequency shift mode is the worst one, since the applied bias voltage (used to achieve stable feedback operation) magnifies the topography signal due to the strong electrostatic force gradient present. As a result, the observed contrast depends both on the bias voltage and the set point of the cantilever resonance frequency f_0', maintained by the feedback loop. Fig 3.2 shows such an example. Due to shape anisotropy, the magnetic elements form single domain states with magnetic moments lying along the long axis. For a small frequency set point, giving rise to a large tip-sample separation, the bipolar contrasts associated with the single domain states (Fig 3.2 (a)) (black and white) can be observed, while for a large set point, i.e. a small tip-sample separation, the bipolar contrast is gone, and only the topography contrast appears, as shown in Fig 3.2 (c). For a medium set point, the observed contrast (Fig 3.2 (b)) is a mixture of (a) and (c). Magnetic and electrostatic interactions are both long range forces, the magnetic interaction however decays more slowly. For large tip-sample separations (on the order of a few hundred nanometers), the magnetic interaction is dominant, and the observed contrast is magnetic [20].

However, as the tip-sample separation becomes smaller, the electrostatic force plays a significant role, and leads to a strong convolution between topography and magnetic signal. In general, to observe magnetic contrast, the set point (the frequency shift setting) should be small as the electrostatic interaction is optimized (stable feedback versus minimal tip sample crosstalk), or the tip moment needs to be large, i.e., etched magnetic wire or thick coating, making the magnetic signal dominate over the electrostatic one. However, the consequence of using a large magnetic moment tip is to potentially irreversibly change the sample magnetic state, while the drawback of choosing a small set point (i.e., a large tip-sample separation) is that it leads to a weak magnetic signal and poor spatial resolution. For example, Fig 3.3 (a) shows an MFM image of a permalloy dot array with the element size of 715 nm $\times$ 148 nm $\times$ 50 nm, taken from reference [58]. Even though the bipolar contrast is observable, the signal to noise ratio is low, and the spatial resolution is poor.

The tapping/lift mode and the constant height mode can separate the magnetic signal from topography. In the constant height mode, the tip flies above the sample at a constant height (see Fig. 2.3(c)). For a small bias voltage with a sharp MFM tip, even if the topography is not flat, with moderate tip-sample separation (50 nm), the electrostatic force and the van der Waals force gradient can be very small, on the order of 10^{-6}N/m, which is very close to the minimal detectable signal of our MFM. The magnetic force gradient however can be much larger than the van der Waals and the electrostatic force gradient for a proper magnetic moment tip at moderate or even small (20-30 nm) tip-sample separation, and the observed contrast is then magnetic. Fig. 3.3 (b) shows an MFM image of an array with a particle size of 240 nm $\times$ 90 nm $\times$ 10nm. Compared to Fig. 3.3 (a), both the signal to noise ratio and the spatial resolution are substantially increased.

In the literature [12, 30, 31, 59–62], the tapping/lift mode has been widely used as it is implemented on all commercial MFMs due to its attractive feature of obtaining topography and magnetic signal simultaneously. However, both experimental results

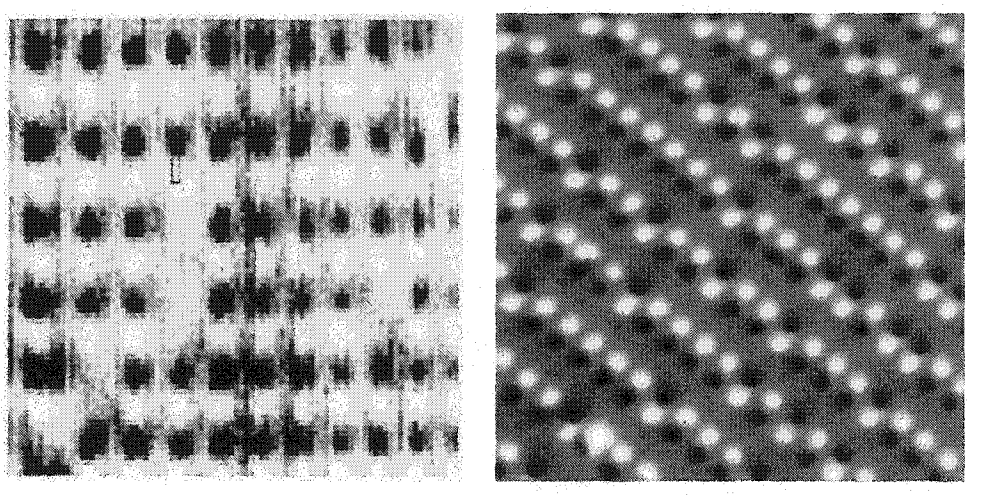

Figure 3.3: (a) Constant frequency images on an array of Permalloy elements with the element size of 715 nm × 148 nm and the thickness of 50 nm, separated by 1.41 μm and 1.78 μm in the x and y direction respectively; tip: etched Ni wire; in air; from [58]; (b) Constant height images on an array of permalloy elements with the element size of 240 nm × 90 nm and the thickness of 10 nm. Force Sensor: 30 nm $Co_{71}Pt_{12}Cr_{17}$, $f_0 = 22.6$kHz $k_{cb} = 0.08$N/m. Tip-sample separation: 70 ± 10 nm. In Vacuum. Gray scale: 1.5 Hz, 1.1×10^{-5} N/m.

and simulation indicate [63] that there is only a very narrow margin of operation that can be used for tapping mode scan where small forces act on the tip, i.e. attractive mode. Beyond that operational window, force and power dissipation are very substantial, and the MFM tip does not remain sharp for a long period of time. Under ambient conditions, a water layer and other contaminations on the surface can make this even worse. Another disadvantage of using tapping/lift mode is that it has the potential to irreversibly change the sample magnetic state during tapping, as will be shown later in section 3.3.1. This is because during tapping the tip is very close to the sample and can apply a substantial field to the sample.

3.2 *Characteristic of MFM Tip Stray Field*

MFM does not have a good history of directly quantifying sample magnetic moments due to the unknown tip stray field and the potential of tip and sample mutual dis-

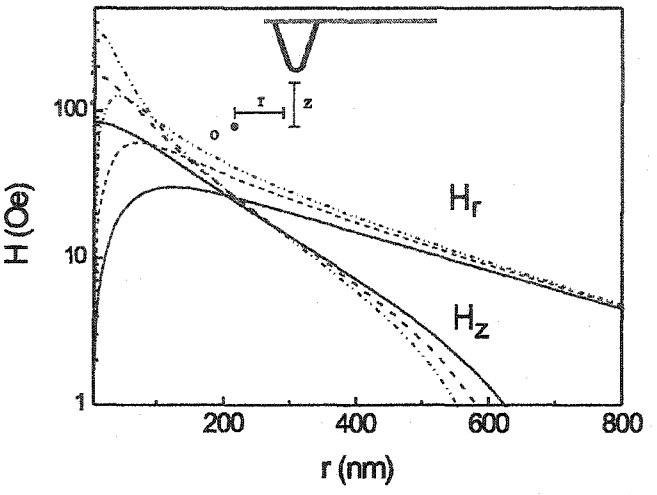

Figure 3.4: Calculated tip stray field of a low moment tip as a function of lateral distance r and at different z, indicated in the inset; solid line: z=100 nm, dash line: z=50 nm, dash dot dot line: z=20 nm. Tip: 30 nm $Co_{71}Pt_{12}Cr_{17}$. The tip is schematically shown in the inset.

tortion. Therefore it is crucial to quantify the tip stray field and to study the effects of MFM tip stray field induced distortion of a sample's magnetic state. Recently, the tip's stray field has been quantified by sophisticated techniques, such as micro-Hall sensors [64], Lorentz electron tomography [65], and electron holography [66]. The tip stray field can also be obtained by quantitative calibrated MFM [67]. It is found that model calculations seem to give a reasonable estimate of the tip stray field [20]. In our model calculation, we assume the tip has a conical geometry, and the coated magnetic material forms a conical shell around the tip, as shown in the inset of Fig. 3.4. The cone half angles of the silicon tip before and after coating are both 17°. The radius of the silicon tip r_0 is 10 nm, while the radius of the coated tip R is assumed to be half of the total of the silicon tip radius and the coating thickness, which leads to equal thickness of coating. The tip is magnetized along the z direction in a field of 10^4 Oe, and the tip moment is assumed to be aligned along the z axis. The saturation magnetization of the coating material is 450, 800, 1000 emu/cm^3 for $Co_{71}Pt_{12}Cr_{17}$,

Tip coating	$Co_{71}Pt_{12}Cr_{17}$	$Co_{71}Pt_{12}Cr_{17}$	$Co_{71}Pt_{12}Cr_{17}$	$Ni_{81}Fe_{19}$
Thickness (nm)	15	30	50	60
H_z^{max} (Oe)	280	360	460	900
R_{eff}(z) (nm)	60	100	130	150
H_r^{max} (Oe)	60	120	160	320
R_{eff}(r) (nm)	240	280	400	420

Table 3.1: A list of tip stray field and field decays for some tips at z=20 nm. H_z^{max} and H_r^{max} are the maximum value of the tip stray field strength for the z and radial components respectively. R_{eff}(z) and R_{eff}(r) are the decay length for both z and radial components.

$Ni_{81}Fe_{19}$ and $Ni_{50}Co_{50}$ respectively. Fig. 3.4 gives a typical example of the stray field of a 30 nm $Co_{71}Pt_{12}Cr_{17}$ coated tip at various tip-sample separations (z) and different lateral distances (r). As expected, the stray field close to the tip end is substantial (a few hundred oersted at distances of a few tens of nanometers). The calculated stray field and decay characteristics are consistent with experimental data [65]. It is worth pointing out a less appreciated fact: the radial component is also substantial and decays much slower than that of the z component. At lateral distances of a few hundred nanometers, the radial component can thus be larger than the z component [59]. In Table 3.1, a list of some MFM tips used in our experiments as well as characteristic field strengths and length decay are presented. The field strength decay length R_{eff} is defined as the radial distance r at which the field strength has decayed to 50% of the maximum value. The decay length is of a few hundred nanometers for the radial component of the tip stray field. It is then easy to imagine that an MFM tip will lead to substantial distortion of the sample magnetic state for a sample with a dimension comparable to the decay length of the tip stray field.

3.3 Manipulation of Magnetic Moment States

The tip stray field locally distorts the sample magnetic structure in a two dimensional film, when the local tip field is larger than the local pinning potential of a domain wall. The magnetic structure is however only slightly modified by the tip, thus no global sample magnetization change will result. This is in contrast to the case of submicron magnetic particles. For particles of a few hundred nanometers in dimension, the associated magnetic torque by the tip stray field can extend over the entire particle volume. The magnetic state of a small particle as observed by MFM is thus expected to be potentially strongly influenced by the magnetic tip stray field. The direct consequence is that the tip can induce particle moment switching, especially for soft magnetic elements. This type of distortion is unavoidable in some cases, especially if experiments are performed in the tapping/lift mode due to the fact that the tip is extremely close to the particle while acquiring topography data.

3.3.1 MFM Tip Stray Field Induced Reversal During Tapping

Typical examples of the MFM tip stray field induced irreversible distortion are shown in Fig 3.5. Fig 3.5 (a-c) shows three consecutive scans on the same particle. The first image indicates that the magnetic elements form a single domain by showing bipolar contrast. The second scan shows that the particle has a double domain like structure. Inspection of the raw data shows that the contrast changed during a single scan line, indicating that the tip stray field reversed the particle's moment. The third image shows the same particle forming a single domain state, but with reversed orientation compared to the first image. We can conclude that the tip stray field reversed the particle magnetic moment in the second image. Fig. 3.5 (d) shows the scan of another particle. Multiple reversal processes can be observed during imaging. Fig. 3.5 (e-g) shows another example of three consecutive scans of a particle along the short axis. The MFM tip stray field induced particle moment reversal occurred during the second scan as indicated by the absence of the bipolar contrast. These kinds of

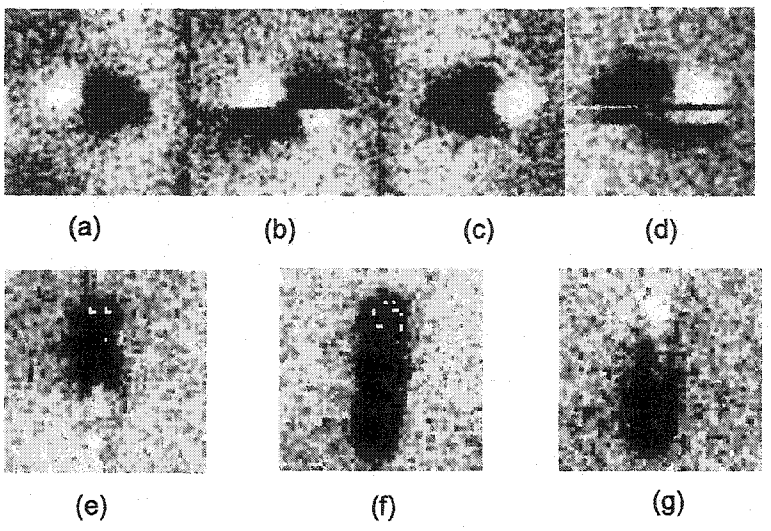

Figure 3.5: (a-c) shows three consecutive scans of the same 500nm×200nm ×30nm particle; (d) a scan on another particle with the same size as (a); (d-g) three consecutive scans along short axis of a element with size of 800nm× 200nm × 30 nm. The tip is a 60 nm Ni_81Fe_{19} coated probe, f_0 = 80kHz, k_{cb} about 1.5 N/m. The images were acquired in air using the tapping/lift mode with a lift height of 80 nm on a DI Multimode Nanoscope.

reversal are very common while performing tapping/lift mode scan. Data such as presented in Fig 3.5(b) and (f) can be (mis)interpreted as a multidomain state and can subsequently lead to wrong conclusions. Examples of this are surprisingly rather common in literature.

The occurrence of tip stray field induced magnetic reversals depends on the tip field strength and the switching field of the submicron magnet. Fig. 3.6 shows tapping/lift MFM images of the same location on an array with element size of $1\mu m \times 0.2\mu m \times 30nm$. Images were acquired in different scan directions, 0°, 180°, and 90° respectively. The scan procedure is sketched on the right side of Fig. 3.6 (c): the forward and backward scans of tapping, and the forward and backward scans in lift mode. The magnetic images were acquired in the backward scan. The lift height was chosen to be 120 nm, which we found empirically to give minimal tip stray field induced switching of the magnetic particle's magnetization. However, what is not negligible is the magnetic influence of the tip during tapping. For the 0° scan, Fig 3.6(a) shows that all the magnetic moments in the particles are oriented the same

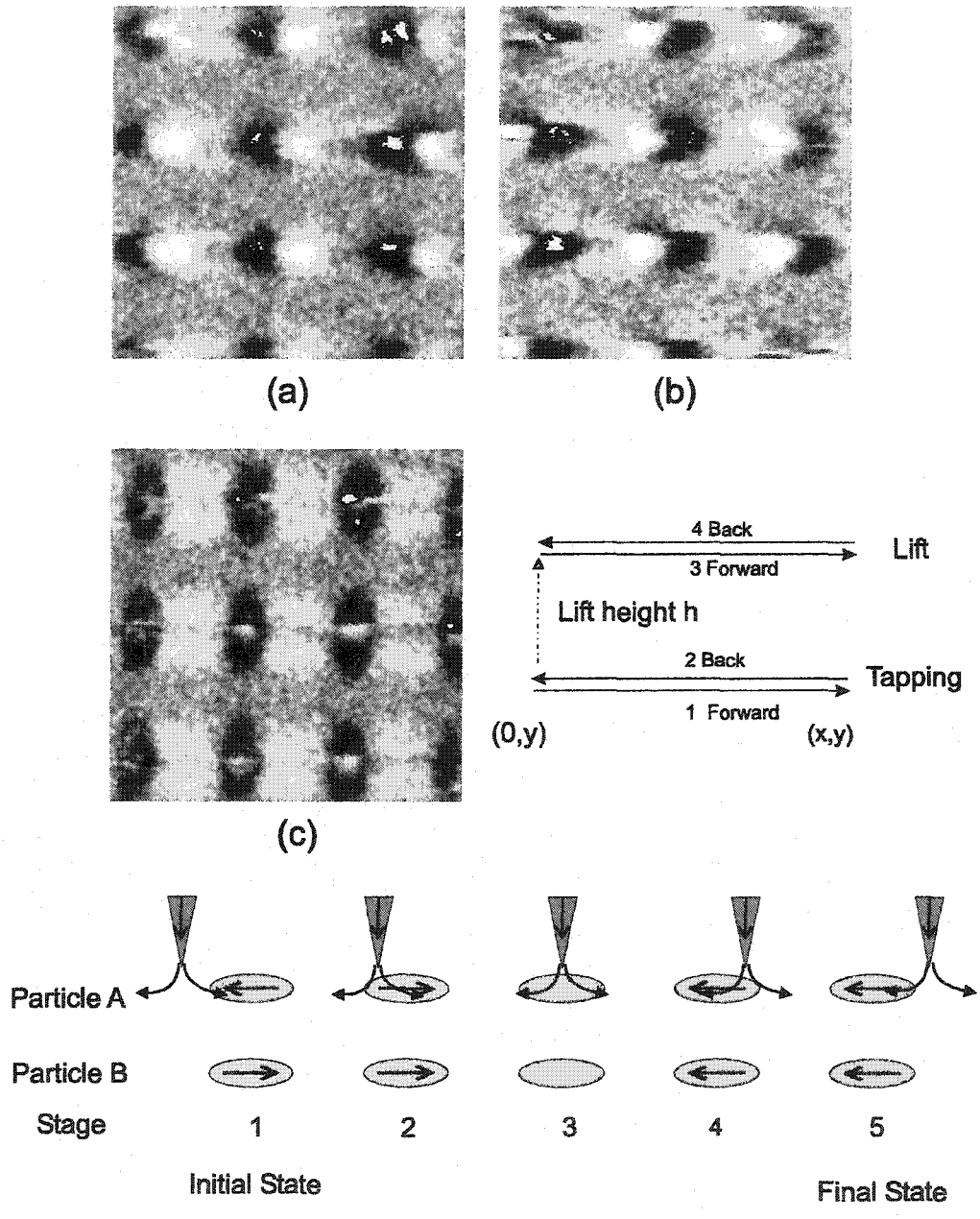

Figure 3.6: Three MFM scans of the identical area with scan directions: $0°, 180°$, and $90°$. Image (b) was off-line rotated to have the same orientation as (a). Tip: 50 nm $Ni_{50}Co_{50}$, Lift height: 120 nm, Particle size: $1.0\mu m \times 0.2\mu m \times 30nm$, in air, Multimode NanoScope. Schematic diagrams shows how MFM tip stray field switches the particles magnetic moments states. The scan procedure is indicated on the right side of (c).

with the left side being attractive (dark). If we now change the scan direction by 180°, Fig. 3.6(b) shows the magnetic orientation switches to the left side now being repulsive (bright). In order to make an easier particle by particle comparison between the two scan directions, the data of Fig 3.6 (b) was software rotated by 180°. Fig 3.6(a) and (b) indicates that the magnetic moments orientation in (a) are opposite to those in (b). Since we observe negligible influence while acquiring the magnetic contrast images (a result of the large lift height used), the reversal must happen while acquiring the topography during tapping. This is not that surprising, given that the tip is very close, if not in contact, to the sample during tapping. The schematic diagram at the bottom of Fig 3.6 shows the tapping scans on two individual particles A and B. Particle A and B initially have opposite moment orientations as shown by arrows. As the MFM tip scans from the left side to the right side during the tapping scan, a tip stray field induced reversal can occur. At stage 1, the tip is on the left side of the element, and the tip stray field strength is not big enough to overcome the coercivity of the particle. As the tip scans to position 2, the radial component of the tip stray field can be larger than the particle coercivity. As a result, the magnetic moments in particle A is switched to the opposite orientation, while the magnetic state of particle B remains. However, as the tip scans to position 4, the tip stray field can force the particle moments to be switched to the opposite direction. As a consequence, after the tapping scan, particle A and B have the same moment orientation determined by the initial (or final) position of the tip. The final magnetic state of a particle thus does not depend on its initial state, but only on the initial position of the tip. This type of tip influence is not detectable by just comparing the contrasts from backward and forward scan lines during lift mode (a commonly used method), since there is negligible influence while acquiring magnetic contrast for sufficiently large tip-sample separations. Instead, comparing the images from different scan directions is necessary. For example, if the scan direction is chosen to be 90°, i.e., scanning parallel to the particle's short axis, the bipolar contrast, representing

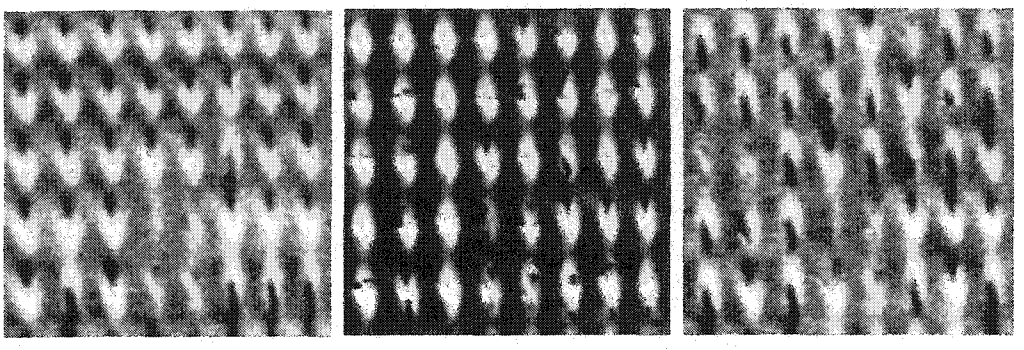

Figure 3.7: Influence of tip-sample separation on the observed magnetic particle structures. All images were acquired in the constant height mode at 120nm, 60nm and 120nm for images (a,b,c) with 30 nm $Co_{71}Pt_{12}Cr_{17}$ coated tip; permalloy particle size of 150nm×750nm, in vacuum.

attractive and repulsive interaction, disappears.

3.3.2 Tip Stray Field Induced Reversal in the Constant Height Mode

The occurrence of magnetization reversal is also tip-sample separation (h) dependent. Images in constant height mode with different tip-sample separation clearly demonstrate this. We found that not only large moment tips can reverse the orientation of the sample magnetic moment, but also small moment tips such as a 50 nm or 30 nm $Co_{71}Pt_{12}Cr_{17}$ tip. Fig 3.7 shows three consecutive images of the same array with different tip-sample separations, 120 nm, 60 nm, and 120 nm, respectively. In Fig 3.7 (a), a predominantly single domain structure is observed at the initial large tip sample separation of 120 nm. No sign of tip-induced sample magnetization reversal can be detected. Tip induced moment reversal can however be found for smaller tip-sample separations, as shown in Fig 3.7 (b). One observes the absence of bi-polar contrast. The reversed domain structures can be clearly seen by increasing the tip and sample separation back to 120nm as shown in Fig. 3.7(c). Some particles form a metastable low moment state (weak MFM contrast) after tip induced reversal.

Similar distortion can also easily be found on a perpendicularly magnetized dot in a constant height mode scan, as shown in Fig. 3.8. Fig. 3.8(a) shows an SEM image of

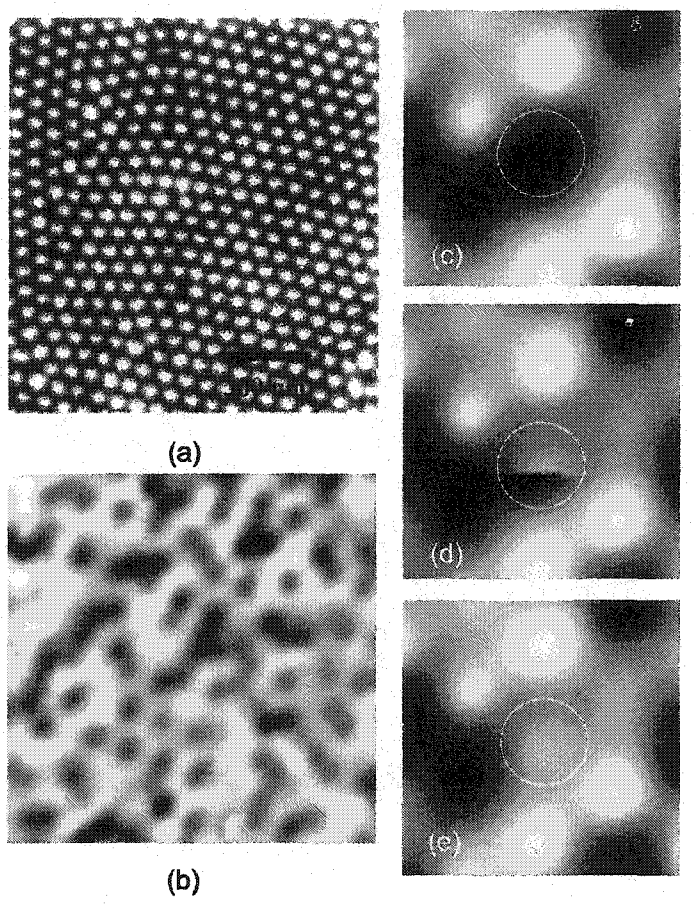

Figure 3.8: Tip stray field induced magnetization reversal in perpendicular magnetized Ni dots in the constant height mode. (a) SEM images of the Ni dot arrays, (b) large scan area $2\mu m \times 2\mu m$; (c-e) three consecutive scans in the area of 350 nm $\times$ 350 nm at different tip-sample separation: 80, 50, 50 nm. The tip stray field induced magnetization reversal occurs within the circled dot. Tip: 50nm $Co_{71}Pt_{12}Cr_{17}$, constant height mode in vacuum, the dot diameter is 50 nm diameter with a 30 nm thickness. The sample was supplied by Liang of Brown University, and the sample details can be found in [13].

the Ni dots, and (b) shows the MFM images of a $6\mu m \times 6\mu m$ scan area with 3.6×10^5 dots inside. The magnetic moments of the white dots and the gray dots point to the same direction as the tip stray field, while the dark and the black dots have the opposite moment direction to the tip stray field.[1] The local hexagonal symmetry can be seen in Fig. 3.8(b).[2] Fig. 3.8 (c-e) shows three consecutive scans at different tip-sample separations with scan sizes of 350nm $\times$ 350nm. Tip induced magnetization occurs in the central dot for smaller tip-sample separation (Fig 3.8 (d)), as indicated by the half dark and half gray contrast. In this case, the z component of the tip stray field is used to flip a particle's magnetic moment.

3.3.3 Controlling Magnetic States

By carefully controlling the height of the tip above a particle, reproducible switching into distinct magnetic states is possible. This is demonstrated in Fig. 3.9. By imaging at a constant height with a large tip-sample separation of 120 nm, we find that a 600nm $\times$ 150nm $\times$ 30nm particle forms single domain states (Fig. 3.9(a)). When the tip is located at position 'c' with smaller tip-sample separation (60 nm), the magnetic moment in this element can be switched to the reversed direction. This can be proved by imaging the magnetic state with increased tip-sample separation (120 nm), and the MFM imaging is shown in image (c). If the tip is then located at position (a) with a small tip-sample separation, the magnetic moment state can be switched back, as shown in the image (a). Such reversal is very reproducible. Fig. 3.9 shows that one can achieve control of the final particle magnetization state by adjusting the tip-sample separation from 60 nm to 120 nm at specific locations. Similar control of the final particle magnetic state was achievable in particles up to a maximum size of 1

[1]The contrast variation from white to gray or from dark to black comes from size variation of the dots, as can be shown in Fig. 3.8(a), since the stray field and stray field gradient is proportionally to the volume of the particle size.

[2]The appearance of local hexagonal symmetry of the magnetic moment state is the result of the minimization of the total sample stray field energy.

μm in length. The particle forms a low moment state when the tip is located in the center of the particle (Fig 3.9(b)), which we attribute to the fact that the in-plane tip field component is omnidirectional. Since the size of the element is still larger than the single domain critical size, a low magnetic moment flux closure state (vortex state) can be formed.

We envision that by carefully controlling the three dimensional tip position, the magnetic state of a particle can be controlled. At a small tip-particle separation, the tip can change the particle moment (write information), while at a large tip-sample separation the tip can be used to read the information from the particle.

3.3.4 Minimizing MFM Tip Stray Field Induced Distortions

It is challenging to image the undistorted magnetic structure of soft, small particles by MFM. This is due to unavoidable substantial perpendicular and in-plane tip stray fields (see Fig 3.2). To minimize tip stray field induced magnetic distortion, we found that the experiment needs to be performed in the constant height mode with a low moment tip, as close approaches to the sample are thus avoided. In the constant height mode, the tip-sample separation is controllable. Using a large tip-sample separation, one can greatly limit and control the tip stray field induced distortion. The reduced magnetic signal due to using small magnetic moment tip can be compensated by reducing the cantilever noise through operating the MFM in vacuum and ultimately at low temperature [34, 49]. As an example, Fig. 3.10 shows an MFM image obtained in the constant height mode of an array of particles with dimensions of 600 nm $\times$ 150 nm. With this low moment tip no visible distortion could be detected even at a tip sample separation as close as 30 nm. Compared to the image of Fig 3.2 (a), the total contrast of this image is weak, but what has improved is the spatial resolution, allowing fine magnetic details of the elements to be observed even though the particle width is only 150 nm.[1]

[1]Spatial resolution can be improved further if a sharp and high aspect ratio tip is used, such as tips prepared by electron beam deposited needles [68].

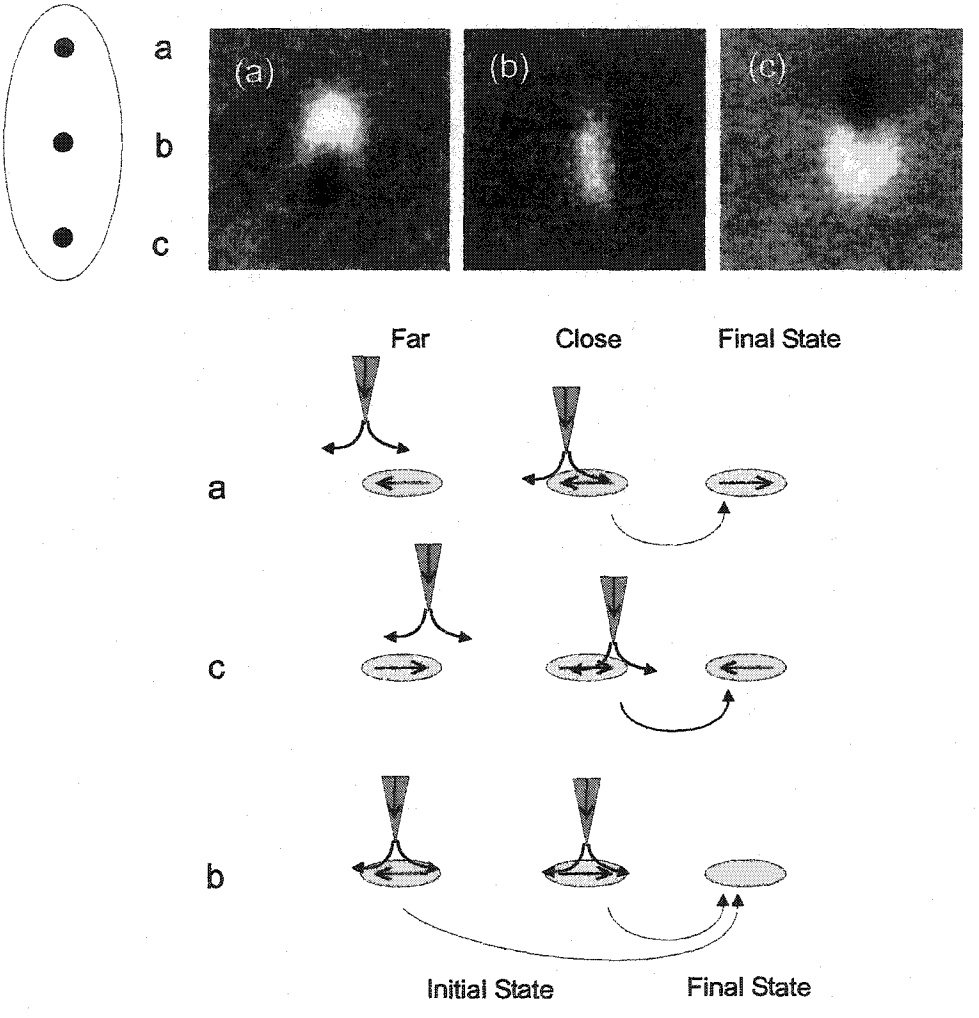

Figure 3.9: Controlling of an individual particle magnetic state by accurate three dimensional tip positioning. Schematic diagram shows how a MFM tip stray field controls a particle's moment state. Constant height mode in vacuum, particle 600nm × 150nm × 30nm, Tip: 50nm $Co_{71}Pt_{12}Cr_{17}$.

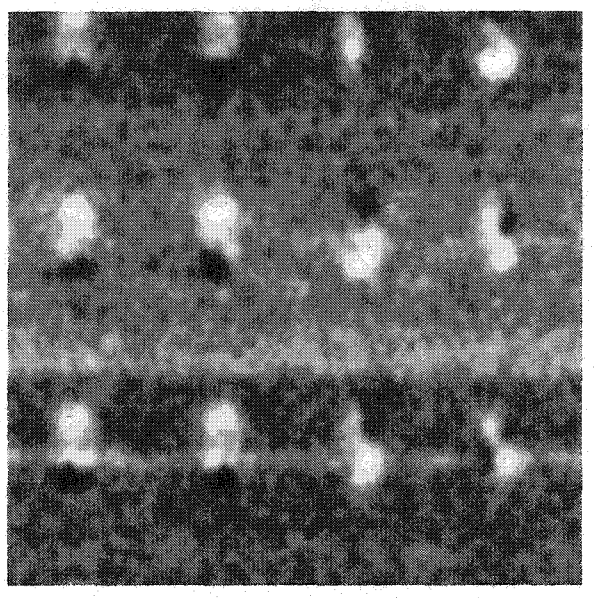

Figure 3.10: MFM images of particle array in size of 600nm× 150nm particle with the thickness of 30 nm. These particles are similar in size as those images in Fig 3.2 (a). Tip: 15 nm $Co_{71}Pt_{12}Cr_{17}$, tip sample separation: 30nm; in vacuum.

There are several other advantages of operating in the constant height mode. It is easy to detect tip stray field induced magnetization reversal in the constant height mode, as it shows up as a discontinuity in the scan line. This is in contrast to the tapping/lift operation mode, where in many cases only a change in the scan angle provides indications of irreversible tip-sample interaction effects [33]. A second benefit of constant height imaging is the potential increase in signal to noise (no extra noise contribution by the feedback control) and the increased possible scan speeds. Scan speed is a crucial aspect while studying the ensemble state at different external magnetic fields or studying switching histograms of one individual classical single domain magnet. Finally, the observed contrast in the constant height mode allows a straightforward comparison with simulation, since each image consists of the force gradient at a fixed tip-sample separation.

A major disadvantage of constant height mode is that it does not tolerate surface defects. Since the feedback controlling the tip-sample separation is turned off, there is the potential danger that the MFM tip physically touches the surface at defects,

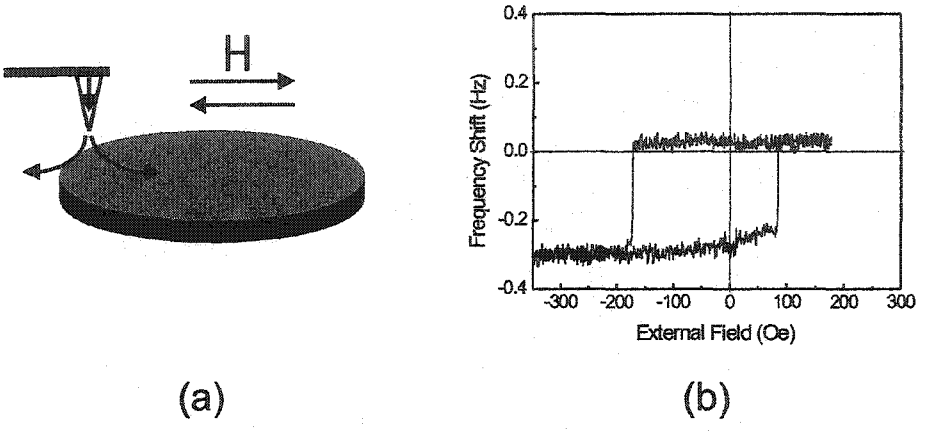

Figure 3.11: Local hysteresis measurement: (a) schematic diagram; (b) a typical plot of spectroscopy performed in a pseudo spin valve structure. Tip: 25 nm $Co_{71}Pt_{12}Cr_{17}$, in vacuum.

such as dust particles, with potentially calamitous effects for the tip. However, we found that this happened infrequently for carefully cleaned lithographically patterned arrays.

3.4 *Spectroscopy Measurements*

Force spectroscopy is performed by measuring the force (force gradient) as a function of tip-sample separation. This can be used to characterize the moment state of a nanomagnet (Fig. 2.13) and to investigate the local sample susceptibility (Fig. 2.15).

An alternative spectroscopy is to measure the local hysteresis loop of an individual nanomagnet. This can be obtained by measuring the force gradient as a function of external field at a fixed tip position. As shown in Fig. 3.11 (a), the MFM tip is located at a predetermined position above an individual element, while an external magnetic field is swept. The measured curve of frequency shift versus external field can be used to characterize the switching behavior of an individual elements, especially for signal domain particles. Fig. 3.11 (b) shows a typical hysteresis loop obtained for a NiFe(6nm)/Cu(3nm)/Co(4nm) pseudo spin valve structure with size of 550 nm $\times$ 70 nm. Two abrupt jumps of the cantilever frequency are associated with the soft layer

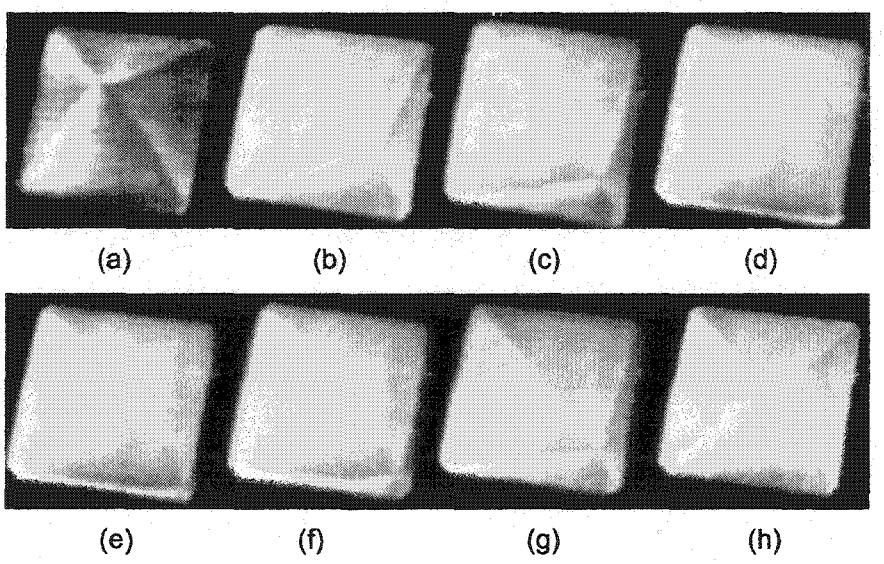

Figure 3.12: domain wall movement respect to an external field. The magnetic field was applied diagonally along the scanned area with the magnetic field of (a)-(h) -2 Oe, 5 Oe, 15 Oe, 45 Oe, 25 Oe, 20 Oe, 12 Oe, -2 Oe respectively. Tip: 50 nm $Co_{71}Pt_{12}Cr_{17}$, constant frequency shift mode.

switching. (The details of this sample will be discussed in the next chapter.)

3.5 Imaging in the Presence of External Fields

MFM imaging in the presence of an external magnetic field provides the opportunity to identify the sample magnetic structure, the nature of domains, and magnetization processes [30].

3.5.1 Magnetization Reversal of Multidomain Elements

Patterned soft magnetic elements of micron size can form flux closure domain patterns (Fig. 1.4 (b) and Fig. 2.11). The magnetization process therefore takes place via domain wall displacement and domain wall nucleation, as can be revealed through MFM images as a function of the external field.

Fig 3.12 shows an example of domain wall displacement via an external field for a 20μm sized NiFe element. In this element, a four-domain flux closure structure is formed. As expected, the domain with the the same moment direction as the external

field will grow, while the domain with opposite moment direction will shrink. The domain wall moves reversibly, as the magnetic field is smaller than the saturation field.

3.5.2 *Magnetization Reversal of Submicron Elements*

By performing MFM with an external magnetic field [30, 31, 58], the nanoparticle magnetization switching behavior and the switching field can be characterized and quantified. One needs to be aware of the fact that for submicron magnets, the combined effects of the MFM tip stray field and the external magnetic field can make the particle switch at a lower (or higher) field during imaging. This is demonstrated in Fig. 3.13. Fig. 3.13 (a) indicates that all the particles form single domain states with the same moment orientation after saturation, while Fig. 3.13 (b) shows the MFM images acquired with a magnetic field of 60 Oe along the particle long axis. Some particles were directly switched to the reversed state by the external field, marked by the solid circle in the image, however, several others were switched during the imaging process, resulting in the same contrast (dark) at both ends, marked by the dashed circle. Similar phenomena have been observed by some other research groups [30,60,61,78]. In this case the particle switching field is the combined effect of the external field and tip stray field. Since the tip stray field is omnidirectional and inhomogeneous, the real switching field of the particle cannot be easily obtained. The assumption that the tip stray field gives a constant offset to the particle's switching field can not hold true in the case of submicron sized particles, as the tip stray field is non-uniform over these dimensions (Fig 3.4). Furthermore, the tip stray field can change in the presence of an external field.

To minimize these effects and to obtain accurate switching fields for submicron or nanoscaled particles, the experiments need to be performed at remanence after the field is ramped to a certain value.[1] In this case, reversible magnetization behavior

[1]There is an exception. If switching happens before the magnetic field is reduced to zero, a magnetic field only reduced to a finite non-zero value should be used, as will be discussed later in Chapter 5.

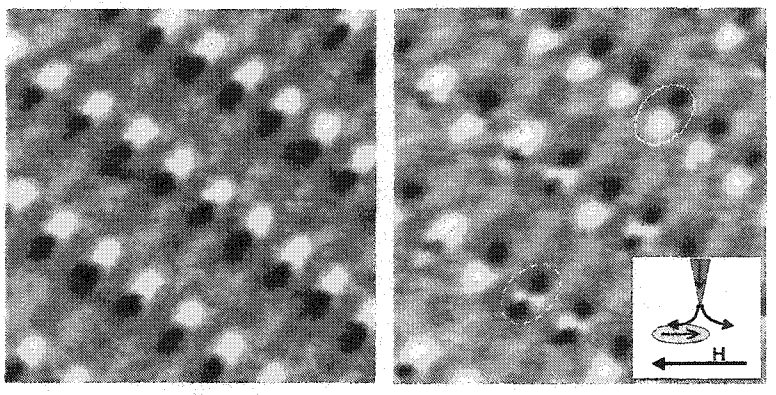

Figure 3.13: MFM images of particle array in size of 1.2μm×200nm. (a) images in remanence after saturation;(b) in the presence of external field of 60 Oe along long axis. Tip: 50nm $Co_{71}Pt_{12}Cr_{17}$; tip sample separation: 80nm; in vacuum. Inset: schematic diagram of experiment. Two circled elements show two different cases: one (solid) switched directly, the other one (dashed) switched during imaging process.

of the elements can not be observed, but the irreversible magnetization behavior, such as switching, can be clearly observed. This method is especially suitable for studying particles which form single domain binary states. By studying arrays of submicron magnetic particles, the remanent 'magnetization curve' of the ensemble as well as individual particles can be obtained. The particle switching field value and its distribution can be obtained very precisely if care is taken to ensure that the tip's stray field itself does not irreversibly reverse the particle's moment. The achievable accuracy is determined by the minimal field ramping step, typically 1 Oe in our study. By using a small moment tip, operating at constant height, and measuring at remanence, we found that the switching fields even lower than 50 Oe can still be determined reproducibly. As an example, Fig. 3.14(a-d) shows a series of MFM images at remanence after applying magnetic fields to predetermined values; no tip stray field effects found. Fig. 3.14(e) shows the percentage of reversed particles as a function of external magnetic field for an array with particle aspect ratio of 7:1.[1]

[1]The moment is assumed to be ±1 while plotting the normalized moment as a function of external field.

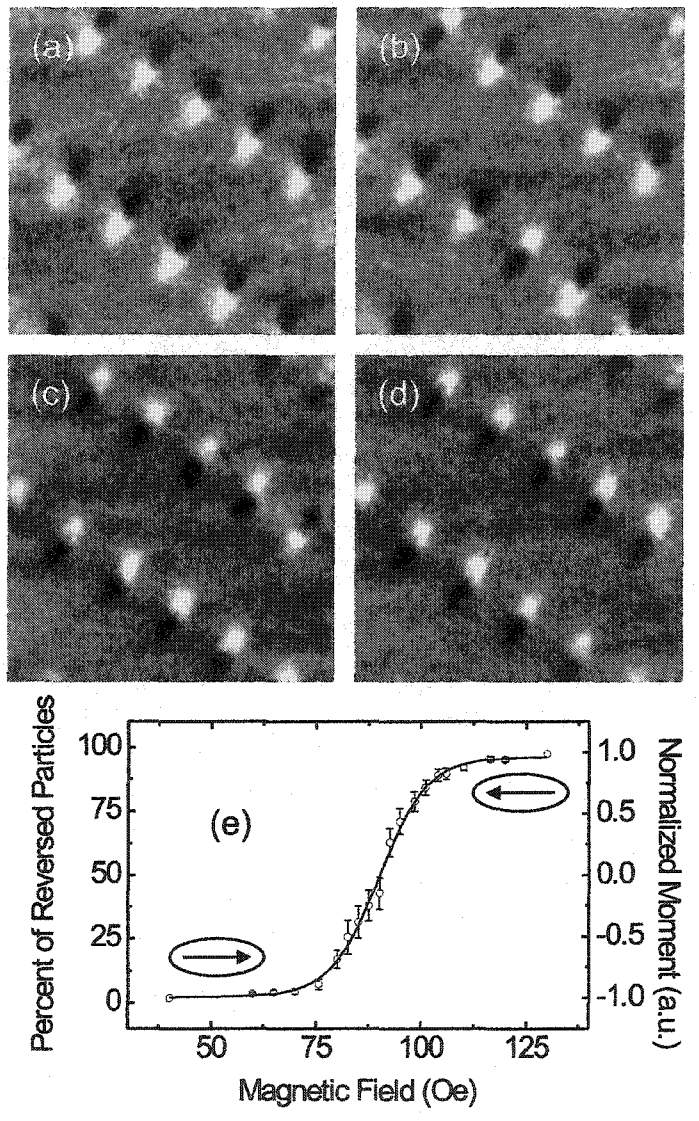

Figure 3.14: Reversal as a function of external magnetic field. Imaged in the remanent state after the field was ramped along the particle long axis. (a) -200 Oe; (b) 75 Oe; (c) 90 Oe; (d) 101 Oe. Particle size: 1.2μm×200nm. (e) Percentage of reversal as function of field. Tip: 50 nm CoPtCr, lift height 120nm; Gray scale is 1 Hz.

The results are averaged over 600 individual particles through 10 different images at different location. Each image contains about 60 individual particles, and the error bar is the statistical deviation of the 10 different images.

3.6 Magnetization Reversal of Elongated Elements

In the following, the magnetization switching of elongated magnets will be presented. One Permalloy array has elements of size 240nm ×90nm×10 nm, prepared by interference lithography techniques by Hao and Ross (MIT), and the others are 200 nm wide and 30 thick Permalloy arrays prepared by electron-beam lithography technique with length to width aspect ratio of 1:1 to 7:1, prepared by Metlushko and Ilic (the University of Illinois at Chicago and Cornell University).

3.6.1 Wide and thick elements

Recent studies show that the material, size and shape of the particles have a strong influence on the particle magnetic state and switching behavior [14, 69–78]. For elongated magnetic elements, shape anisotropy can affect the magnetic state. For example, Fig. 3.15 shows two MFM images of cobalt arrays from the literature [79]: one with the aspect ratio of 3:1, the other one with 1.5:1. For the small aspect ratio elements only a small percentage of the magnetic elements form a single domain state, while others are in low moment states with flux closure. For the aspect ratio of 3:1, bipolar contrast single domain states are observed.

Such bipolar contrast images are not due to uniformly magnetized single domain state, as magnetic moments close to the edge can be curved to reduce the total stray field energy, forming end domains [73, 80]. The magnetization reversal process of such single domain element is therefore not coherent rotation, in which, all the moment inside the elements rotate coherently like a giant spin with respect to an external magnetic field. Instead, the magnetization reversal occurs through the process of domain wall nucleation and propagation [73, 80]. Shi et al. demonstrated that magnetic

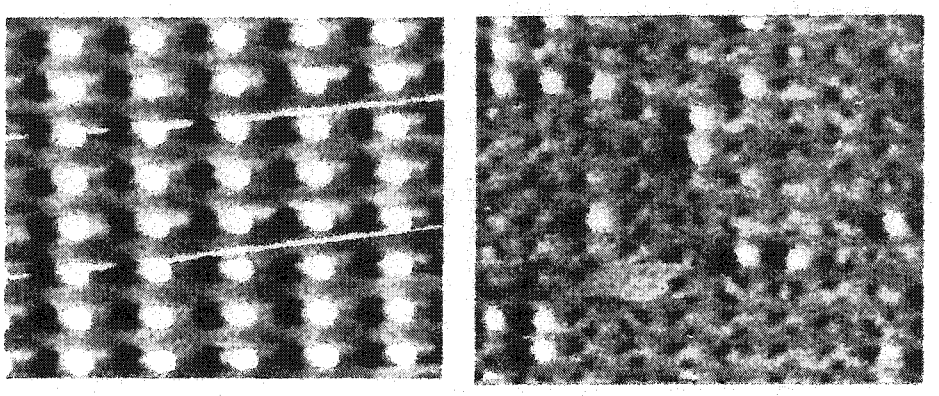

Figure 3.15: (a) MFM image of cobalt elements with a size of 600nm × 200 nm × 15 nm, all the elements form single domain states (b) elements with a size of 300 nm × 200 nm × 15 nm; a small percentage of the elements form single domain states, while others form low moment vortex states. After Girgis et al. [79].

vortices can be trapped during the process of magnetization reversal [62]. Through comparison of the remanent hysteresis loop and the major hysteresis loops obtained by AGM or SQUID Magnetometery [62, 73], they found that there exists a reversible low moment plateau in the remanent loop due to the formation of a vortex. In the following, we will demonstrate that such a low moment vortex state can even be formed in medium aspect ratio elements during magnetization reversal process.

Our MFM images indicate that magnetic elements with a small aspect ratio (< 2:1) can not form a single domain state, by showing low magnetic contrast at remanence. This is due to the increased demagnetization field along the long axis as the aspect ratio decreases. However, for aspect ratios larger than 3:1, the remanence after saturation indicates 100% single domain states by showing bipolar contrast in MFM images. Through MFM investigations, we found that for elements with aspect ratios larger than 4:1, the switching takes place via a sudden moment reversal from one single moment state to the reversed single domain state, as was shown in Fig. 3.14. Fig. 3.14 (e) shows the percentage of reversed particle as a function of external magnetic field for the aspect ratio of 7:1. Most elements are switched from the single domain

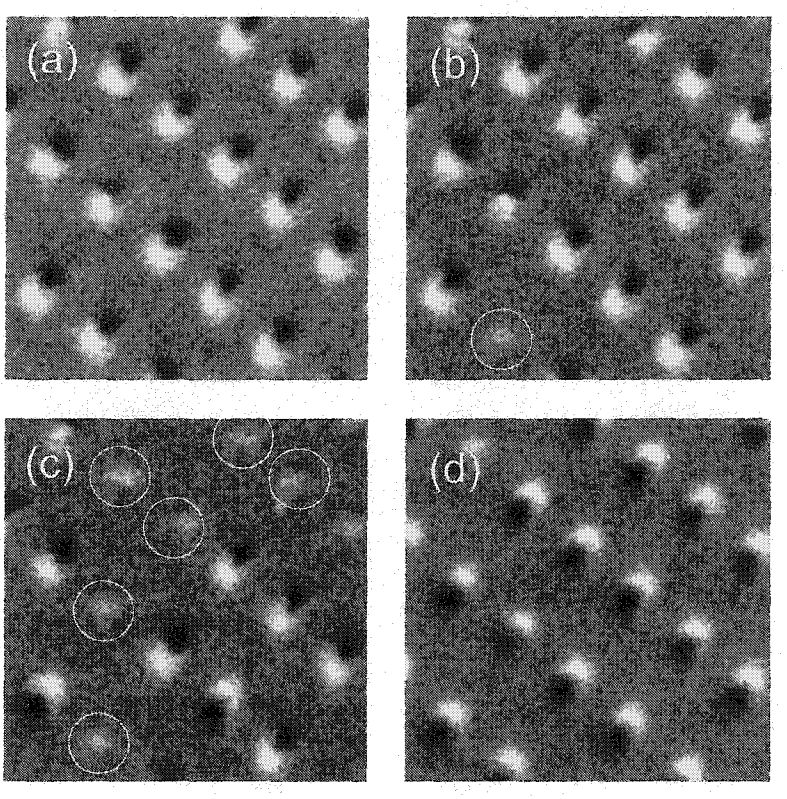

Figure 3.16: Reversal as a function of external magnetic field after saturation at -250 Oe, (a) 50 Oe, (b) 70 Oe, (c) 90 Oe, (d) 180 Oe. Particle size: 800nm×200nm; Circled: low moment states; gray scale 1 Hz.

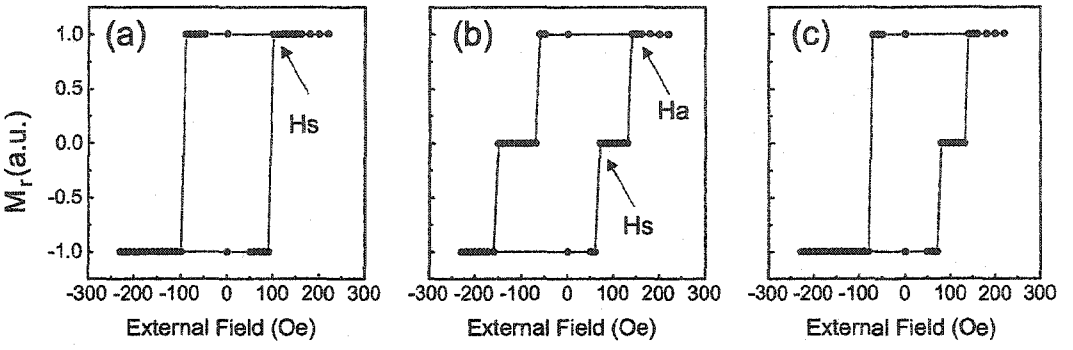

Figure 3.17: Remanent 'hysteresis loops' of three selected particles.

state directly to the reversed single domain state, however, we observe a small percentage (2%) of particles which form low magnetic moment states at remanence as opposite field is applied before forming reversed single domain state. This percentage increases as the particle aspect ratio decreases. Fig. 3.16 shows the remanent states after applying a reversing field of element with the aspect ratio of 4:1. As can be seen, there are several elements forming low moment states, which are are circled for clarity.

To further clarify the magnetization behavior and elucidate the nature of the low moment state, Fig. 3.17 shows the remanent 'magnetization curves' of three different element of aspect ratio of 4:1.[1] A very small percentage of the particles appear to reverse directly (Fig. 3.17(a)), similar to the typical behavior of particles with large aspect ratios. However, most particles behave like Fig. 3.17(b). A broad flat region of about 50-100 Oe width characteristic of a low moment state is found. This observation is similar to measurements by AGM of the remanent magnetization curve of low aspect ratio Permalloy arrays by Shi et al. [62].

This observation can be interpreted through micromagnetic simulation. Micromagnetic simulations suggest that both the single domain state and the vortex state could be formed in the elliptical particle with medium in-plane aspect ratio. Fig. 3.17

[1]The moment is assumed to be ± 1 for single domain state, and 0 for low magnetic contrast state.

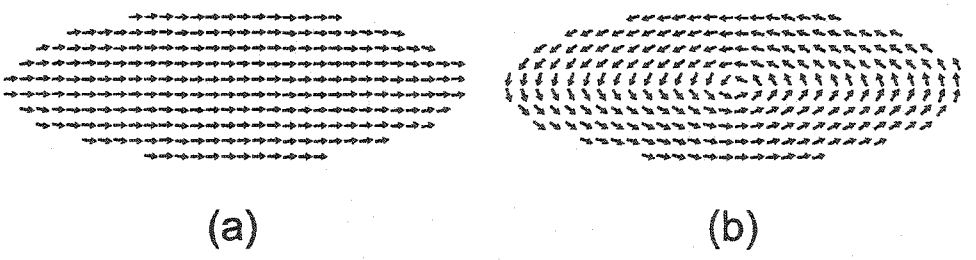

Figure 3.18: Two different states in an elliptical particle. (a) single domain; (b) one vortex. Particle size 600 nm × 200 nm ×30 nm; unit size: $10^3 nm^3$.

shows an example of an elliptical particle with dimension 600 nm×200 nm×30 nm.[1] We found that the total energy of the two states is very close, with the vortex state being only 5% higher than the single domain state. For the single domain state, the exchange energy is lower, but it has a higher demagnetization energy. Simulations from other groups also show that the single vortex or even multivortex states can be formed in elliptical permalloy particles [81]. During the switching process, if the trapped vortex is only a small percentage in the particle, the magnetic moments in the particle can be switched directly switching to the reversed single domain state, as indicted in Fig. 3.17(a). However, if the vortex become a global energy minima, a much larger field H_a, is needed to expel the vortex out from the element in order to form a reversed single domain state. A field smaller than H_a can only make the vortex move reversibly, and leads to the same state at remanence, as shown in the flat low moment region in Fig. 3. 17 (b). However, the switching behavior is not reproducible, which can be demonstrated in Fig. 3. 17 (c). For this individual particle, the moment can be switched directly from the single domain state to the reversed single domain state, or switched via the formation of a vortex state.

Even though the elements in an array were designed to have the same sizes and shape, the lithographic process can lead to element size variation and edge roughness, and eventually lead to switching field variations. As shown in Fig 3.19 (a), the

[1]The simulations were performed using three dimensional micromagnetic code from NIST. The unit size for the simulation is 10 nm.

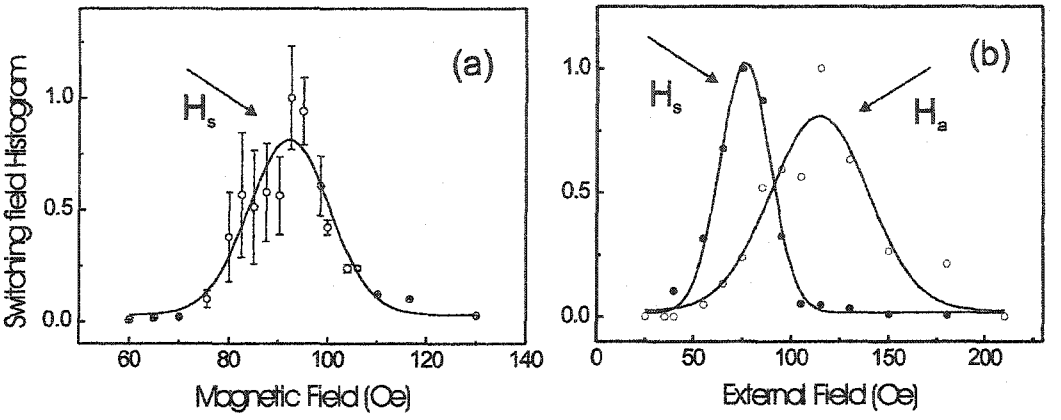

Figure 3.19: The switching field distribution of the array with aspect ratio of 7:1 and 4:1 with a particle width of 200 nm and a thickness of 30nm.

switching field of the elements have a broad distribution. The peak shows that the average switching field of the ensemble of particles is about 90 Oe. However, there are a few percent switched at fields below 70 Oe and a few percent above 110 Oe. By fitting the curve with a gaussian distribution, we found that the full width of the peak is about 32 Oe, 36% of the average switching field. The broad switching field variation is probably attributable to the edge roughness, as Kong et al. demonstrated that element with different edge roughness can leads to significant switching field variation [82]. Recently, micromagnetic simulation results also indicate that the edge roughness can substantially decrease the switching field. [14, 83].

For medium aspect ratio particles (4:1), switching occurs through vortex formation and vortex expelling. We used two fields to characterize the switching behavior: H_s, at which the particle switches directly from the single domain to a low moment state, and H_a at which a reversed single domain is formed. Fig. 3.19 (b) plots the switching field distribution of these two fields. As we can see, two peaks appear, with $< H_s >$ much smaller than $< H_a >$. The variation in δH_s is comparable to that of the large aspect ratio particles, while δH_a is much broader. The much wider switching field

distribution is attributed to vortex trapping.

3.6.2 *Narrow and Thin Permalloy Element Array*

As presented in last section, a vortex state can be formed in thick and wide elements. As the elements become narrower and thinner, the flux closure or vortex state is not favorable due to the cost of the exchange energy, and the single domain state is the most energetically stable state. Elements with the size of 240 nm × 90 nm × 10 nm have previously been demonstrated to be single domain states, as shown in Fig 1.4 (c) and Fig 3.2(b).

The collective switching behavior can be characterized by imaging the remanent state after applying magnetic fields to a predetermined value, as shown in Fig. 3.20. After a large field (±550 Oe) is applied along the long axis, the magnetic moments of all elements are aligned in the same direction as shown in Fig 3.20(a) and (b). As a reversed field is applied, some elements start to reverse to the opposite direction. However the individual element switching fields are not uniform as some elements switch at smaller fields of 150 Oe, while some others switch at fields as large as 350 Oe.

The remanent 'hysteresis loop' can be characterized by counting the percentage of switched elements as a function of external magnetic field, as shown in Fig. 3.21 (a). The observed remanent 'hysteresis loop' can be directly compared to the hysteresis loop obtained by alternating gradient magnetometery, shown in Fig. 3.21 (b). The coercivity obtained by either methods is very close to each other, which demonstrates the capability of using the MFM to characterize the switching behavior of nanomagnets.

AGM measurement shows that the remanent magnetization $(\frac{M_r}{M_s})$ is less than 1. This is because the remanent state is not uniformly magnetized due to the moment curving effects, as suggested by micromagnetic simulation. Edge shape can change the magnetic moment distribution close to the edge, as shown in Fig. 3.22. Elliptical

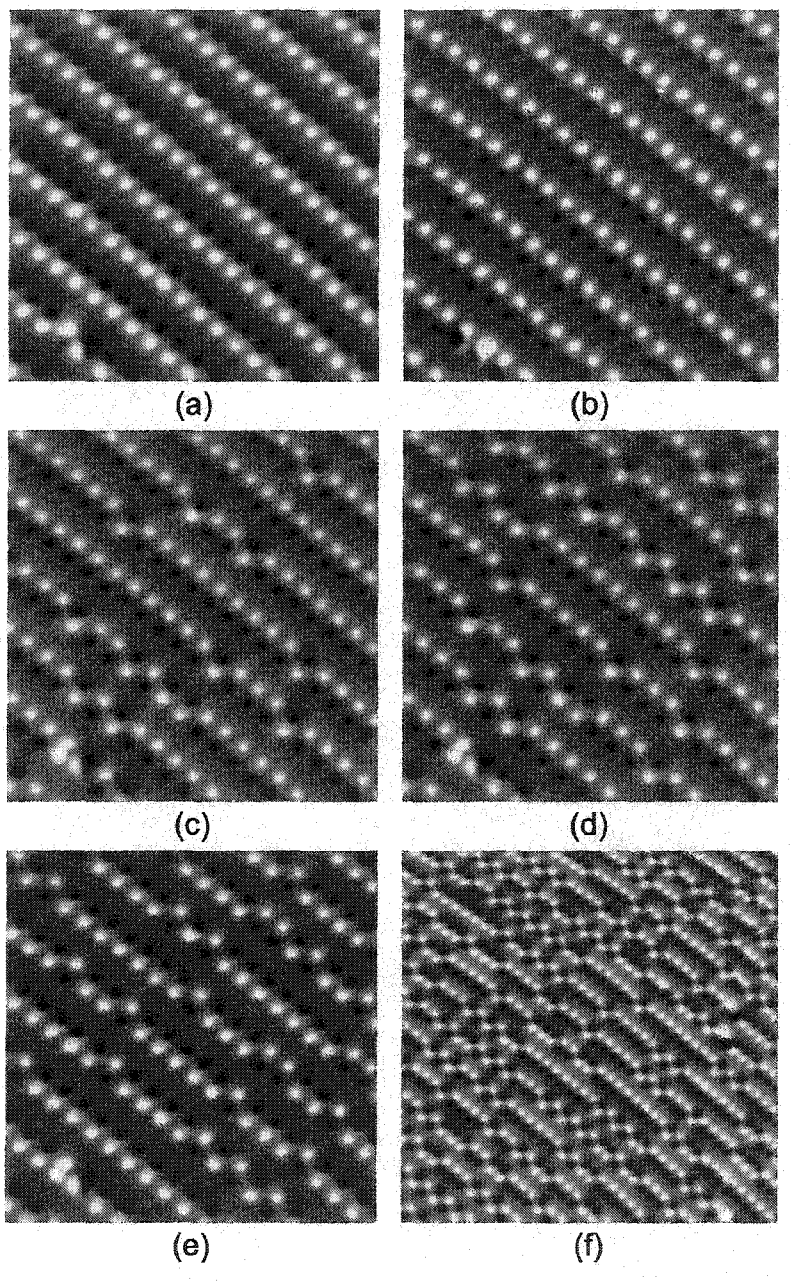

Figure 3.20: The MFM images at remanence after applying different magnetic field: (a) 550 Oe, (b) -550 Oe, (c) 250 Oe, (d) 280 Oe, (e) 330 Oe, (f) -290 Oe after applying 550 Oe (not in demagnetized state). Tip: 30 nm coated $Co_{71}Pt_{12}Cr_{17}$.

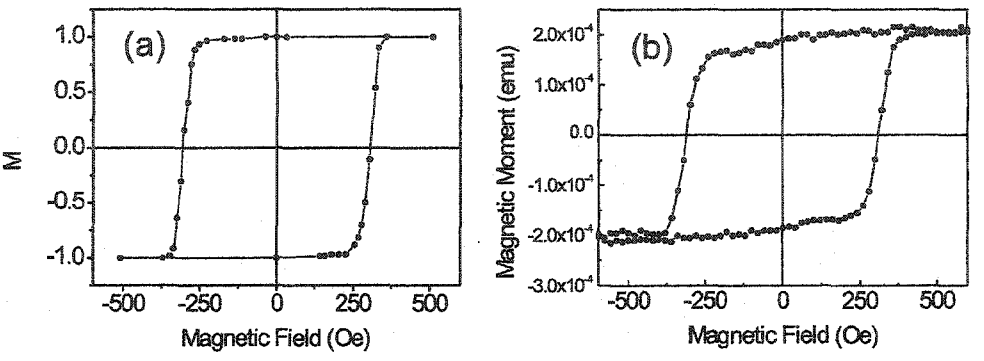

Figure 3.21: (a) remanent 'hysteresis loop' of 120 elements obtained by MFM; (b) hysteresis loop obtained by alternating gradient magnetometer of 10^9 elements.

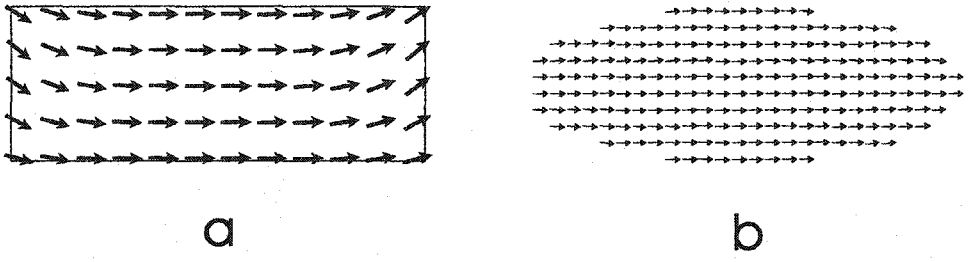

Figure 3.22: The magnetic state of a rectangular (a) and elliptical (b) element with the size of $90nm \times 240nm \times 10nm$. The unit cell is chosen to be 5 nm × 5 nm × 5 nm.

elements have higher remanence, while the magnetic moments close to the edge of rectangular elements is more curved. For real elements, the edge shape variation and edge roughness leads to a magnetic moment distribution variation, which also can dramatically change the switching field of the elements.

3.7 Summary

- Separation of magnetic contrast from topography submicron magnets can be achieved in the constant height mode, and in the tapping/lift mode. However, the constant height mode is desirable as the MFM tip produces less distortion of the sample magnetic state.

- By using various magnetic tips, operating in different modes, and studying different samples, the effect of magnetic tip stray field distortions on a magnetic moment state of a submicron sized magnet is investigated. Through the systematic study, a method of how to detect and to avoid the irreversible distortion is also presented. The possibility of using MFM tip stray fields to control a particle moment state is also proposed.

- A local hysteresis loop is developed by monitoring the cantilever resonance frequency shift versus an external magnetic field. The switching field of nanomagnets and remanent 'hysteresis loop' can be obtained by imaging with an *in-situ* magnetic field.

- Magnetic switching of the ensembles of individual elements can be characterized statistically through analyzing different individual elements, and remanent 'hysteresis loops' obtained by MFM. In narrow and thin magnetic elements, the single domain state is the most energetically state. For wider (200 nm) and thicker (30 nm) elements, even though the magnetic element can hold a single domain state at remanence, an energetically stable vortex state can be formed. The formation of a vortex leads to non-reproducible switching and broadening of the switching distribution.

4

Magnetization Switching of 70 nm Wide Pseudo Spin Valve

The results presented in this chapter are the magnetic domain structure and magnetization reversal of patterned 70 nm wide pseudo-spin valve (PSV) elements. Both the magnetically soft layer and the hard layer form single-domain states at remanence, and can be magnetized either parallel or antiparallel to each other. The switching field of each layer, and the coupling between the layers, are quantified using MFM. Individual elements show well-defined switching fields, while the ensemble has a large switching field distribution due to variability between the PSV elements.

4.1 Introduction

Lithographically patterned magnetic multilayer elements, such as magnetic tunnelling junction (MTJ) [2] and pseudo-spin-valve (PSV) elements [3,84], are key components in high density magnetoresistive random access memory (MRAM) devices [85]. Recent studies have focused on examining the behavior of elements with submicron or deep-submicron dimensions [82,86]. These PSV or MTJ elements consist of asymmetric sandwiches containing two magnetic layers with different switching fields: one is magnetically soft and the other is magnetically hard. For elements with micron-scale dimensions, interactions between the layers can lead to their demagnetization [87], and complex domain structures such as unfavorable 360° domain walls can be formed [88]. In comparison, the magnetic layers in elongated elements of sub-100 nm dimensions can show single domain behavior. The switching process is abrupt and the layers will

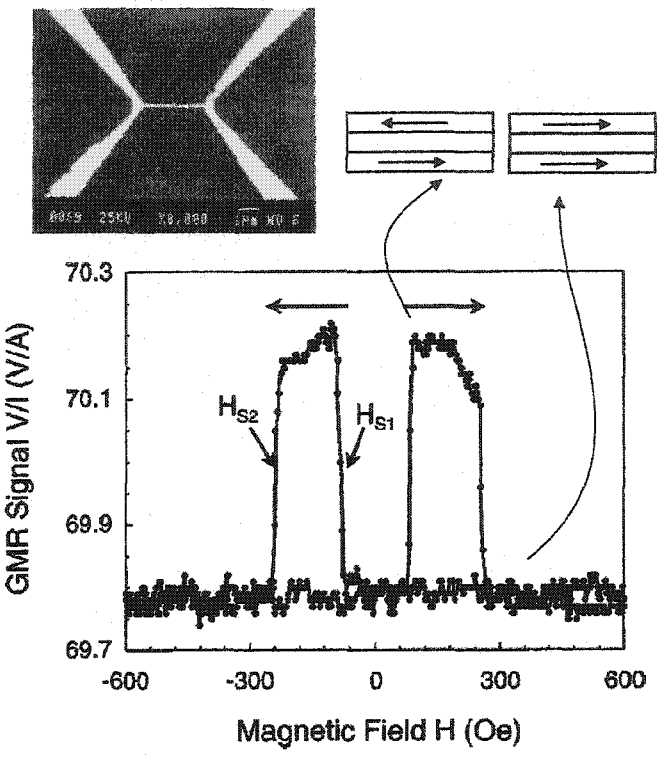

Figure 4.1: GMR curve of a pseudo spin valve structure with element size 300 nm wide and 3 μm long. Top: SEM image of a pseudo spin valve bar 100 nm wide and 3 μm long with four electronic leads fabricated by ion milling. Schematic diagram shows the relative moment state. Parallel: low resist; Antiparallel: high resist. After Kong et al. [82]

not be demagnetized by each others' fringe fields. Magnetoresistive (MR) behavior has been characterized for individual elements in both the current-in-plane(CIP) [82] and current-perpendicular-to-plane (CPP) configurations [86, 89], as shown in Fig 4.1 and Fig 4.2 respectively. The elements can be reversed by applying a magnetic field, or by polarized current-induced switching [86, 89]. Sudden jumps in resistance corresponding to the switching of the magnetic layers have been clearly demonstrated.

However, to date there has not been a study of the reversal of such small elements using magnetic force microscopy (MFM), or an investigation of their remanent states. In this work, we use high sensitivity, high resolution MFM with *in-situ* applied magnetic fields to characterize the magnetic domain structures in such arrays and the switching behavior of single elements.

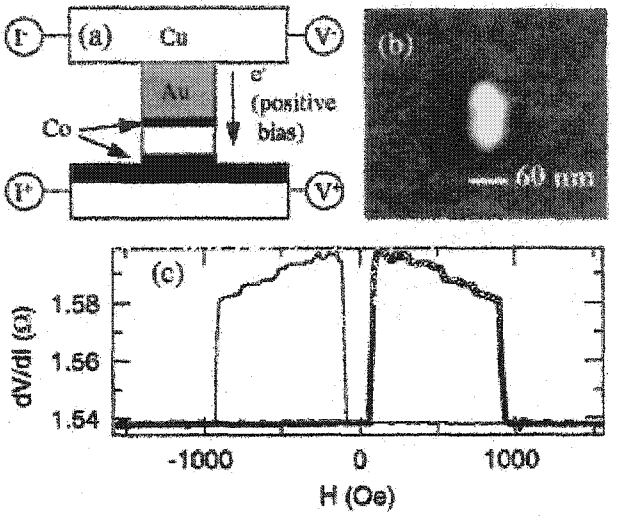

Figure 4.2: (a) A schematic cross section of the nanopillar device. (b) A SEM image of the Co nanomagets. (c) the differential resistance dV/dI as a function of magnetic field H applied parallel to the long axis of the magnet. After Albert et al. [86]

4.2 Experimental Techniques

The sample used in this study is an array of NiFe/Cu/Co/Cu PSV elements prepared using interference lithography and ion milling [90,91]. The individual elements have dimensions 70 nm×550 nm, with NiFe, Cu spacer and Co thicknesses of 6 nm, 3 nm and 4 nm respectively. The topographical image was previously shown in Fig. 1.1 (b). The magnetization behaviors were studied by the alternating gradient magnetometery (AGM) [90] and MFM, and the magnetic structures were studied by MFM. The magnetic probes used were silicon cantilevers sputter-coated with 25 nm of a $Co_{71}Pt_{12}Cr_{17}$ alloy. Two types of cantilevers were used: one with a resonance frequency of 68 kHz and spring constant of 1.5 N/m, and the second with corresponding parameters of 60 kHz and 0.9 N/m. To minimize the MFM tip-induced magnetic distortion, all MFM images were taken in constant height mode by allowing the MFM tip to fly above the sample plane at a user-controlled height, without tracking the sample topography [33]. The experiments were performed under moderate vacuum (1.0×10^{-5} Torr) and using a digital phase-locked loop to detect the cantilever fre-

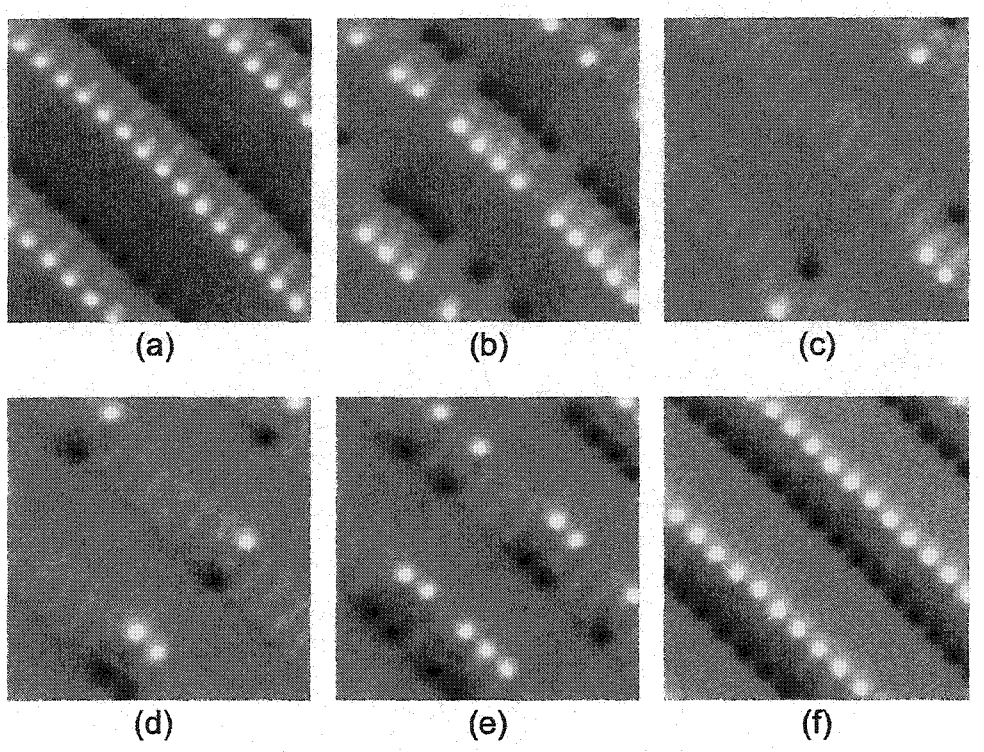

Figure 4.3: MFM images taken at remanence: (a) after saturation at 800 Oe; (b) after subsequently applying -65 Oe; (c) after subsequently applying -130 Oe; (d) -405 Oe; (e) -485 (f) -660 Oe. The gray scale corresponds to ≈ 1.7Hz $\approx 5 \times 10^{-5}$N/m force gradient.

quency shift [51], the minimum detectable force gradient in during this experiment was found to be 1×10^{-6} N/m with a cantilever oscillation amplitude of 15 nm. The images were taken at remanence to reduce the combined perturbing effects of the MFM tip and external field. The magnetic fields were applied in plane along the long axis of the elements, which is the easy axis due to shape anisotropy.

4.3 Imaging at Remanence

Fig. 4.3 (a)-(f) shows sequential images of the PSV structures after applying different fields. The remanent state, after saturation at 800 Oe (Fig. 4.3(a)), shows bright and dark contrast close to the element ends. This is a result of both magnetic layers having the same magnetization direction (the parallel or P state). However, if a magnetic field is then applied in the opposite direction, the magnetic moment in the

soft (NiFe) layer can be switched to be antiparallel to the moment in the Co layer. This is described as an AP state. The observed magnetic contrast is very weak because the stray fields of the NiFe and Co layers almost exactly cancel each other. As the opposite field is increased, more of the low moment AP states are formed, as shown in Fig. 4.3 (b,c). Above a critical field, all elements are in the AP state. If the magnetic field is increased further, the magnetic moment in the hard (Co) layer is reversed and a P state is formed that is oriented opposite to the original P state, as shown in Fig 4.3 (d-f).

4.4 *'Hysteresis Loop': Collective and Individual*

By performing large-area scans with an external field, the remanent MFM 'hysteresis loop' can be obtained,[1] as shown in Fig 4.4. The solid dots show the combined remanent hysteresis loop of 460 $\pm$10 elements. The broad switching field distribution is a result of different individual elements having different switching fields. The moment in the soft NiFe layer reverses at a small field, labelled H_{c1}, which averages approximately 80 Oe, though some elements reverse at 25 Oe and others at 125 Oe. The switching field range is thus at least 100 Oe. An even wider variation (400 Oe) is found for the hard layer switching field H_{c2}. H_{c2} averages 480 Oe, though reversal occurs at fields between 300 Oe and 700 Oe.

However, for an individual element, we find square hysteresis loops with abrupt switching at well-defined field values of H_{c1} and H_{c2}. The magnetization reversal of individual elements may be studied by imaging the element at different fields, but it is more convenient to measure a local hysteresis loop without scanning [26], as shown in the inset of Fig. 4.5(a). The cantilever frequency shift is proportional to the force gradient between the tip and the sample. The observed frequency shift is thus a measure of local sample moment. Fig. 4.5 (a) shows the hysteresis loop of a

[1]We assign +1 or -1 to elements in the P state, and 0 to elements in the AP state, since the magnetization of the two layers in the AP state almost cancel each other.

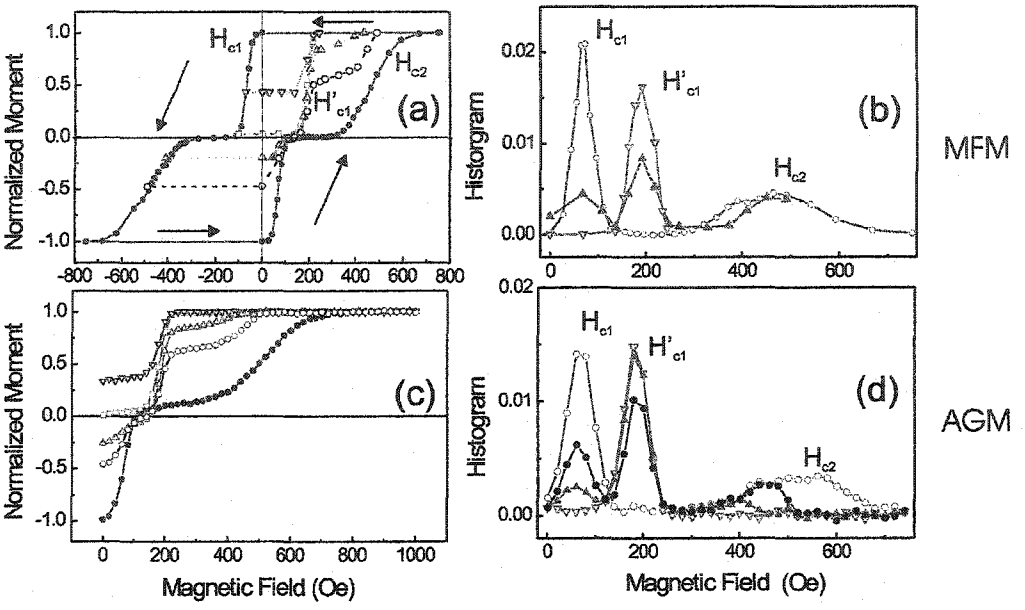

Figure 4.4: (a) Major (solid dots) and minor remanent hysteresis loops obtained by MFM; open dots: minor loop with a starting field of -488 Oe; up triangle: -410 Oe; square: -102 Oe; down triangle: -70 Oe. The major loop is based on measuring 460 elements, the minor loops on 170 elements; (b) differential curve of (a) for the major loop (open dots) and the minor loops with starting fields of -102 Oe (down triangle) and -488 Oe (up triangle); (c) Major and minor remanent loops of 10^9 elements measured using AGM; only field values larger than 0 Oe are presented. (d) differential curve of the AGM remanent major and minor hysteresis loops; circular open dot: major loop; solid dot: minor loop with a starting field of -488 Oe; solid up triangle -410 Oe; open down triangle dot -102 Oe. Dots are connected for clarity.

selected dot.[1] Two distinct frequency changes are clearly visible at applied fields H_{c1} and H_{c2}, which correspond to the soft layer (H_{c1}) and the hard layer (H_{c2}) switching. The abrupt frequency changes, and the images in Fig. 4.3, suggest that both the soft layer and the hard layer switch between two oppositely-oriented single-domain states. However, we cannot conclude that the switching process is classical coherent rotation, as end domain structures may be trapped at the edges of the elements.

[1]The monotonic change in the cantilever frequency at large applied magnetic fields is caused by the stray field gradient of the in-plane electromagnets. This can be demonstrated by performing similar measurements without a sample close to the tip.

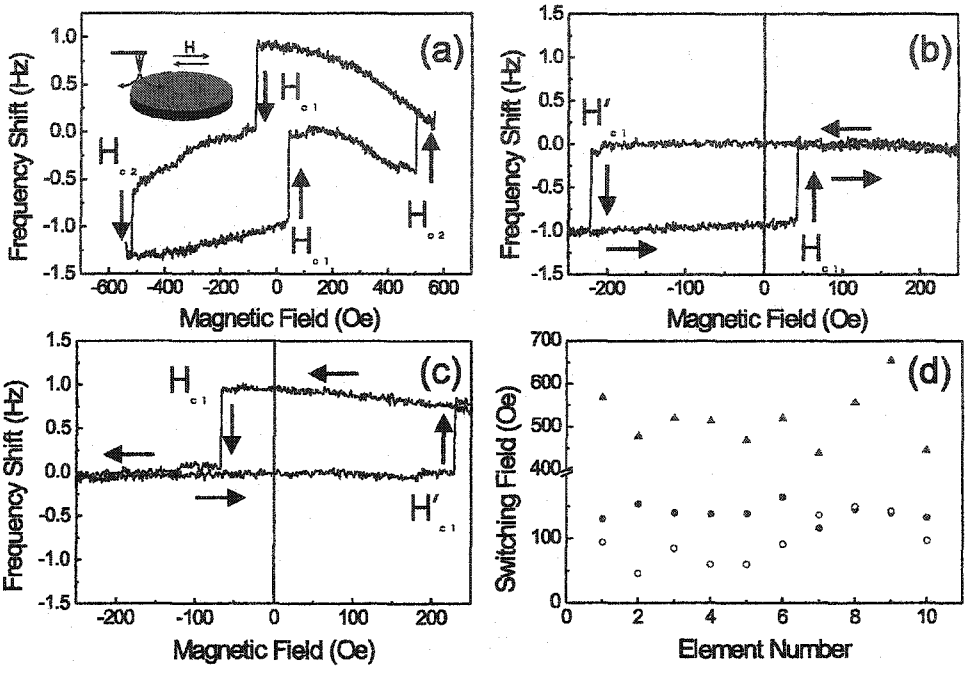

Figure 4.5: Hysteresis loop of a single element. 1Hz $\approx 3 \times 10^{-5}$ N/m. (a) major loop; (b) minor loop starting from the P state, (c) minor loop starting from the opposite P state. The MFM tip was located at one end of the element as shown in the inset of (a). The large difference between H_{c1} and H'_{c1} is caused by the interaction with the hard layer. (d) switching field distribution of H_s (solid circular dots), H_{c2} (solid up triangles) and offset field H_{off} (open circular dots) for ten different individual elements.

4.5 *Layer Coupling*

Minor loops of a single element were measured by sweeping the external field between $\pm H$ where $H_{c1} < H < H_{c2}$. In this case, only the soft layer is switched and the element cycles between the P and the AP states. Typical examples are shown in Fig. 4.5(b) and (c). A large field of 800 Oe (-800 Oe) was first applied to saturate both layers to form a P state, and then an opposite field was ramped to $-H$ (H) to form the AP state. However, if the field is then ramped backward to H ($-H$) as indicated by the arrows in Fig. 4.5(b) (Fig. 4.5(c)), the soft magnetic layer is switched back to form the P state at a field H'_{c1} ($-H'_{c1}$), which is larger than H_{c1}, but much smaller than H_{c2}. The asymmetric switching of the minor loop is due to the magnetic coupling

between the two magnetic layers, as a result of magnetostatic interactions and of exchange coupling through the 3 nm Cu layer spacer. It is worth pointing out that Fig. 4.5(b) and 4.5(c) are realistic hysteresis loops of a PSV element when it is used in an MRAM cell. The novel observation is that the loop is nearly a perfect square in shape with sharp magnetization transitions.

We can express the magnetic coupling between the two layers as an offset field H_{off} which the hard layer exerts on the soft layer. The switching field for an isolated soft layer, in the absence of the hard layer, will be $H_s = \frac{H_{c1}+H'_{c1}}{2}$, while $H_{off} = \frac{H'_{c1}-H_{c1}}{2}$.[1] We found that for any particular element the switching field and the offset field are very reproducible, with variation less than 10 Oe between measurements. However, the switching field and offset field show considerable variation from element to element. Fig 4.5(d) shows a plot of H_s, H_{off} and H_{c2} for ten different elements. The offset field has substantially larger variability than the soft layer switching field.

Minor loops of the array were studied by acquiring MFM images after applying different fields. Fig 4.4 (a) shows several remanent minor loops at a starting field of -70 Oe (open down triangles), -102 Oe (open squares), -410 Oe (open up triangles) and -488 Oe (open dots) for 170 $\pm$ 5 elements. It is convenient to describe the four possible magnetization states that can coexist in the array as A, B, C and D, as shown in Fig.4.6, where A and B are the two possible P states and C and D are the two AP states. Upon positive saturation, all elements are in the B state. In the minor loops corresponding to small reverse fields (-70 Oe and -102 Oe), most elements remain in the initial B state and only a small percentage of the elements are switched from the B state to the D state by the reverse field. As the field is ramped back towards positive saturation, the soft layer in the D state is switched back to recreate the B state at a field H'_{c1}. However, when compared to Fig. 4.5(b), the minor loop is not a perfect square shape, since the abrupt transition of the individual elements is washed out by the switching field variation between the elements in the array. At

[1]The free layer switching field is $H'_{c1} - H_{off}$ or $H_{c1} + H_{off}$.

larger reverse fields (-410 Oe, -488 Oe), the sample consists of a mixture of A and D states. We observe that three different switching process appear as the field is ramped back to positive saturation. The elements in the A state are first switched to the C state at a field H_{c1} and then to the B state at a field H_{c2}. Elements in the D state are switched directly to the B state at a field H'_{c1}. This switching behavior can be clearly seen by constructing differential curves of Fig. 4.4(a). Fig. 4.4(b) shows the differential curves for the major loop (open dots) and minor loops at a starting field of -102 Oe (open down triangles) and -488 Oe (up triangles). For the major loop, there are two distinct peaks at fields H_{c1} and H_{c2}, representing soft layer and hard layer switching. For the minor loop at -102 Oe, only one peak at the field H'_{c1} is observed, which is associated with the switching from the D to the B state (see also Fig. 4.4 (b) or (c)). However, at a field of -488 Oe, 41% of the elements are switched to the A state, while the others are in the D state, and the differentiated minor loop shows three distinct peaks at fields H_{c1}, H'_{c1} and H_{c2}. Fig. 4.4 (c) and (d) shows the corresponding data acquired by AGM on a sample with 10^9 elements. There is an excellent agreement between the AGM and MFM data.

So far, by assuming that both the Co and NiFe layers are single-domain elements which can adopt P or AP configurations, we can successfully explain our experimental observations. In the following, we will show that highly sensitive MFM can be used to visualize distinctly the AP states as well as the P states. A field of -800 Oe was first applied to form the A state. Fig. 4.6 (a) shows the MFM image of the sample after applying 480 Oe reverse field. Some elements were switched to the B state, while the others formed the C state. If the field is then switched back to a value in between H_{c1} and H'_{c1}, for instance 135 Oe, the C states remain, while the elements in B states are changed to D states. Fig. 4.6(b) clearly shows the C and D antiparallel states coexisting. The gray scale contrast in this image is only about 0.09 Hz, which is about 10% of the value obtained for the parallel state image. The result is in good agreement with the relative magnetizations of the parallel and

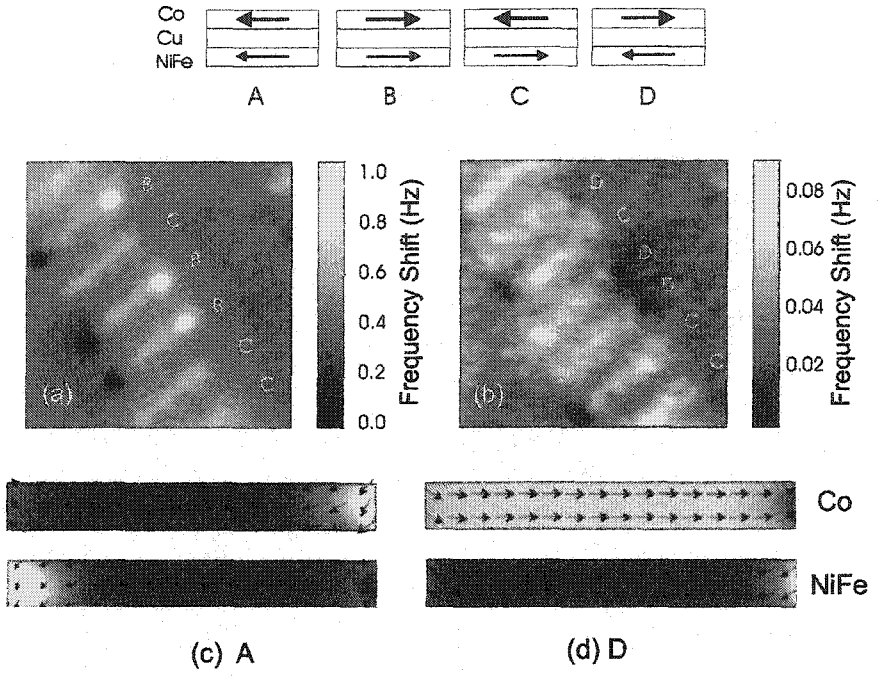

Figure 4.6: Top: diagram of the four possible magnetic states in the PSV elements. (a) mixtures of antiparallel states and parallel states formed after applying 480 Oe reverse field to a previously saturated array; (b) coexistence of the two different antiparallel states, after subsequently applying a positive field of 135 Oe; (c) magnetic moment configuration in P state; (d) in AP states. 1Hz $\approx 4 \times 10^{-5}$N/m.

antiparallel states obtained by AGM. The signal is so small that some unavoidable topographic contrast also appears in the images. The low contrast occurs because the two magnetic layers form a closed flux loop with very small external stray field. Better contrast can be achieved by increasing the MFM tip moment, but this can perturb the magnetic states of the elements. The observed P or AP states are consistent with the remanent states of individual elements calculated using a micromagnetic simulation. The simulated magnetic moment orientations are shown in Fig 4.6 (c-d). The AP state is very stable and consists of two single-domain layers antiparallel to each other, while in the P state, the moments in each layer are parallel to each other but show curling of the magnetization at the edges due to the strong demagnetizing field.

It is critical to maintain a narrow switching field distribution if PSV elements are

to be used in MRAM. During cycling of the soft layer, the switching field distributions for $-H_{c1}$ and H'_{c1} should not overlap, and neither should the distributions of $-H_{c1}$ and $-H_{c2}$, to avoid inadvertent writing of elements during the readback process. MFM analysis has indicated that there are no overlaps in the array studied here, because the Co layers have relatively large switching fields compared to the NiFe layers. However, it is desirable to reduce the switching field distributions so that a lower hard-layer switching field, and therefore a lower write current, can be tolerated. The broad switching field distributions observed in this sample have two different sources: one contribution comes from intrinsic variability in the switching fields of the Co or NiFe layers, due to shape or microstructure differences between the elements, and the other contribution comes from the variation in interlayer coupling field, H_{off}. Perhaps surprisingly, we found that H_{off} has a larger variation than the soft layer switching field H_s, and the two do not appear to be correlated (Fig 4.5 (d)). The variability in H_{off} may be a result of roughness or pinholes in the 3 nm Cu spacer layer, which can affect exchange coupling between the magnetic layers, as well as the detailed microstructure or shape of the element ends, which could lead to local deviations in magnetostatic coupling between the layers.

4.6 Summary

The collective and individual magnetization reversal of 70-nm wide PSV elements has been studied using high sensitivity MFM with an *in-situ* magnetic field. Our results indicate that the two magnetic layers can form either parallel or antiparallel magnetic configurations. Individual elements show abrupt switching behavior, with ideal, square shaped hysteresis loops, but there is a spread in both the switching fields and in the interlayer coupling field between individual elements. This distribution may be a result of variability in shape or microstructure of the magnetic layers, or the roughness of the Cu spacer layer. Controlling the element shape and microstructure will help elucidate this problem.

5

Magnetization Reversal of Dense Disk Array

In this chapter, the magnetic structure and magnetization reversal of a permalloy disk array are presented. The interdot coupling and its induced anisotropy are investigated.

5.1 *Introduction*

In his pioneering work, Cowburn experimentally found that single domain nanomagnet can be formed in a disk as the element diameter (d) and thickness (t) are below a critical value [77]. Above that value, the circular dots are proposed to form vortex state, in which the magnetic moments are parallel to the nearest edge inside the circular disk.

The appearance of the single domain phase and the vortex phase is the result of

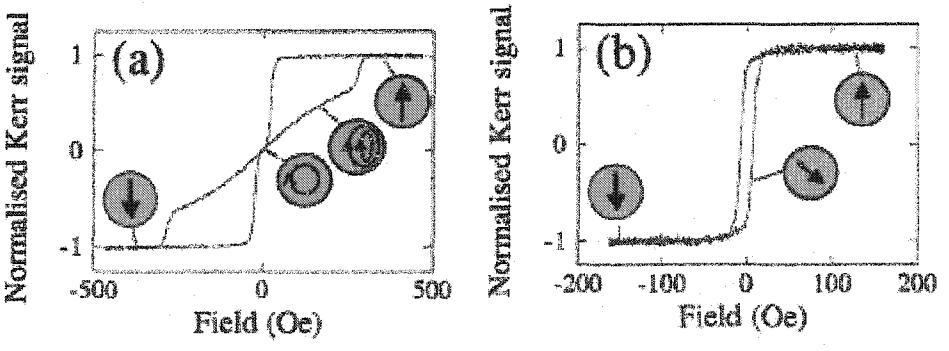

Figure 5.1: Hysteresis loop obtained by MOKE of nanomagnet array with diameter of 300 nm (a) and 100 nm (b) respectively. The thickness of the magnets is 10 nm. From Cowburn et al. [77].

the competition between the magnetic exchange energy and magnetiostatic energy (stray field energy). The typical magnetization reversal curves for both state are shown in Fig 5.1. For the single domain state, the magnetization reversal process can be characterized by coherent rotation (Fig 5.1 (b)), while for the vortex state, the magnetization reversal process is through vortex nucleation and vortex annihilation. The study of circular magnet dots which form vortex states has been of of great interest in the last few years [69]. The vortex state of circular elements have less stray field. Therefore, the disks can be fabricated very close to each other with little neighbor influence, a very attractive feature when fabricating ultrahigh density of magnetoresistive random access memory.

The central problem of studying a disk array is then how magnetization reversal occurs in the disk, and how the interdot coupling affects the switching behavior and switching field. Recently, the vortex structure, magnetization behavior and interdot coupling were studied by Lorentz Microscopy [92], MFM [93], MOKE Magnetometers [75,94], alternating gradient magnetometery(AGM) [95], and Brillouin light scattering (BLS) [96]. In this chapter, we will use MFM with *in-situ* magnetic fields to study the vortex structures and its magnetization reversal. A local hysteresis loop technique is developed to study the reversal mechanism. The interdot coupling induced anisotropy is directly measured through hysteresis curves obtained by MFM as well as imaging.

5.2 *Experiment Techniques*

Standard electron beam lithography and liftoff techniques were used to pattern circular permalloy dots with a diameter of 700nm and thickness of 25nm on a square rectangular lattice with a lattice constant of 800nm.[1]

The magnetic structures and magnetization reversal were studied by a custom built vacuum MFM. The experiments were performed in the constant height mode

[1]The samples were kindly provided by V. Metlushko of the University of Illinois at Chicago, and B. Ilic of Cornell University.

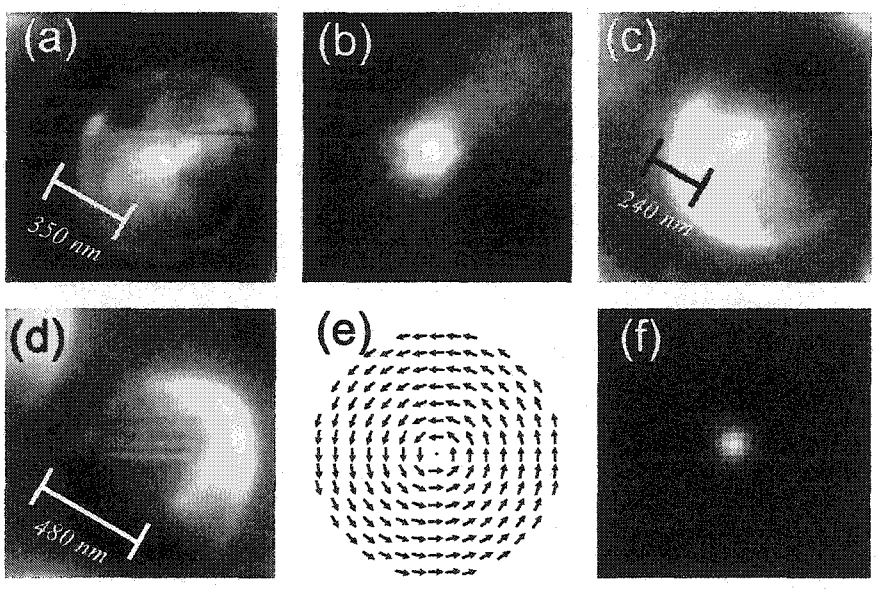

Figure 5.2: a. Vortex structure of permalloy disk; b. Zoom in of a vortex core with 140 nm scan size; c. image at a field of 23 Oe; d. image at a field of -55 Oe. e. simulated moment distribution of a permalloy disk with the same size as the experiment. f. gray scale shows the moments of out of plane component in a 140nm area of e. Tip: T_{30}

to reduce the destructive MFM tip-sample distortions [33]. Silicon cantilevers with spring constants of 1 N/m and 0.08 N/m, sputter coated with $Co_{71}Pt_{12}Cr_{17}$ with thickness of 15 nm (T_{15}), 30 nm (T_{30}) and 50 nm (T_{50}) were used as magnetic probes. The experiments were performed in a vacuum of 1×10^{-5} Torr. A digital phase locked loop (PLL) from NanoSurf to increase sensitivity was used to decode the cantilever frequency shift [51]. The typical tip-sample separations were about 50-80 nm, unless otherwise indicated.

5.3 Experimental Results

5.3.1 Vortex State

The ac demagnetized state of permalloy disks have small stray fields, which lead to very low magnetic contrast MFM images. High resolution images show that the disk forms a vortex state as shown in Fig 5.2 (a) and (b). The disk shows very weak contrast with a bright spot in the center. This is a flux core, a singularity of the vortex

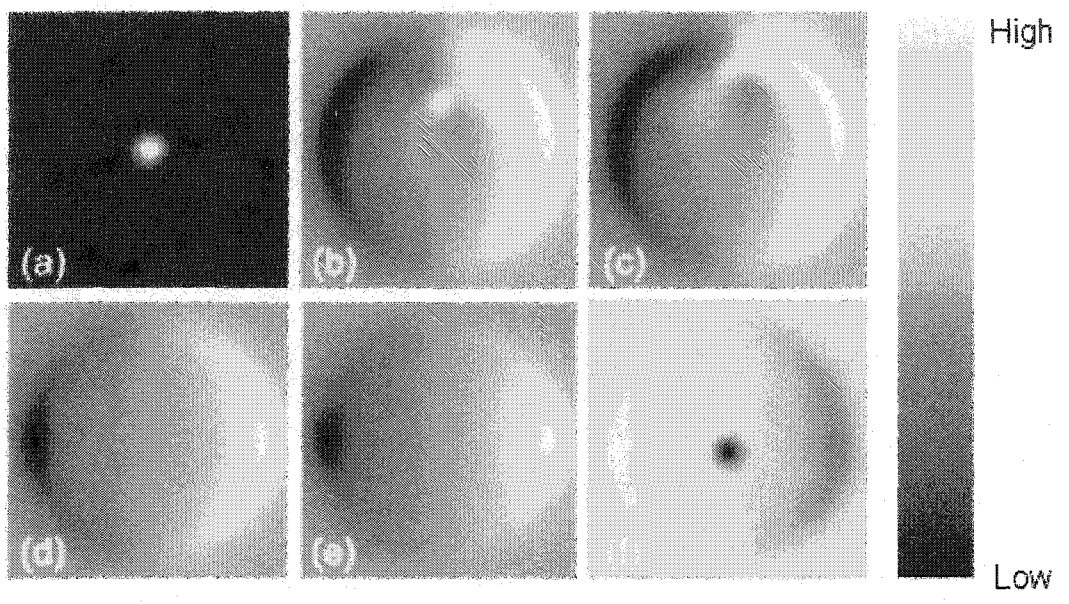

Figure 5.3: Calculate stray field at 40 nm above the disk surface at (a) H=0 Oe, (b) H=200 Oe, (c) H=400 Oe, (d) H=800 Oe, (e) H=0 Oe, and (f) H=-50 Oe. Disk diameter: 500 nm, thickness: 25 nm. Unit cell: 5 nm × 5 nm × 5 nm. A smaller disk than in the experiment is used due to the limit of the computer capacity. Color scale shows the relative stray field magnitude.

state in the permalloy dot, which has been directly observed only recently [92, 93]. This result is consistent with micromagnetic simulation,[1] and theoretical analysis [97]. The simulated results, as shown in Fig 5.2(e) and (f), indicate that the lowest energy state is a vortex state with most of the moments rotating along the disk radius. However, the center part (the vortex core), with a size of about 10 nm, points normal to the sample plane. Because of it small in size, the flux core is hardly observable at large tip-sample separation.

5.3.2 *Nucleation and Annihilation Process*

A distinct characteristic of magnetic disks, which has been confirmed by measuring the hysteresis loop of arrays of dots or through the study of individual disks [77,92–94],

[1]The simulation uses the three-dimensional CODE from NIST, http://math.nist.gov/oommf. The element has the same dimension as the experiment. We used a unit cell of 4nm×4nm×5nm, an exchange constant of 1.0×10^{-11}J/m (1.0×10^{-6}erg/cm), and the damping constant of 0.5. The magnetocrytalline anisotropy is neglected.

is that the magnetization reversal has two transitions: the nucleation and annihilation of the magnetic vortex, as shown in Fig 5.1(a).

By performing MFM images in the presence of an external magnetic field, the vortex core will move. Fig 5.2(c) and (d) are the images when an external field is applied diagonally along the image area. As expected, the flux core moves closer to the edge perpendicularly to the field direction, as marked in the images. As a larger field is applied, the vortex core will be pushed to the edge, and can be expelled. Micromagnetic simulations on a permalloy disk with the presence of an external magnetic field are performed to help understand the experimental results. The stray field emitted from the disk is calculated based on the disk magnetic moment configuration, obtained by micromagnetic simulations. Fig 5.3 shows the stray field distribution in a plane 40 nm above the element. At zero field, the element forms a perfect vortex with a vortex core in the center (Fig. 5.3 (a)). As a magnetic field is applied, the vortex core moves towards the edge perpendicularly to the field direction. For a field larger than a critical value (H_a), the vortex core can be expelled outside of the element, and a single domain state is formed. As the field is reduced, initially, the element still can keep its single domain state, however, when it reaches a critical value ($-H_n$), the vortex core is nucleated inside the element, as shown in Fig. 5.3 (f). Micromagnetic simulation also indicates that the vortex is initially nucleated at the edge, and gradually moves to the center area (Fig. 5.3 (f)). However, MFM has no time resolution to observe this.

5.3.3 *Individual 'Hysteresis Loop'*

Such individual nucleation and annihilation process can be demonstrated by the local hysteresis loop, developed in section 3.4. As shown in the inset of Fig. 5.4, the local hysteresis loop can be obtained by monitoring the cantilever frequency shift as a function of the external magnetic field. The cantilever frequency shift is then converted to the force gradient between magnetic probe and the disk, F′. This force

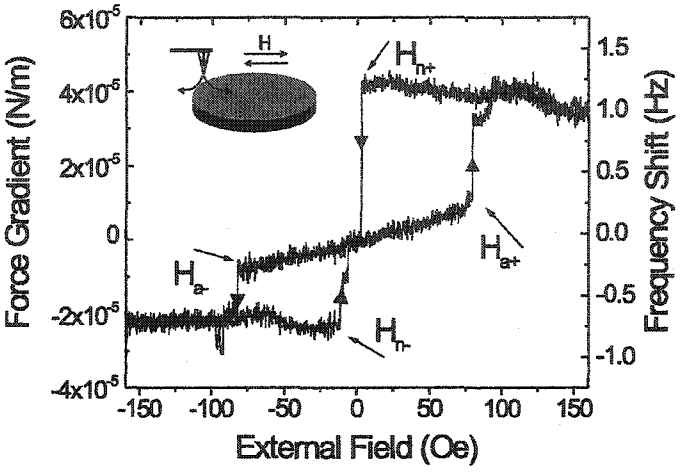

Figure 5.4: Force gradient between the MFM tip and sample as a function of external field, while the tip is located at a fixed position 30 nm above the disk, as shown in the inset. Cantilever: T_{15}, k=1 N/m.

gradient is approximately proportional to the sample moment. A typical plot is shown in Fig. 5.4. When examining each single curve from positive (negative) saturation to negative (positive) saturation, we found that two distinct jumps are clearly visible. One is associated with the nucleation process, while the other is associated with the annihilation of a vortex. As the field decreases from positive saturation (single domain state) the force gradient initially remains at a 'constant' value. When the field reaches the nucleation field H_n, the force gradient decreases abruptly (the formation of a vortex is confirmed by imaging). As the field decreases to negative value, the vortex core moves toward the edge of the disk, (Fig. 5.2(c), (d) or Fig. 5.3(b),(c)), and the force gradient decreases. When the field reaches a critical value H_a, the force gradient decreases abruptly again and reaches a static value (the vortex is expelled). When the field is increased from the negative saturation to positive saturation, similar phenomena can be observed.

Close examination of the hysteresis curve reveals that it is not symmetric. The absolute value of the force gradient is not symmetric, which is due to the z component of the MFM tip stray field locally reversibly rotating the moments of the dots. The switching fields, however, are not symmetric either. The difference comes from the

in-plane component of the tip stray field contributing to the magnetization reversal. Assume that the average in-plane component of tip stray field on the particle is H_{eff}, and the nucleation field without tip is H_n. We observe $H_n = \frac{H_{n+} + H_{n-}}{2} \approx 10$ Oe for the disk. The average contribution of the tip $H_{eff} = \frac{H_{n+} - H_{n-}}{2}$ is less than 10 Oe for T_{15} and 25 Oe for T_{30} with a tip-sample separation of about 30nm. Not only can the local hysteresis curve be used to characterize the magnetization behavior of small disks, but it is also possible to use this technique to characterize both in-plane and out of plane components of the tip stray field.

5.3.4 Imaging Versus Magnetic Fields

It is challenging to obtain the disk switching field from images [78], since the tip stray field can induce irreversible distortions. To obtain the switching field of dots, one can assume that the MFM tip contributes a constant field offset [78]. However, many effects such as the unknown tip in-plane and out of plane component, and the potential change of the tip stray field in the external field lead to major uncertainties. To obtain an accurate switching field, one needs to perform the MFM experiments at a field close to $H_p = (H_n + H_a)/2$ after the external field is ramped to a designated value H. The disk will maintain its previous state at H_p. Suppose that at H the disk is reversed to a single domain state. When the field is decreased to H_p, the nucleation of a vortex will not yet happen. Alternatively, suppose that at H the disk is reversed to a vortex state. When the field is increased to H_p, annihilation will not yet happen. The prerequisite to reliable and accurate determination of a switching field is that H_p combined with the tip stray field cannot induce switching. This can be actually solved by using low moment tips and operating in the constant height mode. Fig 5.5 shows a series of images, where the field was applied in the (100) or (110) directions, as shown in the inset Fig. 5.6. No tip stray field induced reversal can be observed. A weak contrast from the low moment state comes from the distorted vortex as the imaging is not taken at remanence.

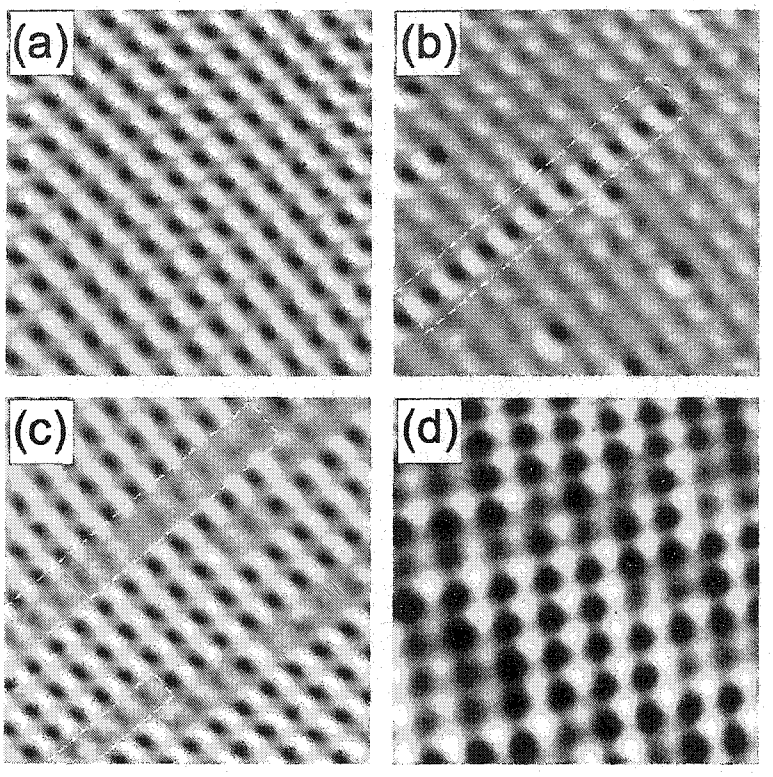

Figure 5.5: A series of images after applying different external fields. a. field ramped to 126 Oe, and imaging at 60 Oe; b. field ramped to 23 Oe, and image at 60 Oe; c. field ramped to -20 Oe after saturation at -200 Oe, and imaged at -60 Oe, d. field ramped to -40 Oe after saturation at -200 Oe, and imaged at -70 Oe. Tip: T_{50}. Switching is found correlated with appearance of chain switching, marked in the dashed squares.

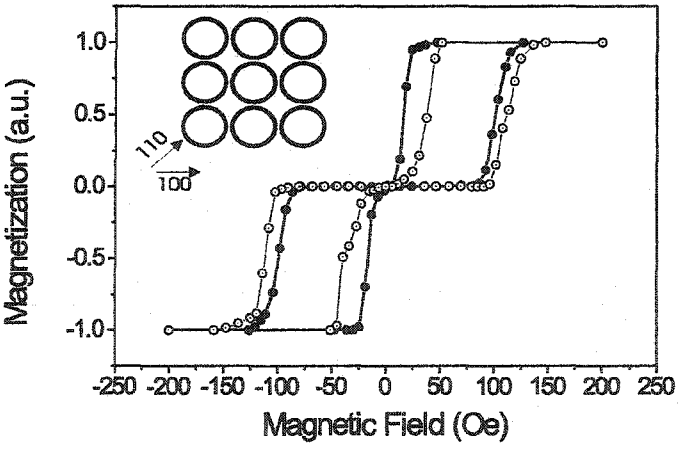

Figure 5.6: Hysteresis curves along 100 (solid dots) and 110 (open dots) direction. Tip: T_{50}.

Field directions	$< H_n >$	δH_n	$< H_a >$	δH_a
$< 100 >$	14	5	104	9
$< 110 >$	32	9.3	115.5	11.5

Table 5.1: Switching field and its distribution of permalloy disk array along the (100) and (111) direction. In oersted.

5.3.5 *Interdot Coupling Induced Anisotropy*

By following this procedure, we can obtain accurate switching fields of the disks without tip stray field artifacts. The 'hysteresis curve' (switching probability) can be obtained by characterizing ensembles of disks, as shown in Fig. 5.6.[1] A two step transition can clearly be seen.

Fig. 5.6 shows that both the nucleation and annihilation fields depend on the direction of the external field. Table 5.1 list the average switching field and its variation. We found that if the field is applied in the (100) direction of the array, a smaller annihilation and nucleation field is observed. The switching fields difference between (100) direction and (110) direction cannot be explained by dipole interaction for uniformly magnetized dots, which only yield a uniaxial anisotropy contribution.

Model calculation by Guslienko shows that the magnetostatic energy is anisotropic with a minima along the (100) or (010) direction with fourfold anisotropy [98]. The anisotropy comes from high order multipole coupling, quadrupolar interaction being dominant. For magnetic disks without external field, the stray field of each individual disk is very small, and the inter-dot dipolar and higher order multipole coupling is negligible. For annihilation of a vortex, as magnetic field is applied, the vortex state is deformed by shifting the vortex core out of center, and the magnetization in the disk is nonuniform. For nucleation of a vortex, as magnetic field decreases from saturation, nonuniform shape of magnetization configuration can be formed

[1]The magnetic moment is assumed to be ± 1 for single domain state, while it is 0 for vortex state. The results are averaged over 120 individual elements.

before nucleation of a vortex. Such non-uniformity will then lead to the observed anisotropy. The magnetostatic coupling expected to be weak for the (110) direction as directly confirmed by MFM images (Fig. 5.5c and 5.5d). For the (100) direction, the nucleation appears to be correlated with nucleated chains (Fig. 5.4c). However, in the (110) direction, the correlation is much weaker (Fig. 5.4d). This correlation is stronger in nucleating vortices than in annihilating vortices, and leads to smaller switching field variations in the (100) direction than that in the (110) direction.

5.4 *Summary*

E-beam patterned permalloy circular dots of 700 nm diameter with small separations were very carefully studied by magnetic force microscopy (MFM) in the presence of an *in-situ* magnetic field. Images in the demagnetized state show that the dot is in a vortex state with a vortex core (singularity) in the center. Local hysteresis loops, measured by cantilever frequency shift in an external field, indicate that the magnetization reversal of individual disks is a vortex nucleation and annihilation process. By carefully doing MFM, nucleation and annihilation fields without MFM tip stray field distortions are obtained. Interdot coupling induced anisotropy originated is found through hysteresis loops, and directly confirmed by MFM imaging, as the nucleated dots are correlated.

6

Magnetization Structure and Switching of Permalloy Ring

This chapter presents the study of the magnetic structure and magnetization reversal of Permalloy rings with diameters of 5 μm and 700 nm respectively. Two stable transitions from the 'onion' state to the flux state and from the flux state to the reversed 'onion' state were studied in detail as a function of external field. The reproducibility of switching and switching field distribution were studied.

6.1 Introduction

The interest of studying the magnetic ring structure was initiated by the possible design of ultrahigh density vertical magneotoresistive random access memory (VMRAM) based on ring structured GMR stacks [69]. The ring shaped memory element forces magnetization to be circular. The relative orientation of an moment direction in the magnetic hard layer and soft layer, clockwise or anticlockwise, can produce GMR effects. There are at least two advantages of using ring structures. The vortex state in the ring structure will minimize the stray field influence of neighbors, therefore, elements can be fabricated very close to each other, achieving ultrahigh density. The edge roughness in elongated elements leads to broad switching field distribution and poor reproducibility of switching. The ring structure however will have less edge roughness effects. The critical size above which the vortex state is stable is smaller for ring structure than the disk structures, therefore, higher density of MRAM can be achieved in ring structures. This is because the vortex core structure is avoided

in a ring, which can substantially reduce the exchange energy.

Recent studies show that cobalt ring structures have two kinds of magnetic states: a stable flux or vortex state, and a second stable or metastable 'single domain' like state [99, 100]. The latter is known as the 'onion state' due to the fact that each half of a ring has the same moment orientation, forming head to head and tail to tail domain walls where the opposite flux meets [99, 100]. There are many open questions concerning the magnetic properties of these ring systems. Why is the onion state or the vortex state stable? What is the nature of the head to head domain? How reproducible is the switching process? Magneto-optical Kerr effect (MOKE) measurements [99, 100] have been used to study the collective behavior of patterned rings, and magnetic force microscopy (MFM) measurements [100] have characterized the switching behavior of individual rings. However, if MFM is operated in the tapping/lift mode [100], the MFM tip stray field can strongly influence the ring magnetic structure and thus make interpretation difficult. In this chapter, we present an MFM study of the switching behavior and its reproducibility, as well as the nature of the head to head domain wall of permalloy rings.

6.2 *Experimental Techniques*

The sample studied in this chapter are two different NiFe size rings: one with outer/inner diameter of 5μm/4μm, the other one with 700 nm/ 350 nm. Both rings are 25 nm thick.[1] The topographic images are shown in Fig. 6.1.

Two types of commercial silicon cantilevers were used as force sensors with typical spring constants of 2 N/m and 0.05 N/m, resonance frequencies of 70 kHz and 15 kHz, and Q factors of 40,000 and 2,000 respectively, each sputter coated with 50nm $Co_{71}Pt_{12}Cr_{17}$. An oscillation amplitude of 10 nm was used. The experiments were performed in a vacuum of 1×10^{-5} Torr in the presence of an in-plane magnetic field.

[1]Both sample were prepared by e-beam lithography and lift-off techniques, and provided by V. Metlushko of the University of Illinois at Chicago.

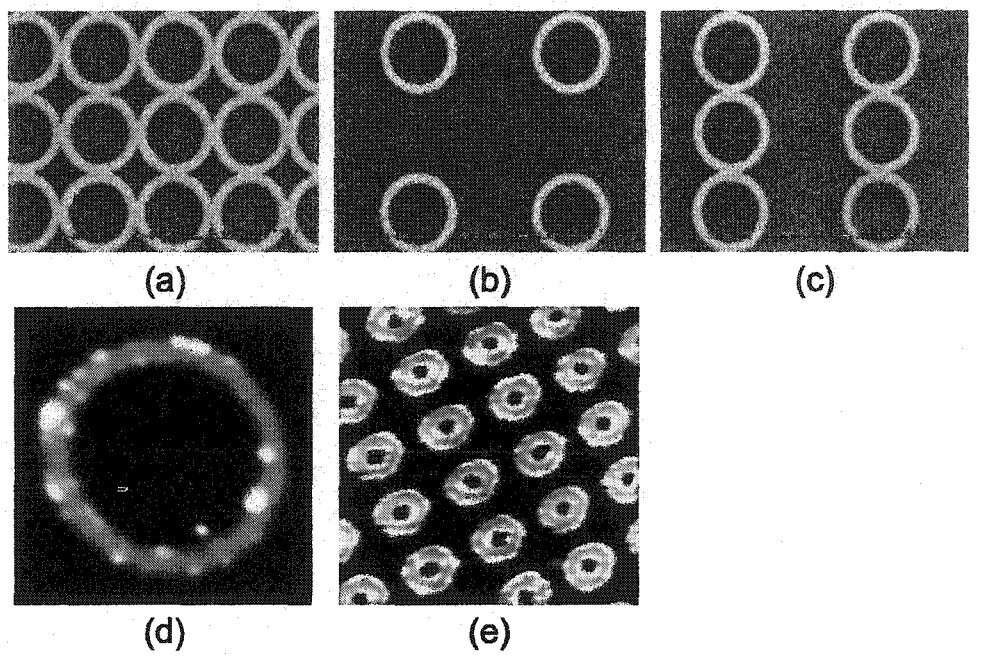

Figure 6.1: SEM and AFM images of Permalloy ring structures: (a) connected rings structures; (b) individual rings; (c) ring chains; (d) non-contact AFM image of individual ring; (e) contact AFM image of individual ring.(a-d) ring size of 5 μm, (e) ring size of 700 nm.

A digital phase locked loop (PLL) [51] was used to decode the cantilever frequency shift. The typical tip-sample separation used is 150-200 nm for studying the switching behavior, while reduced to 50-80 nm when imaging fine details.

6.3 *Imaging versus Magnetic Field*

Fig. 6.2(a-d) show a series of MFM images of an array of 5 μm individual rings as a function of magnetic field. The individual rings show two different magnetic states. One is a low contrast state (Fig. 6.2(c)), also called the vortex state [99], as schematically sketched in Fig. 6.2(c). The other shows bright and dark magnetic contrast at the edge along the field direction (Fig. 6.2(a,b,d)), called the 'onion' state, as sketched in Fig 6.2(a). The transition between these two states can clearly be seen by plotting a remanent 'hysteresis curve',[1] shown in Fig. 6.2(e-f). Fig 6.2(e) shows

[1]The hysteresis curve is a plot of the number of reversed rings versus the external magnetic field. To plot this curve, we assign the onion state the numerical value of +1, the reversed onion state a

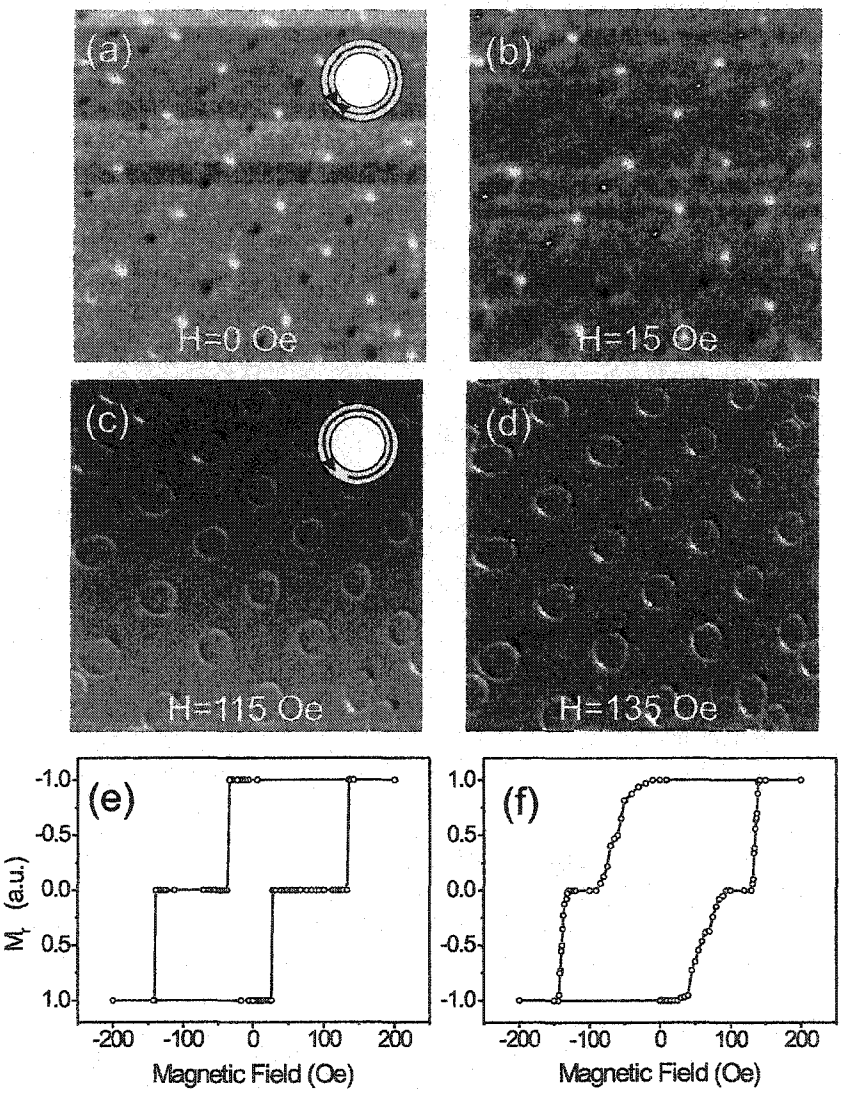

Figure 6.2: (a)-(d) MFM images of rings of 5μm as a function of external magnetic field; (a,b,d) onion state;(c) vortex state (e) hysteresis loop (determined from MFM data) of individual particle, showing two transitions, (f) hysteresis loop of ensemble of particles. The fields were applied diagonally along the images.

the 'hysteresis' loop of an individual particle. By analyzing an image with about 100 rings, we obtain the normalized, averaged sample magnetization as a function of the external field (Fig. 6.2f).

Both the images as well as the hysteresis curves demonstrate two different magnetic transitions. One appears at a low critical field Hn of about 50 Oe, the other at a relative high field Hs of about 140 Oe. At fields $Hn < H < Hs$, images show the rings have a low remanent magnetic moment characteristic of the so called vortex state. At fields $H > Hs$, the rings form a single domain like state, the onion state. In the following we will discuss details of the ring domain structure, and the reversal mechanism, as well as analyze the variations in the values of the critical fields Hn and Hs.

6.4 Magnetic Structure

The vortex state (circular magnetization) is the most stable state in magnetically soft ring structure, which is the result of minimizing magnetostatic energy at the expense of ferromagnetic exchange energy [69]. The magnetic moments in the flux state form a circular or vortex pattern, without a topological singularity associated with the center of a disk structure. Due to this, magnetostatic stray field energy is minimized and the MFM contrast is small (Fig. 6.2c). The magnetic vortex state is shown in Fig. 6.3(a) at tip-sample separation of 40 nm. The bright spots at the edge are defects, as can be shown in Fig 6.1 (d). The gray and dark contrast inside ring comes from nonuniform moment curvature, and regular dark and bright magnetic contrast can be observed in each individual ring at larger tip-sample separation. This contrast comes from nonuniform moment curvature as a result of edge roughness as well as defects. The associated interaction is very small, showing a force gradient contrast

value of -1, and the flux state a value of 0. The MFM images were taken in the remanent state after ramping the external field to a fixed value. This minimized the effect the tip field on the switching field.

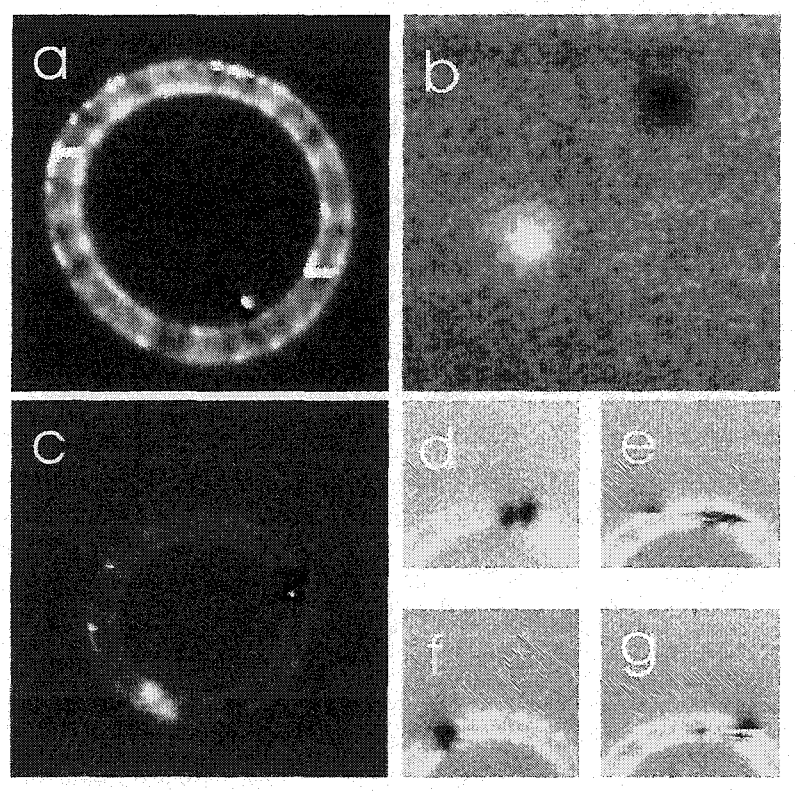

Figure 6.3: High resolution constant height MFM images of 5μm obtained with a 50 nm $Co_{71}Pt_{12}Cr_{17}$ tip. (a) flux state imaged at 40 nm. Onion state imaged at a separation of (b) 150 nm, (c) 80 nm, (d) 70 nm, (e) 50 nm, (f) 50 nm and (g) 50 nm.

of 3×10^{-6} N/m at a tip sample separation of 150 nm. Similar variations in contrast were previously observed at the edge of octagonal rings [100].

The remanent state after saturation however shows a strong single domain like black and white contrast, as shown in Fig 6.3(b). This is expected due to the fact that after saturation, the moments in the ring are mirror symmetric along the axis parallel to the external magnetic field direction. As the external field is reduced to zero, domain walls will be formed at the location where the two opposite half rings meet. The nature of this head to head domain wall can be revealed by a series of MFM images taken with a gradually reduced tip sample separation, as shown in Fig. 6.3(c-g). Reducing the tip-sample separation increases MFM resolution, but also leads to a stronger tip-sample interaction. Unexpectedly, at higher resolution, we found that each dark or bright spot observed at lower magnification is composed of two dark and two bright spots (Fig. 6.3c). When the tip-sample separation is reduced beyond a critical value, these spots (domain walls) are locally moved around from one pinning site to another as shown in Fig. 6.3(d-g).

To understand the head to head domain wall, we performed micromagnetic simulation, as shown in Fig. 6.4. The rings used for simulation have the same dimensions as the experiments, with unit cell sizes of $(12.5\text{nm})^3$ and $(5\text{nm})^3$ for the 5 μm and 700 nm rings, respectively. Recall that there are two types of domain walls between head to head domains. One is a flux closure structure, while the other is a transverse structure [101]. Micromagnetic simulations suggest that the observed MFM contrast for the onion state for the 5μm rings is due to a flux closure domain wall structure at the location where two half rings meet, as shown in figure 6.4(a) and 6.4(b). The z component of the stray field was calculated from the simulated results, as shown in Fig. 6.4(c). The stray field contrast is consistent with the experimental observation of two dark or two bright spots on each side of the ring. Simulation also shows that the transverse domain wall is expected to be formed in thinner or smaller sized rings as shown in Fig. 6.4(d), with the corresponding z component of the stray field in

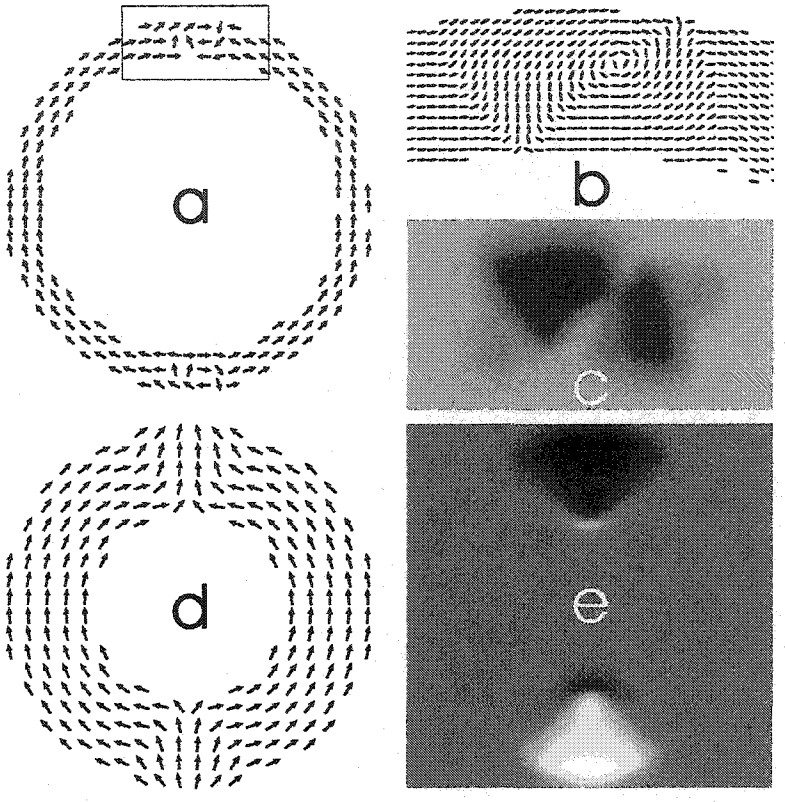

Figure 6.4: (a) Simulated remanent magnetic state after saturation of 5μm ring; (b) zoom of (a); (c) calculated H_z at 100 nm above ring of (b); (d) remanent magnetic state after saturation for 700 nm ring. (e) calculated H_z 50 nm above ring of (d).

Fig. 6.4(e). The metastable nature of the head-to head domain has not been revealed experimentally in 700 nm diameter rings as the stray field from the MFM tip for small tip-sample separations can clearly be larger than the pinning force of the domain wall.

The reason that the tip stray field does not induce a global magnetic transition in 5μm rings is that the tip stray field is localized on a lateral length scale of only several hundred nanometers. The tip stray field cannot flip the ring structure from the onion state to the flux state. This is very different for small (100 nm sized) particles or rings, where the tip globally influences the sample magnetization. In passing, we wish to point out that this is particularly the case when the MFM is operated in tapping/lift mode, where dramatic distortion can occur due to the fact that the tip physically touches the surface during part of the scan [33,100].

6.5 Switching Field Distribution

By comparing the switching behavior of many individual 5 μm rings, we found that the switching field Hs from the flux to the onion state is very uniform. The standard deviation of each individual ring is less than 1 Oe, a limit given by the minimal field increment used in these experiments. The ring to ring variation of the average switching field $< Hs >$ is in the range of 10 Oe. The average switching field $< Hs_{ensemble} >$ of many rings measured through 11 reversals is 135 Oe, with a standard deviation $\delta Hs_{ensmble}$ of less than 4 Oe. The switching field deviation of the ensemble of rings is thus only about 3% of the average switching field. This narrow distribution both for an individual ring as well as the ensemble is in stark contrast to the non-uniformity of the switching fields Hn from the onion to the flux state: it is not uniform. The average flux nucleation field $< Hn >$ is found to vary by as much as 50 Oe from ring to ring, the ensemble average $< Hn_{ensemble} >$ being about 60 Oe. The standard deviation of the ensemble average is $\delta Hn_{ensemble} \geq 10$ Oe, about 20 % of the average switching field. This large spread is due to the observed large spread in both the average as well as the standard distribution of $< Hn >$ of individual rings (see Table 6.1).

This uniformity in switching field Hs and its narrow distribution even holds true when the rings are only 700 nm in diameter (see Fig. 6.5). For these rings we find an ensemble average switching field of 201 Oe with a distribution of 11 Oe, a variability of 5%. Since the MFM tip stray field itself can induced the magnetization switching from the onion state to the vortex, we can not observe a well defined transition for such small ring.

We found experimentally that the reversal mechanism from the onion state to the flux state occurs through domain wall propagation, as indicated by the simulations by Rothman et al. [99]. The typical time for magnetization reversal is expected to be a few nanoseconds, substantially beyond the time-resolution capability of MFM. However, the propagating domain wall could be localized at various pinning sites

Particle	No.1	No.2	No.3	No.4	No.5	No.6	No.7	No.8
$<H_n>$	70	62	63	60	62	46	74	54
δH_n	27	22	14	18	6	4	4	18
$<H_s>$	139	139	131	142	138	138	142	139
δH_s	1.6	2.4	1.6	1.5	1.6	1.5	0.4	0.8

Table 6.1: The average switching field and switching field distribution of individual 5μm rings; in Oersted.

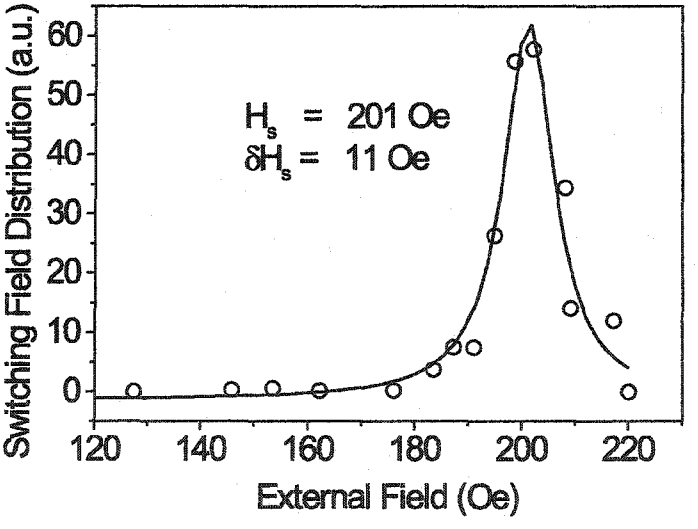

Figure 6.5: Percentage of particles switching from the onion to the flux state as a function of external magnetic field for ring of 700nm diameter. The solid line is a Lorentz fit.

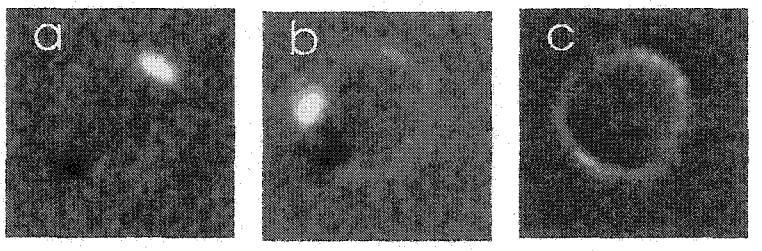

Figure 6.6: The switching mechanism from the onion to the flux state is domain wall propagation. (a) remanent state; (b) H = 25 Oe; (c) H=60 Oe.

(probably associated with sample defects), as shown in Fig. 6.6. Fig. 6.6 (a) shows the onion state at remanence; the wall started to move at a field of about 25 Oe, and was subsequently pinned at another location as shown in Fig. 6.6(b). The domain wall was depinned again at a larger field of 60 Oe, and completed the reversal process to a vortex state shown in Fig. 6.6(c). The direct observation of the reversal mechanism is possible only in a very small percentage of the total number of studied rings. We found that the propagation of the domain wall to be either clockwise or anticlockwise for different individual rings. We conclude that the reversal mechanism from the onion to the flux state is completed through a domain wall propagation process, and dominated by local pinning fields. As a consequence, the switching field depends on the local domain wall pinning potential. Individual rings differ from each other due to uncontrolled variations in their defect density, edge smoothness and chemical composition. This leads to head to head domain walls with different pinning forces and the consequent observed broad distribution of switching fields Hn.

Our observation of the transition field from the flux to the onion state shows only a small variation. Based on the difference in the standard deviation between the two switching fields, we propose that the reversal mechanism for the transition from the flux to the onion state is different from that of the transition from the onion to the flux state. Inhomogeneity of the rings only slightly modify the switching field from the flux to the onion state. This points to a reversal process that is not dominated by domain wall motion, which is strongly affected by existing sample inhomogeneities

leading to a large variation in pinning energies. The latter effect should increase relatively as the ring size becomes smaller, but is not observed (see Fig. 6.5 for 700 nm rings). The most probable reversal mechanism is thus a nucleation process. Once nucleated, the walls move rapidly through the sample as the field Hs is substantially larger than the domain wall pinning field. The global reversal, however, cannot take place until the external field is big enough to overcome the shape determined reversal field Hs. Below Hs, the external field only reversibly distorts the flux configuration.

6.6 Conclusion

Two different reversal mechanisms from the onion state to the flux state, or from the flux state to the reversed onion state, were found through MFM measurements. The detected nature of head to head domain wall structure in the onion state of 5 μm rings was found to be a flux closure structure both by MFM imaging and by micromagnetic simulation. The switching field is not uniform for transitions from the onion state to the flux state, which is shown to be due to domain wall propagation strongly influenced by variations of the local pinning potential. This is in contrast to the switching field for the transition from the flux to the onion state, which is quite uniform. Defects, roughness and size variation play a minor role in this switching process. This switching mode is very reproducible with a very narrow field distribution even for ensembles of rings. As a consequence, the flux state can be stabilized even for large ensembles in a very controllable manner within a wide field range.

7

Conclusion & Outlook

Magnetic force microscopy has been shown to be a versatile tool with which to study lithographically patterned submicron magnets. The technique offers the ability to probe magnetic structure, and the ability to characterize the magnetization reversal mechanisms.

Most results presented in this thesis were obtained by a custom built vacuum magnetic force microscopy under moderate vacuum of 1×10^{-5} Torr with *in situ* in-plane potentially rotatable magnetic fields. The system has been optimized to achieve very high sensitivity limited by thermal noise of the cantilever.

MFM tip stray field can irreversibly distort the sample magnetization state. Great care has been taken to study magnetically soft particles. A systematic study of MFM tip stray field distortion to sample's magnetization state was presented by using various MFM tip, in different operating modes, and using different samples (particles). The technique of how to detect and minimize the irreversible distortion was also proposed. This distortion can be largely reduced by performing MFM in the constant height mode, using low magnetic moment tips, and by operating in vacuum. MFM tip stray field itself can be used to control a particle's magnetic moment state by controlled three dimensional positioning the tip above a particle.

MFM in the presence of magnetic fields can be used to characterize the magnetization switching field and magnetization switching behavior. A new method is developed to characterize magnetization switching of an individual element by monitoring the cantilever frequency shift with respect to magnetic fields without scanning.

Based on above techniques, various lithographically patterned submicron magnetic particle arrays were studied (Section 3.6, Chapters 4, 5, 6). These techniques allow us to perform high sensitivity and less destructive imaging, and allow us to study the details of magnetic structures. For example, the nature of the head-to-head domain wall in a permalloy ring is revealed to be flux closure structures, and the vortex structure with a core singularity in a permalloy disk can be found by high resolution imaging. In the pseudo spin valve structures, the parallel and two different antiparallel configurations for both magnetic layers (NiFe and Co) in an element can be distinguishable. The study of the elongated permalloy disks indicates that vortices can be trapped in elliptical elements even for medium (4:1) aspect ratio elements.

Local hysteresis loop techniques allows us to study the switching behavior of individual elements. In a permalloy disk, the abrupt switching due to a nucleation or annihilation of a vortex has been revealed. In a pseudo spin valve structure, the abrupt switching for both individual layers is clearly distinguishable.

The remanent 'hysteresis loop' can be obtained in the presence of a magnetic field. The interdot coupling induced anisotropy was found in a closely packed disk array which shows a much smaller nucleation and annihilation field along the (100) direction than the (110) direction. This coupling was directly revealed through MFM image, as the switched magnetic elements form chain structures. In the PSV structures, the layer coupling and the broad switching field distribution were investigated through major and minor hysteresis loops obtained by MFM.

Regarding to future experiments, these techniques will be applied to other submicron and nanoscale magnetic elements to characterize their magnetic structures and switching behaviors. For example, MFM can be used to obtain a phase diagram of a vortex state and a single domain state as a function of element thickness and diameter. MFM has the ability to probe ferromagnetic and antiferromagnetic coupling between nanomagnets. As MFM only detects the stray field (or stray field gradient) of the sample, complimentary studies through other techniques will be very useful.

These techniques include micromagnetic simulation, spatial resolved imaging technique (LEM or SEMPA), time-resolved imaging technique (time-resolved scanning Kerr microscopy), and the techniques characterizing the collective behaviors (AGM, SQUID magnetometery). A combination of these techniques allows one to fully reveal the mechanism of magnetization switching.

Besides studying the magnetization structure and magnetization switching, the application of using MFM tip stray field to 'write' and 'read' information is promising. For example, we will use MFM tip stray field to control the output of a magnetic logic gate [4].

Appendix A

Magnetic moment or spin configuration can be approached by solving the formalism of micromagnetics [32], in which a macroscopic view is adopted where the atomic spin configuration is averaged to form a continuous magnetization M(r). The magnitude of M(r) is constrained to be a constant with $|\mathbf{m}(r)|^2 = |\mathbf{M}(r)/\mathbf{M}|^2 = 1$. Magnetic moment configuration in a system is then chosen to make the total energy minimal.

A.1 Energy terms

The total system energy is written as a sum of anisotropy energy, exchange energy, Zeeman energy, magnetostatic energy, magneto-elastic interaction energy and magnetostriction energy. The last two energies are often neglected due to their small contributions.

A.1.1 Exchange energy

Magnetic ordering is a result of the electron-electron Coulomb interaction, together with the Pauli exclusion. A simple model dealing with magnetic ordering is Heisenberg spin-spin exchange interaction, which is a quantum-mechanical interaction. In micromagnetics, a classical energy term is used to replace the quantum-mechanical exchange interaction. In the case of a continuous magnetization distribution, the exchange energy density can be written as

$$E_{ex} = A_{ex}M^2[(\bigtriangledown m_x)^2 + (\bigtriangledown m_y)^2 + (\bigtriangledown m_z)^2], \tag{A.1}$$

where A_{ex} is the exchange constant related to the interatomic exchange.

A.1.2 Zeeman energy

Zeeman energy appears when a magnetic field is applied, such magnetic field may be either uniform or spatially varying e.g. the stray field from an MFM tip. The Zeeman energy density can be expressed as

$$E_H = -M\mathbf{H}_{ext}(r) \cdot \mathbf{m}(r) \tag{A.2}$$

where $\mathbf{H}_{ext}(r)$ is the external magnetic field applied at point r.

A.1.3 Magnetostatic Energy

The stray field energy (magnetostatic energy) can be considered as the magnetic field energy with magnetic field generated by the magnetic body itself, and the energy term can be expressed as

$$E_d = \frac{M}{2} \int \mathbf{m}(r) \cdot \mathbf{H}_{mag}(r', r) d^3r' \tag{A.3}$$

where $H_{mag}(r')$ is the field generated by the magnetic body of point r' at point r, and can be expressed as

$$\mathbf{H}_{mag}(r', r) = M \int d^3r' \frac{3\hat{\mathbf{r}}(\hat{\mathbf{r}} \cdot \mathbf{m}(\mathbf{r}')) - \mathbf{m}(\mathbf{r}')}{|\mathbf{r} - \mathbf{r}'|^3} \tag{A.4}$$

A.1.4 Crystalline Anisotropy Energy

The energy of a ferromagnet depends on the direction of the magnetization relative to the structural axes of the material, resulting from spin-orbit interactions. The cyrstalline anisotropy energy density can be expressed as,

$$E_{anis} = K(r)|\mathbf{k}(r) \times \mathbf{m}(r)|^2, \tag{A.5}$$

where K(r) is the magnitude of the anisotropy of each grain and $\mathbf{k}(r)$ denotes the orientation of the anisotropy easy axis. For uniaxial crystalline material, the anisotropy energy can be written as

$$E_{anis} = K sin^2\theta. \tag{A.6}$$

However, for polycrystalline material, the anisotropy easy axis can be randomly, and for soft magnetic material such as permalloy, the energy is very small.

A.2 Micromagnetic modelling

The total energy density at $\mathbf{m}(r)$ is just a summing up all the contributions of previous sections, which can be expressed as

$$E_{tot} = E_{ex} + E_{anis} + E_H + E_d. \tag{A.7}$$

The total (free) energy is then

$$F = \int d^3r(E_{ex} + E_{anis} + E_H + E_d). \tag{A.8}$$

Given the system energy, there are two common approaches for determining the magnetic moment configuration. One way utilizes a variational principle to obtain the equilibrium magnetization pattern by finding the configuration that minimize the energy by finite-element techniques [102].

However, an alternative approach is to solve the Landau-Lifshitz dynamic equation of motion with suitable damping. Magnetic field produces a torque on the magnetization, and the magnetic moment follows a damped precession about the field until it loses the excess energy through dissipation. The Landau-Lifschitz-Gilbert (LLG) equation can be expressed as

$$\frac{dM}{dt} = -\gamma M \times H_{eff} - \frac{\gamma\alpha}{M_s} M \times (M \times H_{eff}), \tag{A.9}$$

where M is the magnetization, H_{eff} is the effective field, γ is the gyromagnetic ratio, while α is the damping coefficient. The effective field is defined as

$$H_{eff} = -\frac{\partial E_{tot}}{\partial M}, \tag{A.10}$$

where E_{tot} is the total magnetic energy density defined in eq. A.7.

A.3 OOMMF

All micromagnetic simulations throughout the thesis were perfomred using the OOMMF (Object Oriented Micromagnetic Framework) code from the National Institute of Standards and Technology.[1] It is portable, extensible public domain micromagnetic simulation program. The simulations were performed in two or three dimensions. For two dimensional simulation, the micromagnetic problem is impressed upon a regular 2D grid of squares, with three dimensional magnetization $\mathbf{m}(\mathrm{r})$ positioned at the center of the cells. The anisotropy and applied field energy terms are calculated assuming constant magnetization in each cell. The exchange energy is calculated using the eight-neighbor bilinear interpolation described in reference [103]. The magnetostatic energy is calculated through various algorithms, such as 'ConstMag', '3dSlab' and '3dCharge'. The algorithm of 'ConstMag' calculates the *average* field in each cell under the assumption that the magnetization is constant in each cell, using formulae from reference [104]. The algorithm of '3dSlab' calculates the in-plane field components using offset blocks of constant (volume) charge. Details can be found in reference [105]. all algorithms use Fast Fourier Transform techniques. The Landau-Lifshitz equation is integrated using a second order predictor-corrector technique of the Adams type.

In submicron magnetic systems, the relevant length scale is usually characterized by the exchange length,

$$l_{ex} = (\frac{A_{ex}}{4\pi {M_s}^2})^{1/2}, \tag{A.11}$$

where A_{ex} is the exchange constant, with the order of 1.0×10^{-6} erg/cm. The value of l_{ex} is about 10 nm. For micromagnetic simulation, it is usually safe to choose an unit cell size with smaller value than the exchange length.

Fig. A.1 shows an example of the magnetic moment pattern in 'McGill'. The size of 'McGill' is 2.2μm $\times$ 0.8μm with the thickness of 8 nm, as shown in Fig. A.1(a). The material is Permalloy with the saturation magnetization of 860 emu/cm^3 and

[1] http://math.nist.gov/oommf.

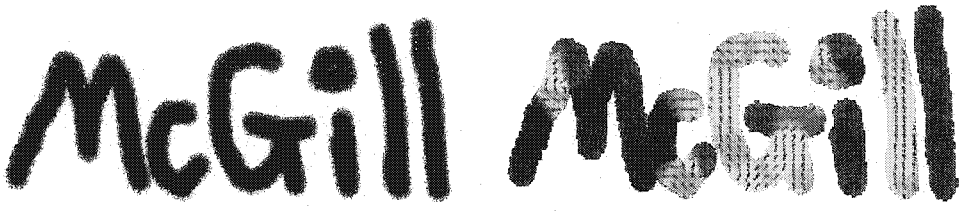

Figure A.1: (a)pattern of 'McGill' with size 2.2 μm $\times$ 0.8 μm; (b) micromagnetic simulation patters. Arrows and colors indicate the magnetic moment orientation.

the exchange constant A of 1.0×10^{-6} erg/cm. The unit cell size is $8 \times 8 \times \times 8\text{nm}^3$. The initial configuration is chosen randomly. The magnetic moment configuration obtained through micromagnetic simulation is shown in Fig. A.1(b). As can be seen, two 'l's form single domain states, and 'i' forms a vortex and single domain state. There are a few head-to-head domains in 'McG'.

Bibliography

[1] R. L. White, R. M. H. New, and R. F. W. Pease, IEEE Trans. Magn. **33** 990 (1997).

[2] S. S. P. Parkin, K. P. Roche, M. G. Samant, P. M. Rice, R. B. Beyers, R. E. Scheuerlein, E. J. O'Sullivan, S. L. Brown, J. Bucchigano, D. W. Abraham, Y. Lu, M. Rooks, P. L. Trouilloud, R. A. Wanner, and W. J. Gallagher, J. Appl. Phys. **85**, 5828 (1999).

[3] J. M. Daughton, A. V. Pohm, R. T. Fayfield, and C. H. Smith, J. Phs. D **32**, R169 (1999).

[4] R. P. Cowburn and M. E. Welland, Science, **287**, 1466 (2000).

[5] S. Mann, R. B. Frankel, R. P. Blakemore, Nature **310**, 405 (1984); S. Mann, N. H. C. Sparks, R. B. Frankel, D. A. Bazylinski, H. W. Jannasch, Nature **343**, 258 (1990).

[6] R. B. Proksch, T. E. Schäffer, B. M. Moskowitz, E. D. Dahlberg, D. A. Bazylinski and R. B. Frankel, Appl Phys. Lett. **66**, 2582 (1995).

[7] J. F. Smyth, S. Schultz, D. R. Fredkin, D. P. Kern, S. A. Rishton, H. Schmid, M. Cali, and T. R. Koehler, J. Appl. Phys. **69**, 5262 (1991).

[8] S. Y. Chou, M. Wei, P. R. Krauss, and P. B. Fischer, J. Appl. Phys. **70**, 6673 (1994).

[9] J. E. Wegrowe, O. Fruchart, J.-P. Nozieres, D. Givord, F. Rousseaux, D. Decanini, and J. Ph. Ansermet, J. Appl. Phys. **86**, 1028 (1999).

[10] B. Cui, W. Wu, L. Kong, X. Sun, and S. Y. Chou, J. Appl. Phys. **85**, 5534 (1999).

[11] C. A. Ross, S. Haratani, F. J. Castano, Y. Hao, M. Hwang, M. Shima, J. Y. Cheng, B. Vogeli, M. Farhoud, M. Walsh, and Henry I. Smith, J. Appl. Phys. **91**, 6848 (2002).

[12] A. Fernandez, M. R. Gibbons, M. A. Wall, and C. J. Cerjan, J. Magn. Magn. Mater. **190**, 71 (1998).

[13] J. Liang, H. Chik, A. Yin, and J. Xu, J. Appl. Phys. **91**, 2544 (2002)

[14] R. P. Cowburn, J. Phys. D: Appl. Phys. **33** 1 (2000).

[15] B. D. Cullity, *Introduction to magnetic materials*, Addison-Wesley Publishing Company, Inc. (1972).

[16] Alex Hubert and Rudolf Schäfer, *Magnetic Domains: The Analysis of Magnetic Microstructures*, Springer-Verlag Berlin Heidelberg 1998.

[17] A. Aharoni, *Introduction to the Theory of Ferromagnetism* (Oxford University Press, Oxford, 1996), Sec. 10.5.1.

[18] Y. Martin and H. K. Wickramasinghe, Appl. Phys. Lett. **50**, 1455 (1987)

[19] J. J. Saenz, N. Garcia, P. Grütter, E. Meyer, H. Heinzelmann, R. Wiesendanger, L. Rosenthaler, H. R. Hidber, H. J. Güntherodt, J. Appl. Phys. 62, 4293 (1987).

[20] P. Grütter, H. J. Mamin and D. Rugar, *Magnetic Force Microscopy*, Springer Ser. Surface Sciences, Vol. 28 (Springer, Berlin, Heidelberg 1992)

[21] J. N. Chapman, J. Phys. D: Appl. Phys. **17**, 623 (1984).

[22] J. Unguris, D. T. Pierce, A. Galejs, and R. J. Celotta, Phys. Rev. Lett. **49**, 72 (1982).

[23] W. Wernsdorfer, D. Mailly, and A. Benoit, J. Appl. Phys. **87**, 5094 (1996).

[24] O. Fruchart, J.-P. Nozières, W. Wernsdorfer, D. Givord, F. Rousseaux, and D. Decanini, Phys. Rev. Lett. **82**, 1305 (1999).

[25] D. Schuh, J. Biberger, A. Bauer, W. Breuer, and D. Weiss, IEEE Tran. Mag. **37**, 2091 (2001).

[26] X. Zhu, P. Grütter, V. Metlushko, B. Ilic, Appl. Phys. Lett. **80**, 4789 (2002).

[27] B. C. Choi, M. Belov, W. K. Hiebert, G. E. Ballentine, and M. R. Freeman, Phys. Rev. Lett. **86**, 728 (2001).

[28] P. Grütter, Th. Jung, H. Heinzelmann, A. Wadas, E. Meyers, H. R. Hidber, H.-J. Güntherodt, J. Appl. Phys. **67**, 1437 (1990).

[29] A. Y. Elezzabi, M. R. Freeman, and M. Hohnson, Phys. Rev. Lett. **77**, 3220 (1996).

[30] R. D. Gomez, M. C. Shih, R. M. H. New, R. F. W. Pease and R. L. White, J. Appl. Phys. **80**, 342 (1996); R. D. Gomez, E. R. Burke, Isaak and D. Mayergoyz, *ibib.* **79**, 6446 (1996).

[31] R. Proksch, E. Runge, P. K. Hansma and S. Foss, J. Appl. Phys. **78**, 3303 (1995).

[32] W. F. Brown, *Micromagnetics*, Interscience, New York, 1963.

[33] Xiaobin Zhu, P. Grütter, V. Metlushko, B. Ilic, J. Appl. Phys., **91**, 7340 (2002).

[34] T. R. Albrecht, P. Grütter, D. Horne and D. Rugar, J. Appl. Phys. **69**, 668 (1991)

[35] F. J. Giessibl, Phys. Rev. B **56**, 16010 (1997).

[36] P. Grütter, Y. Liu, P. LeBlanc, and U. Dürig, Appl. Phys. Lett. **71**, 279 (1997)

[37] Y. Liu, Ph.D. thesis, McGill University, 1997.

[38] J. Israelachvili, Intermolecular Surface Force, Academic Press, (1992).

[39] D. Rugar, H. J. Mamin, P. Guethner, S. E. Lambert, J. E. Stern, I. McFadyen, and T. Yogi, J. Appl. Phys. **68**, 1169 (1990).

[40] Digital Instruments, Santa Barbarla, California, USA, http://www.di.com. Patent.

[41] C. Schönenberger and S. F. Alvarado, Z. Phys. B **80**, 373 (1990).

[42] P. LeBlanc, MSc. thesis, McGill University, 1995.

[43] http://www.nanosensros.com

[44] http://www.mikromasch.com

[45] J. E. Sader, J. W. M. Chon, and P. Mulvaney, Rev. Sci. Inst. **70**, 3967 (1999).

[46] J. E. Sader, J. Appl. Phys. **84**, 64 (1998).

[47] Dror Sarid, *Scanning Force Microscopy with Applications to Electric, Magnetic and Atomic Forces*, Oxford University Press, 1994

[48] D. Rugar, H. J. Mamin and P. Güthner, Appl. Phys. Lett. **55**, 2588 (1989)

[49] M. Roseman, Ph.D. thesis, McGill University, Canada, 2001.

[50] U. Dürig, H. R. Steinauer, and N. Blanc, J. Appl. Phys. **82**, 3641 (1997)

[51] Digital PLL and Amplitude feedback from Nanosurf AG, Liestal, CH (www.nanosurf.com)

[52] D. P. E. Smith, Rev. Sci. Instrum. **66**, 3191 (1995).

[53] H. J. Mamin and D. Rugar, Appl. Phys. Lett. **79**, 3358 (2001).

[54] P. Grütter, D. Rugar, H. J. Mamin, G. Castillo, C.-J. Lin, I. R. McFadyen, O. Wolter, T. Bayer, J. Greschner, J. Appl. Phys. **69**, 5883 (1991).

[55] H. J. Mamin, D. Rugar, J. E. Stern, R. E. Fontana, Jr. P. Kasiraj: Appl. Phys. Lett. **55**, 318 (1989).

[56] T. Göddenhenrich, U. Hartmann, M. Anders and C. Heiden: J. Microscopy **152**, 527 (1988).

[57] Laurent Belliard, Ph.D. thesis, Universite de Paris-Sud Center D'Orsay (1997).

[58] M. Lederman, G. A. Gibson, S. Schultz, J. Appl. Phys., **73**, 6961 (1993).

[59] J. M. Garcia, A. Thiaville, J. Miltat, K. J. Kirk, J. N. Chapman and F. Alouges, Appl. Phys. Lett. **79**,656 (2001).

[60] M. Kleiber, F. Kummerlen, M. Lohndorf, A. Wadas, D. Weiss and R. Wiesendanger, Phys. Rev. B **58**, 5563 (1998)

[61] C. A. Ross, M. Farhoud, M.Hwang, Henry I. Smith, M. Redjdal and F.B. Humphrey, J. Appl. Phys. **89**, 1310 (2001).

[62] Jing Shi, S. Tehrani and M. R. Scheinfein, Appl. Phys. Lett. **76**, 2588 (2000).

[63] B. Anczykowski, J.P. Cleveland, D. Krüger, V. Elings, H. Fuchs, Appl. Phys. A **66**, S885-S889 (1998).

[64] A. Thiaville, L. Belliard, D. Majer, E. Zeldov and J. Miltat, J. Appl. Phys. **82**, 3182 (1997).

[65] S. McVitie, R. P. Ferrier, J. Scott, G. S. White and A. Gallagher, J. Appl. Phys. **89**, 3656 (2001).

[66] D. G. Streblechenko, M. R. Scheinfein, M. Mankos and K. Babcock, IEEE Tran. Magn. **32**, 4124 (1996).

[67] P. J. A. van Schendel, H. J. Hug, B. Stiefel, S. Martin and H.-J. Güntherodt, J. Appl. Phys. **88**, 435 (2000).

[68] George D. Skidmore and E. Dan Dahlberg, Appl. Phys. Lett. **71**, 3293 (1997).

[69] J. G. Zhu, Y. Zheng, G. A. Prinz, J. Appl. Phys. **87** 6668, (2000).

[70] J. F. Smyth, S. Schultz, D. Kern, H. Schmid and D. Yee, J. Appl. Phys. **63** 4237 (1988); J. F. Smyth, S. Schultz, D. R. Frekin, D. P. Kern, S. A. Rishton, H. Schmid, M. Cali and T. R. Koehler, *ibid.* **69**, 5262 (1991).

[71] G. A. Gibson and S. Schultz, J. Appl. Phys. **73**, 6961 (1993).

[72] M. Hehn, K. Ounadjela, J. -P. Bucher, F. Rousseaux, D. Decanini, B. Bertenlian and C. Chappet, Science, **272**, 1782 (1996).

[73] Jing Shi, S. Tehrani, T. Zhum Y. F. Zheng and J. -G. Zhu, Appl. Phys. Lett. **74**, 2525 (1999).

[74] R. E. Dunin-Borkowski, M. R. McCartney, B. Karynal, D. J. Smith and M. R. Scheinfein, Appl. Phys. Lett. **75**, 2641 (1999).

[75] R. P. Cowburn, A. O. Adeyeye, M.E. Welland, Phys. Rev. Lett. **81**, 5414 (1998).

[76] K. J. Kirk, J. N. Chapman, S. McVitie, P. R. Aitchison and C. D. W. Wilkinson, Appl. Phys. Lett. **75** 3683 (1999); K. J. Kirk, J. N. Chapman and C. D. Wilkinson, *ibid.* **71** 539 (1997).

[77] R. P. Cowburn, D. K. Koltsov, A. O. Adeyeye, M. E. Welland and D. M. Tricker, Phys. Rev. Lett. **83**, 1042 (1999).

[78] A. Fernandez and C. J. Cerjan, J. Appl. Phys., **87**, 1395 (2000); A. Fernandez, M. R. Gibbons, M. A. Wall and C. J. Cerjan, J. Magn. Magn. Mater. **190**, 71 (1998).

[79] E. Girgis, J. Schelten, J. Shi, J. Janesky, S. Tehrani, and H. Goronkin, Appl. Phys. Lett., **76**, 3780 (2000).

[80] Youfeng Zheng and J.-G. Zhu, J. Appl. Phys. **81**, 5471 (1997).

[81] N. A. Usov, C. Chang and Z. Wei, J. Appl. Phys. **89** 7591 (2001).

[82] L. Kong, Q. Pan, B. Cui, S. Y. Chou, J. Appl. Phys. **85**, 5492 (1999).

[83] R. P. Cowburn, D. K. Koltsov, A. O. Adeyeye, and M. E. Welland, J. Appl. Phys. **87**, 7067 (2000).

[84] B. A. Everitt, A. V. Pohm, A. Fink, J. M. Daughton, IEEE Trans. on Magnetism, **34**, 1060, (1998).

[85] J. M. Daughton, J. Magn. Magn. Mater. **192**, 334 (1999).

[86] F. J. Albert, J. A. Katine, R. A. Buhman, D. C. Ralph, Appl. Phys. Lett., **77**, 3809 (2000).

[87] M. R. McCartney, R. E. Dunin-Borkowski, M. R. Scheinfein, D. J. Smith, S. Gider, S. S. P. Parkin, Science, **286**, 1337 (1999).

[88] X. Poriter, A. K. Petford-Long, Appl. Phys. Lett., **76**, 754 (2000).

[89] J. A. Katine, F. J. Albert, R. A. Buhrman, E. B. Myers, D. C. Ralph, Phys. Rev. Lett., **84**, 3149 (2000).

[90] F. J. Castano, Y. Hao, M. Hwang, C. A. Ross, B. Vögeli, Henry I. Smith, S. Haratani, Appl. Phys. Lett., **79**, 1504 (2001).

[91] F. J. Castano, Y. Hao, C. A. Ross, B. Vögeli, Henry I. Smith, S. Haratani, J. Appl. Phys., **91**, 7317(2002).

[92] M. Schneider, H. Hoffman, and J. Zweck, Appl. Phys. Lett. **77**, 2909 (2000).

[93] T. Shinjo, T. Okuno, R. Hassdorf, K. Shigeto, T. Ono, Science, **289**, 930 (2000).

[94] V. Novosad, K. Yu. Guslienko, H. Shima, Y. Otani, S. G. Kim, K. Fukamichi, N. Kikuchi, O. Kitakami, Y. Shimada, Phys. Rev. B. **65**, 060402(R) (2002).

[95] M. Schneider, H. Hoffmann, J. Appl. Phys., **86**, 4539 (1999).

[96] C. Mathieu, C. Hartmann, M. Bauer, O. Buethner, S. Riedling, B. Ross, S. O. Demokritov, B. Bartenlian, C. Chappert, D. Decanini, F. Rousseaux, E. Cambril, A. Müller, B. Hoffmann, U. Hartmann, Appl. Phys. Lett., **70**, 2912 (1997).

[97] K. Yu. Guslienko, V. Novosad, Y. Otani, H. Shima, K. Fukamichi, Appl. Phys. Lett., **78**, 3848 (2001).

[98] K. Yu. Guslienko, Phys. Lett. A, **278**, 293 (2001).

[99] J. Rothman, M. Kläui, L. Lopez, C. A. F. Vaz, A. Bleloch, J. A. C. Bland, Z. Cui, R. Speaks, Phys. Rev. Lett. **86**, 1098 (2001); M. Kläui, J. Rothman, L. Lopez-Diaz, C. A. F. Vaz, J. A. C. Bland, and Z. Cui, Appl. Phys. Lett. **78**, 3268 (2001).

[100] S. P. Li, D. Peyrade, M. Natali, A. Lebib, Y. Chen, U. Ebels, L. D. Buda, and K. Ounadjela, Phys. Rev. Lett. **86**, 1102 (2001).

[101] R. D. McMichael, M. J. Donahue, IEEE Trans. Magn. 33, 4167 (1997).

[102] D. R. Fredkin and T. R. Kohler, J. Appl. Phys. **67**, 5544 (1990).

[103] M. J. Donahue and R. D. McMichael, Physica B **233**, 272 (1997).

[104] A. J. Newell, W. Williams, and D. J. Dunlop, J. Geophysical Research **98**, 9551 (1993).

[105] D. V. Berkov, K. Ramstöck, and A. Hubert, Phys. Stat. Sol. (a) **137**, 207 (1993).